THE UNIVERSITY *of* EDINBURGH

Detection and Analysis of Proteins in the Solid Phase Using Extrinsic and Intrinsic Fluorescence

---

Hannah Niland

Doctor of Philosophy

2016

Real knowledge is to know the extent of one's ignorance.

-Confucius

Knowledge rests not upon truth alone, but upon error also.

-Carl Jung

It is not when truth is dirty, but when it is shallow, that the lover of knowledge is reluctant to step into its waters.

-Friedrich Nietzsche

Censure is perhaps inevitable; for some are so ignorant that they grow sullen and silent and are chilled with horror at the sight of anything that bears the semblance of learning, in whatever shape it may appear; and should the *spectre* appear in the shape of *woman*, the pangs which they suffer are truly dismal.

-Elizabeth Fulhame

Abstract

Over the past two decades a body of evidence concerning residual biological contamination on cleaned surgical instruments has accumulated. This is substantiated by the number of yearly surgery cancellations due to visible residue on instruments in surgical packs and incidences of iatrogenic Creutzfeldt-Jakob disease (iCJD). It is therefore imperative to develop a method of protein detection for use in clinical sterile services departments (SSDs) for monitoring of decontamination quality. This Thesis describes the development and use of an epifluorescence surface scanner (EFScan) technology in the assessment of proteinaceous residue on surgical instruments, by detecting protein pre-labelled with fluorescein isothiocyanate (FITC), and exploratory studies on the feasibility of label-free detection, using intrinsic protein fluorescence.

Measurements using FITC labelling showed that residual protein on the order of micrograms can be found on new, single-use instruments (i.e. prior to use). This is comparable to the amount of residual protein found on retired, reusable instruments. To confirm the suitability of fluorescence techniques in the detection and quantification of proteinaceous residue, a blind, pilot study was carried out in conjunction with groups from Queen Mary University and the University of Southampton. Each University used a different labelling and detection method, and results showed good agreement between these methods. This showed that fluorescence is a suitable technique for the detection and quantification of proteinaceous contamination on surgical instruments.

The next step in the project focussed on detection of contamination via intrinsic protein fluorescence from tryptophan residues, with a view to elimination of the labelling step. Intrinsic fluorescence of proteins in solution is widely characterised; however, fluorescence characteristics of solid or surface-bound protein have been little studied. Therefore, the characterisation of solid protein fluorescence and the emission characteristics of protein adsorbed onto stainless steel was undertaken. Analysis of the commonly used protein standard bovine serum albumin (BSA) showed that the two tryptophan residues it contains are highly susceptible to photo-oxidation in the solid state, resulting in conversion to the fluorescent photoproducts n-formylkynurenine (NFK) and kynurenine. Therefore, BSA is not suitable for use as a standard in the development of intrinsic fluorescence detection of surface-bound protein. The 72-tryptophan protein fibrinogen, as well as a series of other multi-tryptophan proteins, were assessed and it was found that photo-oxidation of the

tryptophan residues did not occur on the irradiation timescale of 1 hour utilized. Therefore, it was concluded that lysozyme or gamma-globulins, a prominent group of serum proteins, would be more suitable candidates as a standard in subsequent research into the intrinsic detection and quantification of proteinaceous contamination.

A third study explored the potential use of fluorescence in the early diagnosis of cataract. This involved the fluorescence characterisation of healthy porcine lenses and the use of UV irradiation of the lens to attempt to create cataract *in vitro*. There was found to be a large variation in fluorescence characteristics from lens to lens, suggesting that fluorophore concentrations can vary significantly. This implies that identification of a suitable standard for the early detection of cataract may be problematic. Attempts to create cataract resulted in the photo-oxidation pathway which had been observed in BSA, and although NFK and kynurenine play a role in cataractogenesis, the accumulation of these photoproducts is not analogous to a natural cataract. It was found that these products could be destroyed by irradiation of the lens at appropriate photo-bleaching wavelengths. However, this also destroyed intrinsic, protective fluorophores within the lens, suggesting that a light-based method of cataract treatment may not be achievable.

Lay Summary

Thorough decontamination of reusable surgical instruments is both necessary and, in the Western world, presumed, yet millions of surgical operations are cancelled each year in the UK due to the presence of visible biological contamination on 'cleaned' surgical instruments. Residual biological contamination can lead to disease via iatrogenic transmission of infectious material; there has been particular concern about the risk of transmission of Variant Creutzfeldt-Jacob disease (vCJD), the human form of "mad cow disease" (BSE). Current methods for detecting residual contamination are insensitive and it is, therefore, imperative that a method of detection, quantification and monitoring is developed for use in clinical settings, as highlighted in the recently published Department of Health Guidance on the Management and Decontamination of Surgical Instruments in Acute Care. This Thesis describes the development of an epifluorescence surface scanner (EFScan) which has been used successfully to detect and quantify biological contamination on both reprocessed surgical instruments (cleaned multiple-use instruments which have been used in surgery) and single-use instruments (used for a single operation then disposed of), before they had been used in surgery. The EFScan method uses a non-toxic fluorescent dye which attaches to the protein residue on the surgical instrument to make it visible to the detection system; the fluorescence from the dye is picked up by a detector which scans over the surface of the instrument and the measured intensity (brightness) of the fluorescence indicates the amount of protein present. The sensitivity of the EFScan system is more than a thousand times greater than the standard test for protein contamination that is used currently to monitor the standard of decontamination of surgical instruments.

Analysis using this method has shown that protein contamination on the order micrograms can be found on unused single use instruments, comparable to levels found on poorly cleaned, reprocessed instruments. Moreover, a pilot study conducted between the University of Edinburgh, Queen Mary University of London and the University of Southampton, with each institution using a different fluorescence-based technique, showed good agreement between results, validating fluorescence as a valuable tool in the detection and quantification of biological contamination.

Subsequent research focussed on further development of the technique by attempting to detect protein without attaching a fluorescent dye, using the native fluorescence of proteins, which is due to a particular amino acid, tryptophan. It was found that, upon binding of proteins to the stainless steel surface of the instrument, fluorescence intensity decreased greatly, reducing the sensitivity of detection. Moreover, it was found that, the common protein standard, bovine serum albumin,

underwent light-induced decomposition, under the measurement conditions, destroying the tryptophan and its fluorescence. Analysis of other proteins found that the amount of tryptophan and its location within the protein structure affected the susceptibility to photo-decomposition and identified the protein lysozyme and a group of proteins known as gamma-globulins as far more suitable standards for future studies.

Another study reported in this Thesis investigated the fluorescence properties of healthy porcine lenses and the feasibility of using UV light to create cataracts *in vitro*, with a view to developing a fluorescence-based method for cataract diagnosis. Large variation in the fluorescence characteristics, from lens to lens, was observed, suggesting that a suitable reference for measurements may be difficult to obtain. It was found that irradiating the lens with UV light resulted in the same photo-decomposition reaction as had been observed in bovine serum albumin. This is only one aspect of natural cataract formation and does not fully replicate the complex process in the living eye. Nevertheless, the ability to detect the products of the photo-decomposition by their characteristic fluorescence may form the basis of a new diagnostic technique.The research conducted has reaffirmed fluorescence detection as a highly sensitive and selective analysis technique and has shown that it could be a powerful tool in clinical applications.

Declaration

This is to certify that that the work presented in this Thesis is my own unless otherwise indicated with a reference.

Signed:

Date:

Acknowledgements

Without the unwavering support and guidance from the following people, I wouldn't have made it this far.

Firstly, I would like to thank my supervisor, Anita Jones. Her seemingly endless knowledge and insight never cease to amaze and I am indebted to her for generously sharing it with me. Her generosity is not limited to sharing her wealth of knowledge but also her valuable time, of which she gives up much to support her students throughout their studies. Thank you, Anita.

Thank you too to my second supervisors David Dryden and Andy Alexander for your support throughout my PhD and to Jochen Arlt for putting up with endless COSMIC-based queries. Moreover, this PhD would not have been possible without the support of the EPSRC and our industrial partners at Edinburgh Biosciences Ltd.

My time as a post-graduate student at Edinburgh University has been enriched by the friendships I have made. Fi, Rachel, Grant, Gareth and Darren I can't thank you all enough for your support and insights over the last few years, being in a group with you has made the day-to-day (and the odd night!) an absolute pleasure.

Finally, to my friends, family and to my Jessie; who support and encourage me in all that I do, thank you for everything, I love you.

Table of Contents

Abbreviations

CJD	Creutzfeldt-Jakob disease
BSE	Bovine spongiform encephalopathy
SSD	Sterile service department
FITC	Fluorescein isothiocyanate
Trp	Tryptophan
UV	Ultraviolet
BSA	Bovine serum albumin
BFG	Bovine fibrinogen
HAI	Healthcare acquired infection
PrP^{c}	Normal prion protein
PrP^{Sc}	Pathological prion protein
COSMIC	Collaborative Optical Spectroscopy, Micromanipulation and Imaging Centre
TAC	Time to amplitude converter
MCP	Microchannel plate photomultiplier
IRF	Instrument response function
FWHM	Full width at half maximum
HTM 01-01	Health Technical Memorandum 01-01
EFScan	Epifluorescence Surface Scanner
FITC	Fluorescein isothiocyanate
SEM	Scanning electron microscopy
EDX	Energy-dispersive X-ray spectroscopy
FITC-BSA	BSA labelled with fluorescein isothiocyanate
CCD	Charge coupled device
OPA	o-Phthaldialdehyde
NAC	N-acetyl cysteine
FAD	Flavin adenine dinucleotide
RSD	Relative standard deviation
EEM	Excitation-emission matrix
3-OHK	3-Hydroxykynurenine
ToF-SIMS	Time-of-Flight Secondary Ion Mass Spectrometry
$^{1}O_{2}$	Singlet oxygen
PCh	Protective chromophore
LEC	Lens epithelial stem cells
AGEs	Advanced glycation end products
HPLC	High performance liquid chromatography
ELISA	Enzyme-linked immunosorbent assay
KRTD	Kynurenine-related tryptophan derivative

Chapter 1. Introduction and Background Theory

Creutzfeldt-Jakob disease (CJD) gained notoriety in the mid-90s due to the bovine spongiform encephalopathy (BSE) epizootic which resulted in numerous cases of variant CJD. Its infamy continues in the form of iatrogenic (medical procedure acquired) CJD of which yearly cases have remained constant since 1990[1]. The infectious agents in CJD are robust, mis-folded proteins known as prions and their resistance to current cleaning methods in clinical Sterile Services Departments (SSDs) and the lack of improvement in SSD standards are of great concern. As evidence has mounted that organic debris remains on surgical instruments following decontamination in SSDs[2-8] (which comprises of washing, followed by visual inspection, followed by steam sterilisation or autoclaving) quantitative methods for evaluating the degree of soiling have been sought. Initial investigations involved soaking instruments in strong detergents with sonication, followed by analysis of the washings[4-7]. However, as any residual protein on these instruments has survived washing with detergents and autoclaving, the soaking process is unlikely to remove all residual protein with consequential underestimation of the protein load. Accordingly, subsequent studies have focused on more sensitive methods of detection in the form of fluorescence to enable the *in situ* detection and quantification of proteinaceous contamination on surgical instruments.

This thesis describes a detection system based on the use of the extrinsic fluorophore fluorescein isothiocyanate (FITC) to label surface-bound protein in combination with epifluorescence detection, and demonstrates the efficacy of fluorescence in the analysis of single-use surgical instruments. Subsequent investigation into the possibility of utilising the intrinsic, tryptophan (Trp) fluorescence of proteins to the same end is then reported. The study focussed on the analysis of the fluorescence properties of Trp in model proteins in the solid state, both in crystalline form and adsorbed onto a stainless steel surface, and the effect of UV-induced photochemistry on that fluorescence. Four model proteins were studied to determine their viability as standards; bovine serum albumin (BSA), bovine fibrinogen (BFG), bovine γ–globulins and hen egg-white lysozyme, to gain insight into Trp photochemistry in proteins adsorbed onto surgical instruments. Finally, a project carried out in conjunction with Edinburgh Biosciences Ltd (the industrial partner in the PhD CASE studentship) is described. This study, which is also concerned with the effect of UV-irradiation on Trp fluorescence, explores the possibility of exploiting this effect in the early diagnosis of cataracts. The fluorescence of extracted, healthy porcine lenses

was characterised and the feasibility of creating and analysing cataract in those lenses has been explored. Further background information pertinent to each study is given in the introduction to each of the relevant chapters.

1.1 Motivation

Decontamination in hospitals and clinical settings is imperative to reduce the risk of healthcare-acquired infections (HAI). The theory of transmissible infection has been proposed sporadically for centuries, however, cleanliness in practice was not considered worthwhile until the work of Louis Pasteur, Florence Nightingale and, in particular, Joseph Lister in the 19th century. Decontamination and disinfection procedures have improved drastically since the importance of hand washing and the use of pure water in clinical settings was realised, however, there is still room for improvement.

1.1.1 Decontamination in Healthcare

Reducing the risk of HAI begins with a clean clinical environment and hygienic execution of procedures. Hand washing is the primary measure in reducing the risk of HAI[9] and, coupled with the use of protective clothing and cleaning and disinfection of the healthcare environment, hospital sanitation and safety has improved dramatically. Currently, one of the main concerns in the effort to reduce HAI is the lack of quality control concerning the decontamination of re-useable surgical instruments. Current guidelines provided by the Department of Health allow for local decisions on decontamination procedures and this, coupled with a lack of quality control, has led to deficiencies in decontamination standards. The standard process for the decontamination of surgical instruments involves disassembly, cleaning, disinfection, visual inspection, assembly, packaging and steam sterilization[10]; however, a body of evidence has accumulated regarding residual biological contamination on reprocessed surgical instruments.

Several studies have utilised swab tests using protein-specific reagents such as ninhydrin and ophthaldialdehyde/sodium 2-mercaptoethanesulfonate to detect and quantify proteinaceous contamination removed from reprocessed surgical instruments and have found that, in some cases, reprocessed instruments had hundreds of micrograms of proteinaceous contamination[6,7]. In many cases a large proportion of instruments had visible biological debris after decontamination and in

one instance 98% of instruments displayed visible contamination[7]. Subsequent research has demonstrated that swab tests are insensitive due to poor desorption of protein adhered onto the stainless steel surface[11]. Moreover, ninhydrin has poor affinity for protein and results from Lipscomb *et al*[12] suggest that up to 6.5 µg of proteinaceous contamination could remain undetected using these methods. More rigorous analysis of the washings from instruments incubated with extraction buffer or detergent to remove surface contamination found that, in some cases, milligrams of protein could be found on reprocessed surgical instruments[5]. Studies carried out by the Keevil group from Southampton University have shown that small changes to decontamination procedures could have a significant impact on their effectiveness. They have shown that both pre-soaking[13,14] and storing used instruments in a moist environment before washing[14] significantly reduced the amount of proteinaceous material remaining on instruments after washing. More sensitive methods, based on fluorescence detection, for the detection and quantification of proteinaceous contamination remaining on surgical instruments are currently under development and are discussed in more detail in Chapter 3.

Hand washing, hospital and bedding disinfection, protective clothing and surgical instrument decontamination combine to reduce the risk of HAI; however, in the early 90's the emergence of variant CJD (vCJD) presented a unique problem for the healthcare sector and has prompted a necessary revaluation of decontamination standards and procedures.

1.1.2 Creutzfeldt-Jakob Disease

CJD is a neurodegenerative disorder in which 90% of patients die within a year of symptom onset. CJD arises when an endogenous cell-surface glycoprotein known as PrP^{C} conformationally transforms into the infectious isoform PrP^{Sc}. The covalent modification of PrP^{C} can be genetic, acquired by exposure to prion-infected material - e.g. via food (variant), blood transfusion or surgery (iatrogenic) or may occur sporadically. Prion diseases are unique in that the infectious agent lacks genetic material in the form of DNA or RNA like bacteria and viruses, moreover, PrP^{Sc} displays some interesting physical properties. It is proposed that PrP^{Sc} is infectious as its monomers or oligomers act as a template that induces the transformation of PrP^{C} to the infectious conformational isoform[15] causing the degeneration of brain tissue in the form of spongiform change, neural loss, brain atrophy and the formation of

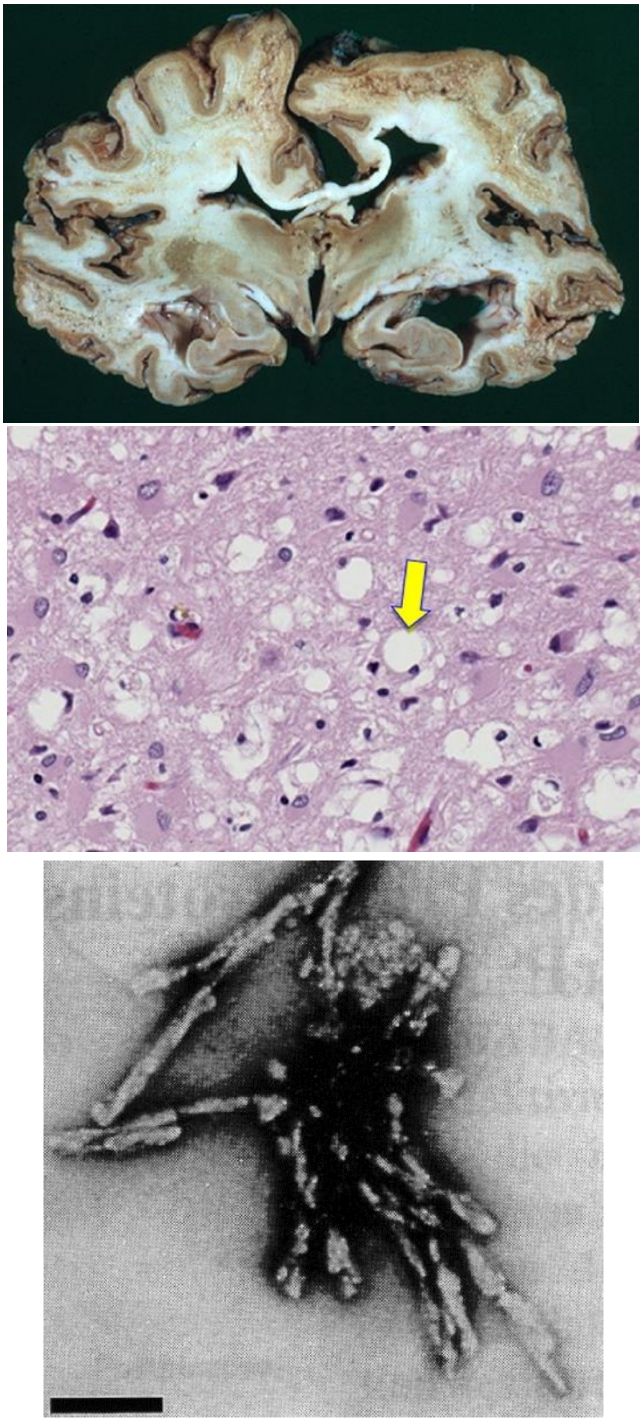

Figure 1.1a. Top – Severe atrophy in CJD infected brain, Middle - Spongiform change of neural tissue with vacuole indicated by yellow arrow[16], Bottom – Electron micrograph of purified prion rods[17]

amyloid plaques (Figure 1.1a). Although there is no difference in the primary structure of the isoforms, the secondary and tertiary structural differences result in entirely dissimilar biophysical properties. Unlike PrP^{C}, PrP^{Sc} has been shown to have partial resistance to proteolytic degradation, detergent solubility[18] and thermal

denaturation[19], the core steps in the decontamination process used in SSDs. Moreover, PrP^{Sc} has a very high affinity for surgical steel[10] and, therefore, binds strongly to the surface of surgical instruments. Even more troubling is a confirmed case of vCJD in 2016, which may indicate the return of vCJD in a second wave of cases[20]. This second wave is the result of our own genetics as there are two genetic variants of PrP^{C}, M and V. All patients diagnosed with vCJD so far have produced the M variant, however, in the 2016 case, the patient produced both the M and V variants. Due to the reduced concentration of the M variant the incubation period was longer and the onset of vCJD symptoms delayed. Furthermore, 51% of the population make both variants indicating that the yearly cases of vCJD may be set to rise. With the emergence of such a robust contagion, the development of instrumentation capable of accurately assessing the cleanliness of surgical instruments and the effectiveness of decontamination procedures is vital (see Chapter 3).

1.2 Principles of Fluorescence

This section highlights some of the principles of fluorescence and fluorescence spectroscopy. Content is mainly derived from Lakowicz[21] and Atkins and De Paula[22].

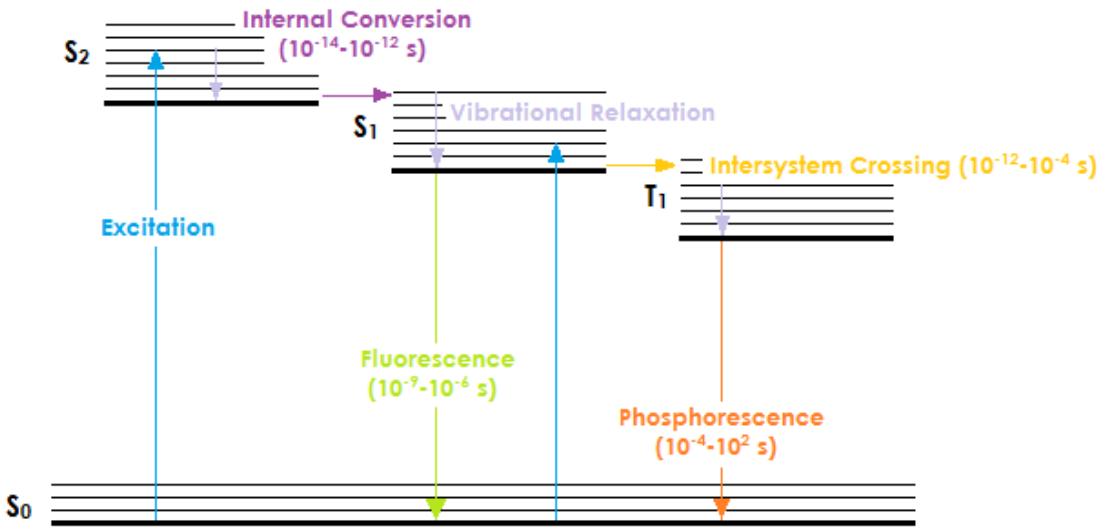

Figure 1.2a. Jablonski diagram showing possible transitions for a molecule

Fluorescence occurs when a fluorophore is excited from the ground singlet state (S_0) to a higher electronic singlet state (e.g. S_1 or S_2) by absorption of a photon. As the excited state relaxes, it may lose its excitation energy by the emission of a photon,

resulting in transient fluorescence. A summary of the excitation and possible relaxation pathways is shown in the Jablonski diagram in Figure 1.2a. Following absorption of a photon (excitation) the molecule can be excited to any one of the vibrational energy levels of the S_1 or S_2 (or higher) states and quickly relaxes to the lowest (thermally populated) vibrational energy level(s) of the S_1 state. This occurs via non-radiative decay processes; vibrational relaxation and internal conversion. The former is the loss of vibrational energy as heat to the surroundings and the latter is the non-radiative transition to a lower electronic state of the same multiplicity. The total excitation energy is conserved during internal conversion (horizontal transition), but the difference in electronic energy between the two states is converted into vibrational energy in the final state. A radiative transition from the lowest vibrational level of the S_1 state to the ground state (S_0) results in the release of a photon of fluorescence. As a result of rapid internal conversion and vibrational relaxation before the emission of a photon (in the condensed phase), the wavelength of fluorescence is independent of the excitation wavelength. This is known as Kasha's Rule. Figure 1.2b shows the typical forms of the excitation and emission spectra of the S_1 state of a fluorophore. The excitation (absorption) spectrum consists of transitions from the lowest vibrational level of S_0 to the many vibrational levels in S_1.

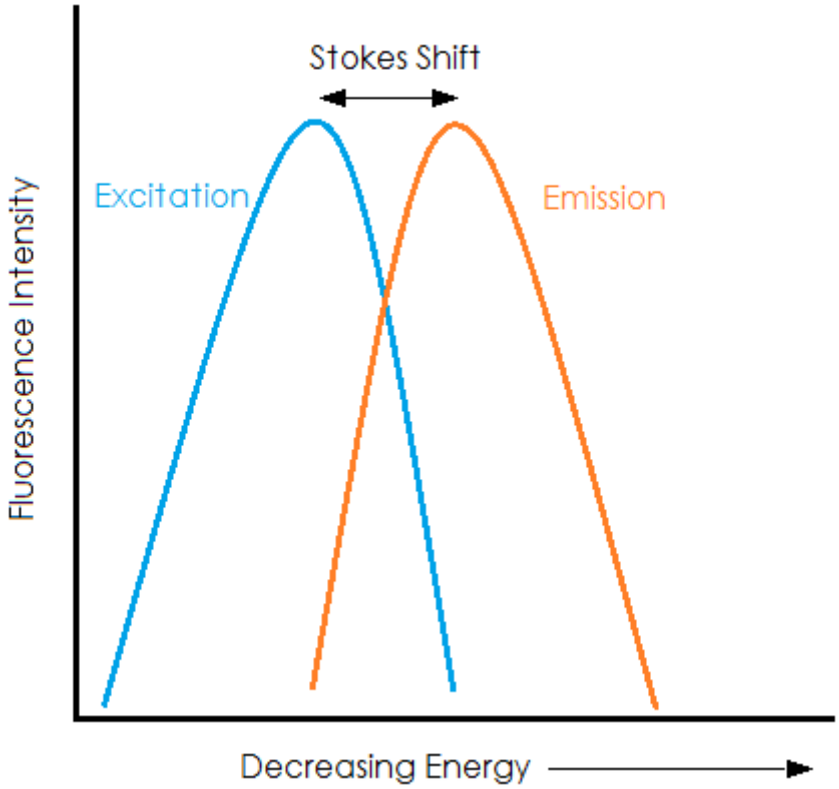

Figure 1.2b. Typical excitation and emission spectra

The intensity of each vibronic transition, and hence the spectral profile, is determined by the Franck-Condon principle. According to the Franck-Condon principle, the probability of a vibronic transition depends on the overlap of the ground and excited state vibrational wave functions; the more overlap the more likely the transition. Similarly, the emission spectrum consists of transitions from the lowest vibrational level of S_1 to many vibrational levels in S_0. The vibronic transitions that constitute the excitation spectrum thus lie to higher energy (shorter wavelength) than the pure electronic, 0-0, transition, whereas the vibronic transitions that constitute the emission spectrum lie to lower energy than the 0-0 transition. Therefore, the emission spectrum always lies at longer wavelength (lower energy) than the excitation spectrum, as shown in Figure 1.2b. The point at which the two spectral profiles overlap corresponds to the 0-0 transition and the separation between the maxima of the two spectra is known as the Stokes shift, the magnitude of which can vary largely between fluorophores. Radiative decay (fluorescence) of the S_1 state occurs in competition with non-radiative decay processes, internal conversion to the ground state and inter-system crossing to the triplet manifold, as shown in Figure 1.2a. Intersystem crossing is similar to internal conversion, except that it occurs between states of different multiplicity; it is a spin-forbidden process that occurs as a result of spin-orbit coupling. Intersystem crossing from S_1 results in population of the lowest triplet state, T_1, from which phosphorescence, radiative decay to the ground state may occur. Phosphorescence is a spin-forbidden process and, therefore, is much weaker than fluorescence, and occurs on a much longer timescale. The time taken for a molecule to emit fluorescence after excitation is expressed by its fluorescence lifetime. The definition of the fluorescence lifetime and its experimental measurement are discussed in Section 1.3.2. The fluorescence efficiency of a fluorophore, which depends on the relative rates of the radiative and non-radiative decay processes, is generally expressed by the fluorescence quantum yield (Φ), which is defined as the ratio of the number of photons emitted to the number of photons absorbed. Fluorophores with quantum yield values approaching 1 (i.e. the majority of absorbed light is converted to fluorescence) will give very bright emission. Numerous substances containing aromatic groups exhibit fluorescence with moderate-to-high quantum yields; for example, the aromatic amino acid residues give rise to the intrinsic fluorescence of proteins.

The Jablonski diagram shows only intramolecular, photo-physical, non-radiative decay processes. Intermolecular interactions may introduce additional non-radiative decay channels, generally referred to as quenching processes. Furthermore, excited

photochemical processes (excited state reactions), which may be intramolecular or intermolecular, can also lead to non-radiative decay of the S_1 state. If irreversible photochemical degradation of a fluorophore occurs, this results in irreversible loss of fluorescence, known as photo-bleaching.

1.3 Fluorescence Analysis Techniques

The fluorescence of many fluorophores is highly sensitive to the external environment which makes fluorescence a valuable technique, in the study of biological systems in particular. Various fluorescence analysis techniques are available, giving insight into particular aspects of a system, the most widely used of which are described below.

1.3.1 Steady-State Analysis

The excitation and emission spectra of a fluorophore are unique, characteristic properties. The excitation spectrum shows the emission intensity as a function of varying excitation wavelength, at a fixed emission wavelength. The emission spectrum shows the emission intensity as a function of varying emission wavelength, for a fixed excitation wavelength. Analysis of steady-state spectra can give insight into the excited state energies, the ground and excited state vibrational structure, the fluorescence quantum yield and the molecular environment of a molecule.

1.3.2 Fluorescence Lifetime and its Measurement

The fluorescence lifetime describes the amount of time a fluorophore remains in the excited state before emitting a photon. The overall rate of decay of an excited state population can be defined by considering the combination of radiative (fluorescence) and non-radiative (internal conversion, inter-system crossing, quenching, etc.) processes. A population of excited state fluorophores, [M*], decays with a rate according to;

$$-\frac{d[M^*]}{dt} = (k_R + k_{NR})[M^*] \qquad \textbf{Equation 1}$$

where k_R and k_{NR} are the rate constants of the radiative and non-radiative decay processes, respectively. Defining k_F as the sum of the rate constants for radiative and non-radiative decay processes ($k_F = k_R + k_{NR}$) and integrating Equation 1 gives an expression for the concentration of the excited state population as a function of time

$$[M^*](t) = [M^*]_0 e^{-(k_F t)} \qquad \textbf{Equation 2}$$

where $[M^*]_0$ is the concentration of M* at t= 0.

The property observed during fluorescence experiments is the fluorescence intensity, I, which is directly related to the excited state population:

$$I(t) = k_R[M^*] \qquad \textbf{Equation 3}$$

substituting for [M*] from Equation 3 gives

$$I(t) = I_0 e^{\frac{-t}{\tau_f}} \qquad \textbf{Equation 4}$$

where I_0 is the intensity at the time of the excitation pulse ($=k_R[M^*]_0$) and $\tau_f = 1/k_F$.

Equation 4, relates the observable property of the time-dependent decay of fluorescence intensity to the fluorescence lifetime τ_f, and allows its determination experimentally. The shorter the fluorescence lifetime, the more highly quenched is the fluorescence and the lower the quantum yield. If a sample contains a number of species, n, with different fluorescence lifetimes, the measured fluorescence decay consists of a sum of exponential terms, as given in Equation 5

$$I(t) = I_0 \sum_{i=1}^{n} A_i e^{\frac{-t}{\tau_i}} \qquad \textbf{Equation 5}$$

where A_i is the fractional amplitude and τ_i is the fluorescence lifetime of the emission of the *i*th species. In some cases, for example tryptophan within a protein, a single fluorophore can show a multi-exponential fluorescence decay as a result of its

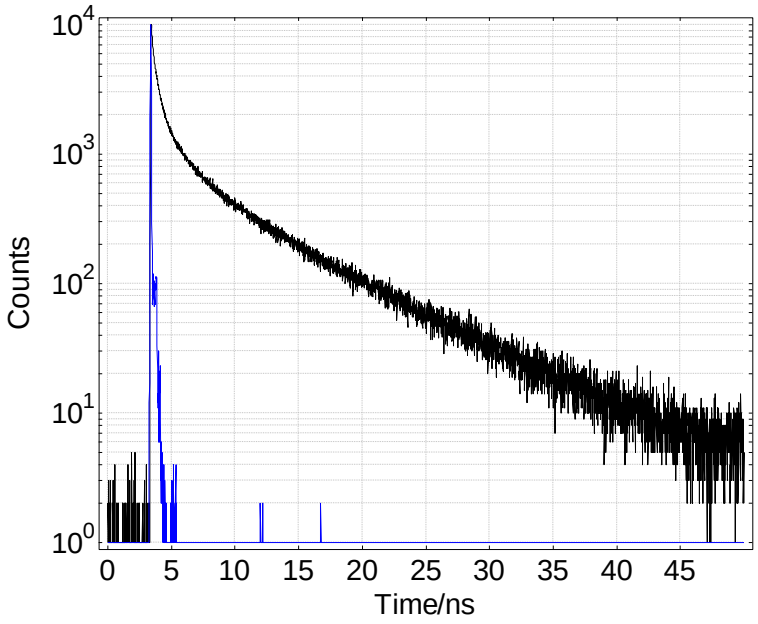

Figure 1.3a. Typical TCSPC data: decay curve (black) and instrument response function (IRF) (blue)

existence in a number of different local molecular environments, in which it experiences different quenching interactions. The fluorescence lifetime, τ_i, indicates the degree of quenching of the fluorophore in a particular environment and the fractional amplitude A_i, known as the A-factor, indicates the fraction of the fluorophore population that exists in that particular environment. In the present work, fluorescence lifetimes were measured using the technique of time-correlated single photon counting (TCSPC). In TCSPC, the time interval is measured between the excitation of the sample, with a short pulse of light, and the first detected photon of fluorescence. By repeating this cycle many times, a distribution of arrival times for individual photons at the detector is obtained. The distribution of photon counts versus arrival time corresponds to the fluorescence decay of the sample, as illustrated in Figure 1.3a. Fitting of the measured decay to an exponential function allows determination of the fluorescence lifetime(s) of the sample.

A generic experimental setup for TCSPC is shown in Figure 1.3b. A light source (laser) is used to produce narrow (femtosecond-nanosecond in width), rapid pulses of light. With each optical pulse an electronic 'start' pulse is simultaneously generated. This is done by splitting off part of the optical excitation pulse and directing it towards a photodiode. The photodiode converts the optical pulse to the electrical 'start' pulse. This passes through an electronic component called the 'constant fraction discriminator' (CFD) and from there is relayed to the time-to-amplitude converter (TAC). The TAC, which can be considered analogous to a stopwatch, is effectively a capacitor that begins to charge at the arrival of the start pulse. The remainder of the

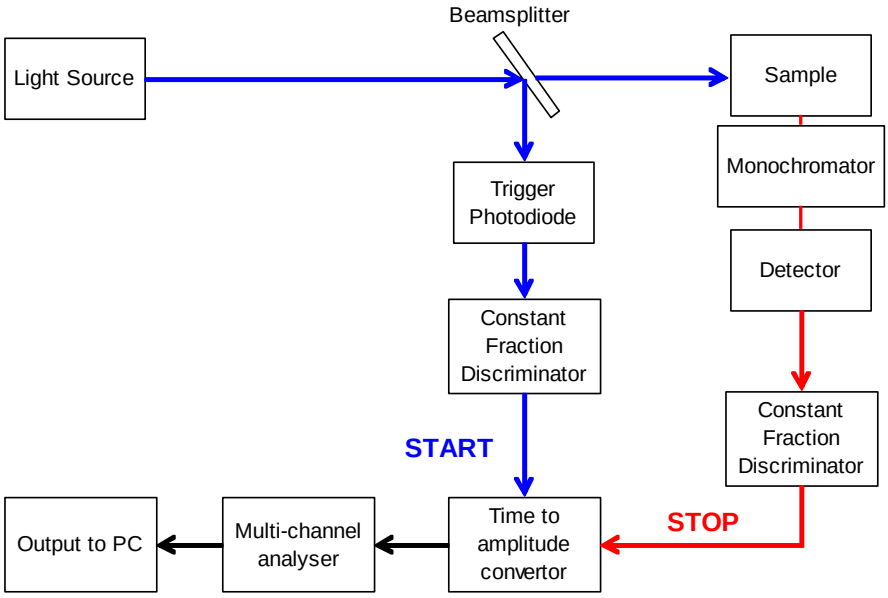

Figure 1.3b. Schematic of the components of a TCSPC system

optical pulse is directed toward the sample. Excitation of the fluorophore leads to the emission of photons, a few of which impact on the detector. The detector converts the energy from each photon into an electrical pulse. The first pulse released from the detector is used as the 'stop' pulse. It travels via the CFD to arrest the voltage ramp at the TAC. The TAC is then discharged and the resulting electrical pulse has a height that is directly related to the time between start and stop pulses. The multi-channel analyser converts the analogue pulse from the TAC into a digital signal which is registered as a single count on a histogram of fluorescence intensity (counts) against time. Collection of many thousands of these counts reveals an exponential decay curve that allows determination of the fluorescence lifetime(s) for the sample under investigation.

1.3.3 Fluorescence Imaging

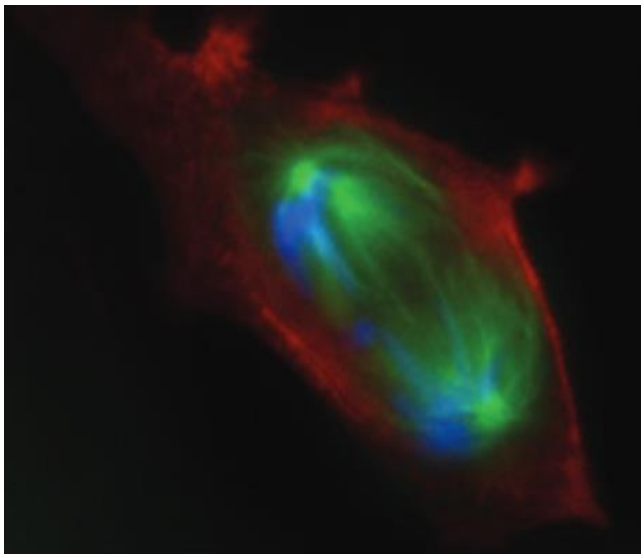

Figure 1.3c. Fluorescence micrographs of PtK2 kidney cell undergoing mitosis with chromosomes stained blue, tubulin stained green and actin stained red[23]

Fluorescence imaging utilises the fluorescence of certain probes and proteins to visualise and/or quantify a biological process or structure either statically or in real-time. Imaging systems are often based on epifluorescence detection in a microscope set-up with software controlled positioning of the sample for 3D analysis. Due to the lack of naturally occurring fluorophores in most biological systems, fluorescent probes specific to molecules of interest are used to elucidate the system. Figure 1.3c shows a cancer cell stained with probes specific to different structures; by varying the excitation wavelength, different probes are isolated and imaged. Combining the images obtained at different excitation wavelengths gives a complete view of the system of interest. The epifluorescence scanner used in the present work employs the same optical principles as an epifluorescence microscope, but uses low magnification to image the distribution of protein over the surface of a surgical instrument at low spatial resolution (on the mm scale).

1.4 Protein Structure and Fluorescence

Proteins are essential biomolecules that perform a vast array of cellular functions from catalysis to DNA replication and repair. Their primary structure is composed of amino acid residues and the length of the amino acid chain ranges from a few (peptides) to thousands of amino acids long (polypeptides/proteins). There are 20 ubiquitous amino acids which are coded in DNA, although approximately 500 amino acids are known. Each amino acid has different properties, such as charge and

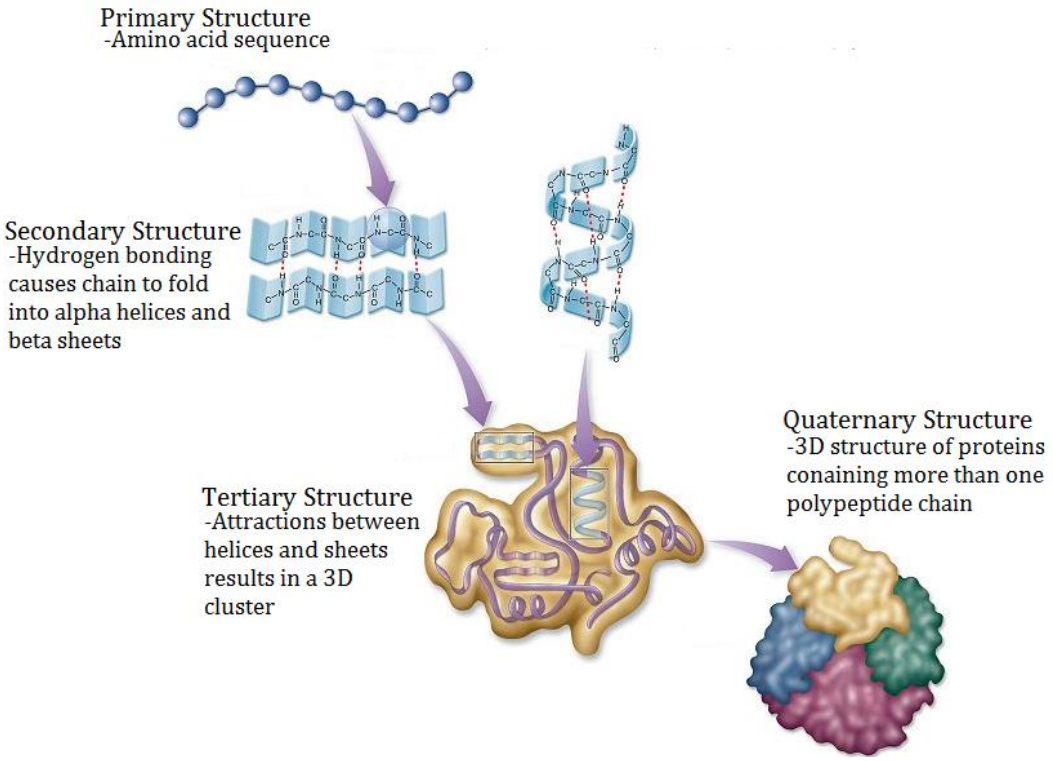

Figure 1.4a. Stages of protein folding

polarity, therefore it is the primary structure of a protein that determines how it arranges into its secondary, tertiary and quaternary structures (Figure 1.4a). The secondary structure of a protein describes ordered, local sub-structures which are formed via hydrogen bonding between amino acid residues; the two main types of secondary structure are α-helices and β-sheets. The tertiary structure of a protein forms when secondary structure components associate to form a 3D structure, which is driven by the requirement to bury hydrophobic residues. Once this 3D shape has been established, multi subunit proteins can form a quaternary structure which describes the association of protein subunits into complexes. The 3D structure of a protein determines its function and properties[24,25], a feature which is neatly demonstrated by PrP^{C} and PrP^{Sc}, where one is an endogenous glycoprotein and the

other causes fatal disease, as described in Section 1.1.2. Figure 1.4b shows the proposed change in secondary structure for these isoforms showing a transformation from an α-helix rich structure to a β-sheet rich structure.

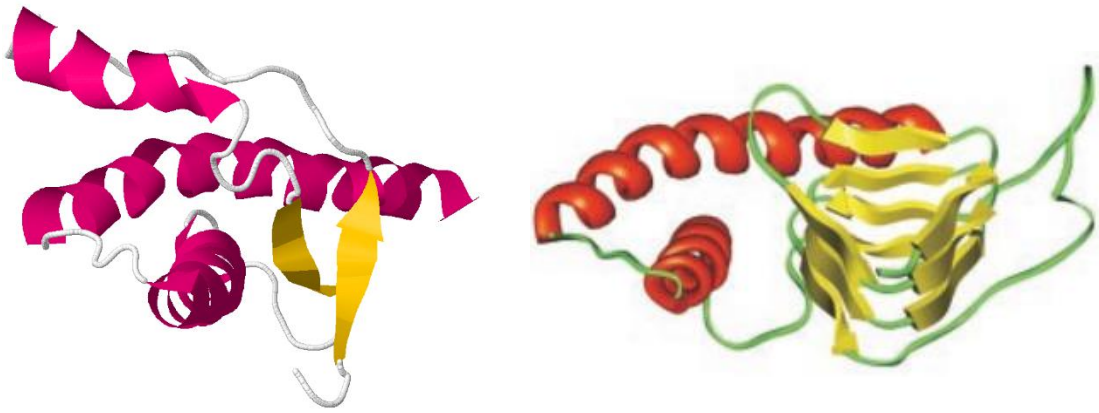

Figure 1.4b. Left – The globular domain of recombinant human prion protein PDB: 1QM0[26], Right: Proprosed structure of PrP^{Sc} combining the structure 1QM0 with the β-helical model of the N-terminal region of PrP 27–30[27]

1.4.1 Tryptophan, Tyrosine and Phenylalanine

There are 20 ubiquitous amino acids which are encoded directly from DNA to make proteins. (Following this, post-translational modifications alter the structure or chemical nature of the amino acids creating a vast array of modified amino acids with different functionalities.) Of these it is those containing aromatic side chains; tryptophan (Trp), tyrosine and phenylalanine, which fluoresce[21,28]. As Trp has the largest extinction coefficient and the highest quantum yield the majority of protein fluorescence can be attributed to it[21]. Tyrosine and phenylalanine do fluoresce, although their quantum yields are 8 and 140 times smaller, respectively; however, due to the absorption/emission spectral overlap of the three amino acids (Figure 1.4c), the energy absorbed by tyrosine and phenylalanine is often transferred to Trp, so that only Trp fluorescence is detected. Trp fluorescence is highly sensitive to its surrounding environment and is described as solvatochromic. This describes the shifting of emission wavelength depending on the solvent polarity; in the case of Trp emission, spectra are red-shifted with increasing solvent polarity. Consequently, intrinsic fluorescence of proteins is an ideal probative method for protein folding and dynamics. For example, progress has been made in the early diagnosis of cataracts thanks to changes in Trp fluorescence in the ocular lens. Cataracts are caused by structural changes in the proteins of the ocular lens and are triggered by factors such as age and exposure to UV light[29] (see Chapter 5). Similarly, a unique fluorescence

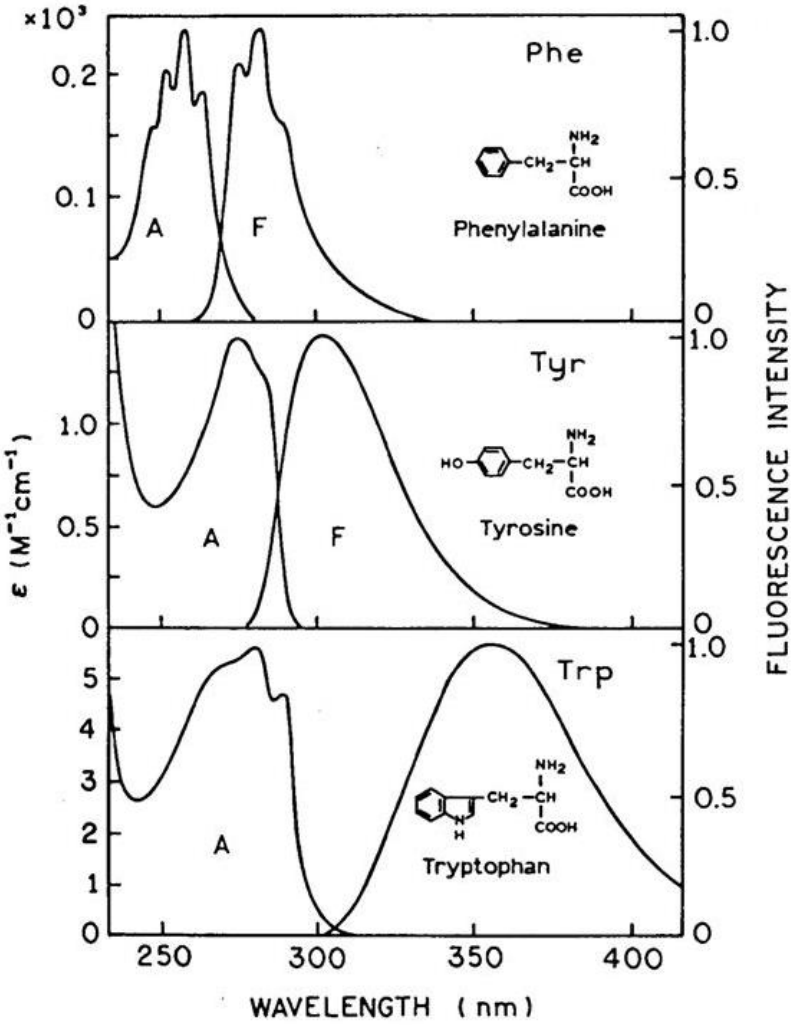

Figure 1.4c. Excitation and emission spectra of fluorescent amino acids with structures shown. Excitation spectra are located on the left of each graph and emission spectra on the right, separated by respective Stoke's shifts[9]

signature has been shown to develop in protein amyloids during aggregation[30]. Amyloids are clusters of misfolded proteins characteristic of neurodegenerative diseases such as CJD, Alzheimer's and BSE as mentioned previously. Studies of egg white lysozyme aggregation have shown that, as accretion progresses, the observed fluorescence increases due to the formation of β-sheets from lysozyme molecules.

1.4.2 Fluorescence Lifetime of Tryptophan

Lifetime values from intrinsic protein fluorescence are complex and diverse, varying by a factor of 100 between proteins[31]. Environmental conditions have been established as the main cause of this variation and include solvent polarity, temperature, number of tryptophan residues and tryptophan position and orientation within a protein. Accordingly, lifetime measurements are used to probe protein dynamics and reactions. Protein aggregation; which is implicated in pathological conditions such as CJD and Alzheimer's, has been monitored by Schlick *et al*[32] via intrinsic time resolved studies of Concanavalin A (Con A). It was observed that as aggregation increased, the Trp lifetime decreased i.e. Trp fluorescence was quenched. It was hypothesised that this was caused by protein-protein interaction and a possible change in conformation upon aggregation. Protein folding and unfolding can similarly be monitored. Anand and Mukherjee[33] have used a combination of steady state and time resolved fluorescence to monitor BSA unfolding and refolding in the presence and absence of a denaturant. It was observed that as denaturant concentration increased the Trp fluorescence intensity and lifetime decreased. This suggests that as BSA unfolds, exposure of Trp residues to the solvent results in fluorescence quenching. Upon refolding both the fluorescence intensity and lifetime increased to a similar value to that obtained before denaturation.

1.5 Proteins Studied

Proteins come in a wide range of sizes and conformations, with varying Trp contents and a multitude of Trp environments. Due to the sensitivity of Trp residues to the surrounding environment emission maxima can range from 308 nm (azurin) to 355 nm (glucagon) in solution[34], with Trp residues which are buried within the protein structure typically having an emission maximum of approximately 335 nm and those which are solvent exposed having an emission maximum of approximately 355 nm[35]. When studying protein fluorescence it is important to be able to understand the observed fluorescence characteristics in relation to protein structure. Accordingly, this section describes the structure of the proteins analysed and their relevance to this study.

1.5.1 Bovine Serum Albumin

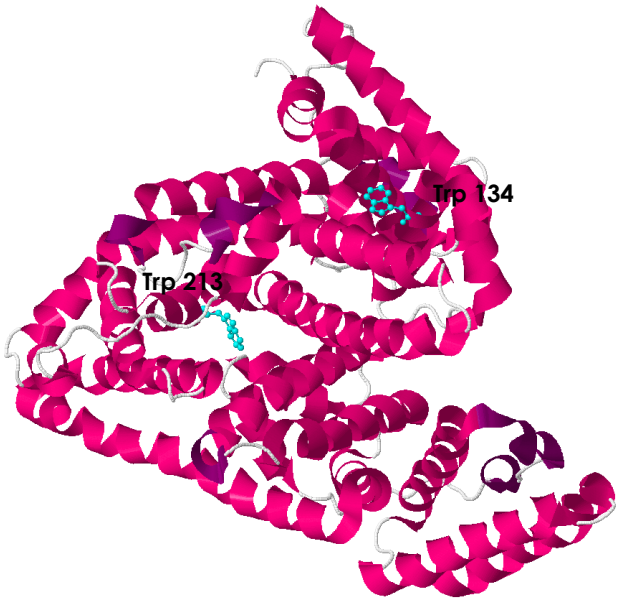

Figure 1.5a. Crystal structure of BSA showing its two tryptophan residues highlighted cyan (Structure downloaded from RSCB PDB Ref: 3V03)

BSA is a 66.5kDa protein involved in the transport of fatty acids and is the most abundant protein found in bovine blood plasma, accounting for approximately 55% of the protein content. This single chain of amino acids, which is 583 residues in length[36], carries out a multitude of functions including the binding and transportation of nutrients and the neutralisation of toxins. BSA is often used as a protein concentration standard and is particularly apt in the study described as there is 76% homogeneity between the primary structure of BSA and human serum albumin (HSA)[33,37]. HSA is the most abundant protein present in human blood plasma and is therefore likely to make up a large proportion of the protein contamination which adsorbs onto instruments during surgery. A fundamental difference between BSA and HSA is that the former contains two Trp residues whereas the latter contains only one[37], therefore, a lower fluorescence intensity is detected from HSA. Figure 1.5a shows the globular structure of BSA with its two Trp residues highlighted in cyan. Trp 134 is shown on the surface of the structure, which has been corroborated by solvent accessibility studies, whereas Trp 213 is buried within the structure. The difference in the environment of each Trp residue is evident in an experiment by Tayeh *et al*[38] in which solvent exposed Trp 134 was quenched using Calcolflour White. As the Calcofluor concentration was increased a shift in Trp

fluorescence was observed from 340 nm to 330 nm indicating the isolation of hydrophobic Trp 213 emission.

1.5.2 Bovine Fibrinogen

BFG is a 340kDa protein, containing 72 Trp residues[39] and makes up approximately 7% of blood plasma proteins and, compared to BSA, it is very large at 450 Å long. It comprises two sets of three alpha helical chains linked by a globular, N-terminal, central 'knob' with each end capped with globular C-terminal 'knots' (Figure 1.5b)[40]. In the presence of thrombin BFG molecules associate end to end to form long fibres which then associate laterally, with a half off-set arrangement, to form blood clots. Consequently, BFG is likely to be present in high concentrations at the area of surgical procedures. Also, due to its' size, BFG is a particularly 'sticky' protein and a study by Gettens and Gilbert[41] found that completely irreversible adsorption was observed between BFG and 316L stainless steel, the steel used in the manufacture of surgical instruments.

Figure 1.5b. Crystal structure of partially proteolized BFG showing the location of Trp residues (cyan) located in globular C-terminal 'knots' (Structure downloaded from RSCB PDB Ref: 1DEQ)

Figure 1.5b shows the crystal structure of modified BFG with the tryptophan residues highlighted in cyan. The distribution of Trp residues is concentrated in the flexible, globular 'knots' at either end of the molecule suggesting a variety of Trp environments. The properties of BFG and the high Trp content highlight the fact that BFG may be appropriate for use as a concentration standard in studies such as those described in Chapters 3 and 4.

1.5.3 Bovine γ-Globulins

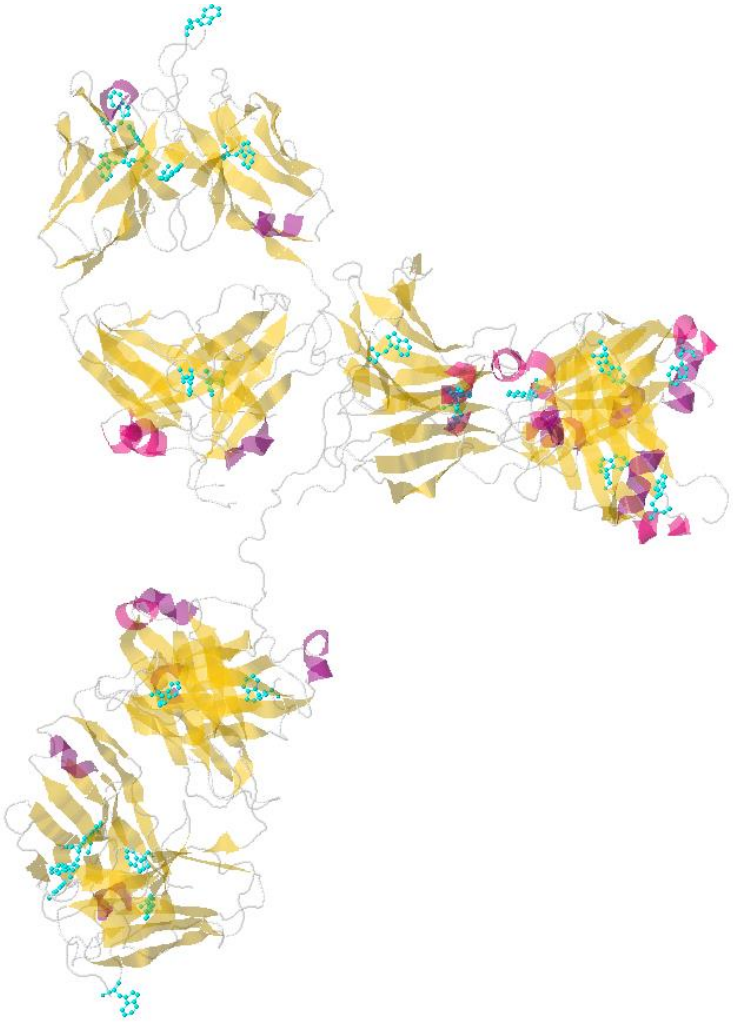

Figure 1.5c. Crystal structure of the human anit-HIV-1 antibody IgG1 b12 with Trp residues in cyan (Structure downloaded from RSCB PDB Ref: 1HZH)

γ-Globulins are globular proteins which make up approximately 36% of the proteins found in blood plasma. They are immune molecules which transport ions and lipids required for immune response and a number of γ-globulins are also known as immunoglobulins or antibodies[42]. The mixture of globulins used in this study have an average molecular weight of approximately 150kDa, although some γ-globulins can weigh up to 1200kDa. Figure 1.5c shows the crystal structure of the human anit-HIV-1 antibody IgG1 b12, with Trp residues highlighted cyan, showing that the majority of Trp residues are located centrally, buried within the β-sheet rich protein structure. Once again the prevalence of these proteins in blood plasma makes them appealing options as a standard for intrinsic detection of proteins. Moreover, as globulins are supplied as a mixture of proteins, the fluorescence observed may more

closely resemble that of a mixture of plasma proteins adsorbed onto the surface of a surgical instrument post-surgery.

1.5.4 Hen Egg-White Lysozyme

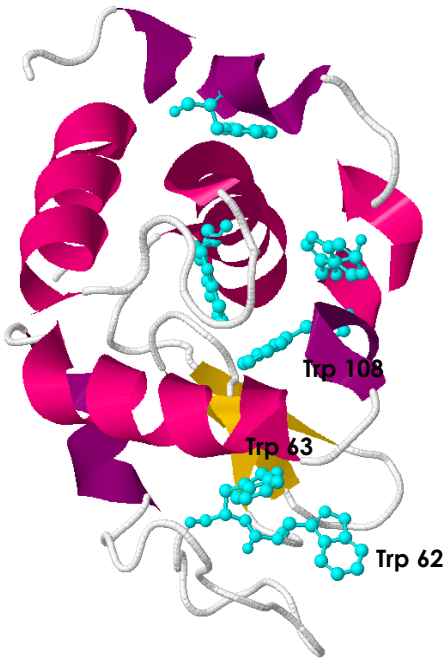

Figure 1.5d. Left - Crystal Structure of hen egg showing cyan Trp residues (Structure downloaded from RSCB PDB Ref: 1DPX)

Lysozyme is a small 14.3kDa globular protein containing only 129 residues and is the first enzyme to have its x-ray structure resolved. Lysozyme is a powerful enzyme which has the ability to damage the cell walls of many gram-positive bacteria and fungi species[43]. It is found largely in the saliva, tears and breastmilk, as a form of defence against bacterial infection. Figure 1.5d shows the crystal structure of hen egg-white lysozyme with its 6 Trp residues highlighted cyan. Trp residues 62, 63 and 108 surround the active site of lysozyme and are closer to the surface of the protein. This is evident when lysozyme is complexed and a blue shift in Trp emission is observed due to the newly hydrophobic/non-polar environment of residues 62, 63 and 108. It is proposed that the majority of lysozyme fluorescence can be attributed to these residues due to their less quenched positions within the protein[44]. Lysozyme has undergone extensive research into its structure and function and, as it is so well characterised, it is a possible candidate as a standard for the intrinsic detection of protein on surgical instruments.

1.5.5 Bovine Crystallins

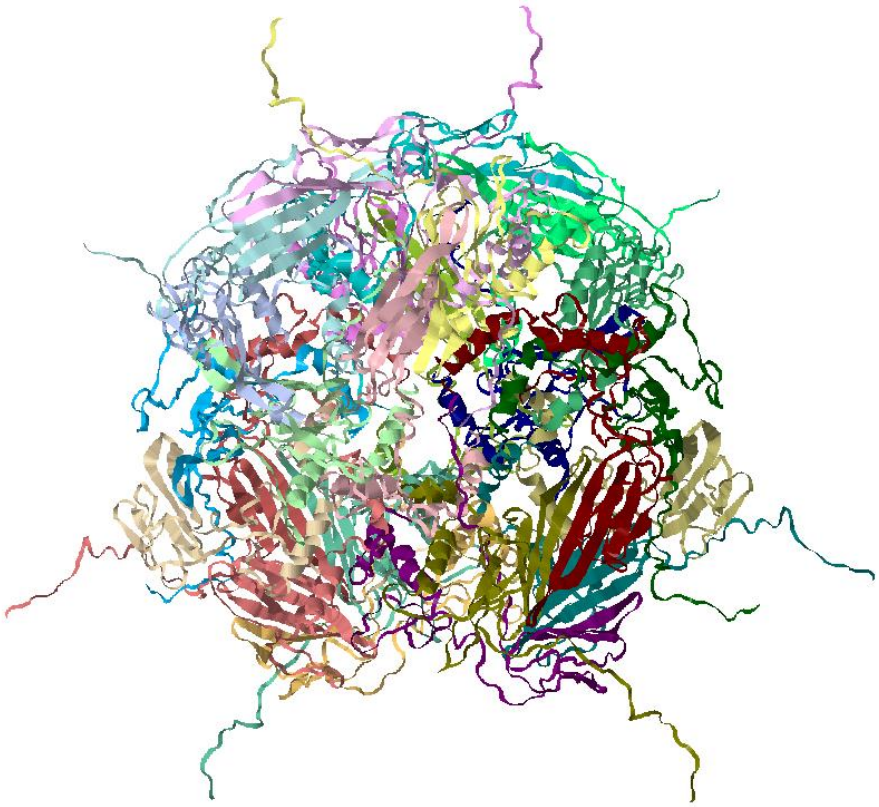

Figure 1.5e. Crystal structure of αB-crystallin 24mer (Structure downloaded from RSCB PDB Ref: 3J07)

Crystallins of the eye lens are unique proteins which have evolved the ability to remain in solution at high concentration without forming crystals. They are small proteins with α, β and γ-crystallins varying in size in the region of 20kDa (subunits), 46-200kDa and ~20kDa respectively. The lens is a concentrated solution of proteins of which crystallins compose 90% and this tightly packed and highly ordered mixture of α, β and γ-crystallins is what gives the lens its transparency[45]. α-Crystallins are the most common crystallins and are composed of two similarly structured subunits called the A and B chains, which contain one and two Trp residues, respectively. Alpha crystallins are found in multimeric complexes which, in the case of mammalian lenses, can rage in size from 600-900kDa[46]. Figure 1.5e shows the crystal structure of a spherical complex of 24 αB-crystallin molecules to highlight the close interaction of the protein molecules within the lens. γ-Crystallins are small monomeric proteins which act as molecular glue, allowing α-crystallins to associate into the aforementioned, multiunit complexes and for those complexes to associate[47]. γ-crystallins show similarity in their structures with α-crystallins, with the number of

Trp residues remaining reasonably consistent. Figure 1.5f shows the crystal structure of γF-crystallin. Although crystallins are not relevant as protein standards, their evolutionary resistance to photo-damage is relevant to the present studies of UV-induced changes in tryptophan fluorescence in crystalline proteins (Chapter 4), and to the potential use of fluorescence in cataract diagnosis (Chapter 5).

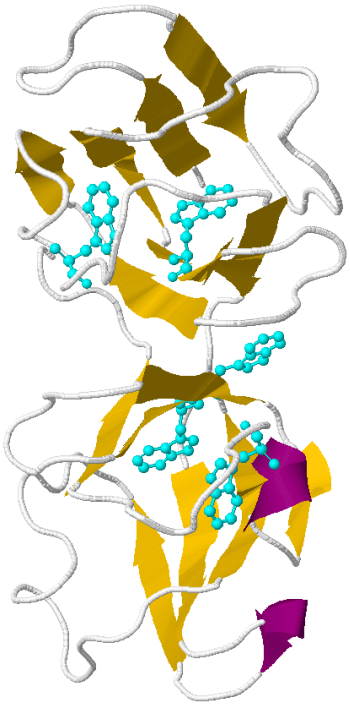

Figure 1.5f. Crystal structure of γF-crystallin with Trp residues in cyan (Structure downloaded from RSCB PDB Ref: 1A45)

1.6 References

1. The National CJD Research and Surveillance Unit – University of Edinburgh, Creutzfeldt-Jakob Disease in the UK, http://www.cjd.ed.ac.uk/documents/figs.pdf, [Accessed August 2016]

2. J. G. Descoteaux, E. C. Poulin, M. Julien and R. Guidoin, *AORN J*, 1995, **62**, 23-29.

3. A. Smith, M. Dickson, J. Aitken and J. Bagg, *J. Hosp. Infect.*, 2002, **51**, 233–235.

4. A. Smith, S. Letters, A. Lange, D. Perrett, S. McHugh and J. Bagg, *J. Hosp. Infect.*, 2005, **61**, 237–241.

5. H. Murdoch, D. Taylor, J. Dickinson, J. T. Walker, D. Perrett, N. D. H. Raven and J. M. Sutton, *J. Hosp. Infect.*, 2006, **63**, 432–438.

6. M. Vassey, C. Budge, T. Poolman, P. Jones, D. Perrett, N. Nayuni, P. Bennett, P. Groves, A. Smith, M. Fulford, P. D. Marsh, J. T. Walker, J. M. Sutton and N. D. H. Raven, *Br. Dent. J.*, 2011, **210**, E14, DOI: 10.1038/sj.bdj.2011.144.

7. G. W. Smith, F. Goldie, S. Long, D. F. Lappin, G. Ramage and A. J. Smith, *J. Foot Ankle Res.*, 2011, **4**, DOI: 10.1186/1757-1146-4-2

8. R. L. Baxter, H. C. Baxter, G. a Campbell, K. Grant, A. Jones, P. Richardson and G. Whittaker, *J. Hosp. Infect.*, 2006, **63**, 439–444.

9. World Health Organisation, *WHO Guidelines on Hand Hygiene in Health Care: A Summary*, WHO Press, 2009.

10. J. T Walker, *Decontamination in Hospitals and Healthcare*, Woodhead Publishing, 2014.

11. N. K. Nayuni, E. Cloutman-Green, M. Hollis, J. Hartley, S. Martin and D. Perrett, *J. Hosp. Infect.*, 2013, **84**, 97–102.

12. I. P. Lipscomb, H. E. Pinchin, R. Collin, K. Harris and C. W. Keevil, *J. Hosp. Infect.*, 2006, **64**, 288–292.

13. I. P. Lipscomb, H. Pinchin, R. Collin and C. W. Keevil, *J. Hosp. Infect.*, 2007, **65**, 72–77.

14. T. J. Secker, R. Hervé and C. W. Keevil, *J. Hosp. Infect.*, 2011, **78**, 251–255.

15. J. A Pezza and T. R. Serio, *Prion*, 2007, **1**, 36–43.

16. G. B. Dudhatra, K. Avinash, C. M. Modi, M. M. Awale, H. B. Patel, and D. K. Mody, *ISRN. Infect. Dis*, 2013, **2013**, 1-11

17. D. Riesner, *Br. Med. Bull.*, 2003, **66**, 21-33

18. J. D. F. Wadsworth, S. Joiner, J. M. Linehan, M. Desbruslais, K. Fox, S. Cooper, S. Cronier, E. A. Asante, S. Mead, S. Brandner, A. F. Hill and J. Collinge, *Proc. Natl. Acad. Sci. U. S. A.*, 2008, **105**, 3885–3890.

19. T. R. Appel, M. Wolff, F. von Rheinbaben, M. Heinzel and D. Riesner, *J. Gen. Virol.*, 2001, **82**, 465–473.

20. T. Mok, Z. Jaunmuktane, S. Joiner, T. Campbell, C. Morgan, B. Wakerley, F. Golestani, P. Rudge, S. Mead, H. R. Jäger, J. D.F. Wadsworth, S. Brandner and J. Collinge, *N. Engl. J. Med.*, 2017, **376**, 292-294

21. Lakowicz, J. R., *Principles of Fluorescence Spectroscopy*, New York: Springer, 2006

22. Atkins, P. and De Paula, J., 2010, *Physical Chemistry*, Oxford University Press

23. P. J. Brescia Jr. and P. Banks, *BioTek: High Resolution Fluorescence Microscopy of PtK2 Cells Undergoing Mitosis in Microplates*, 2014, https://www.biotek.com/assets/tech_resources/Mitosis_App_Note.pdf, (Accessed November 2016)

24. C. Levinthal, *Extr. du J. Chim. Phys.*, 1968, **65**, 44.

25. A. Sali, E. Shakhnovich and M. Karplus, *Nature*, 1994, **369**, 248–251.

26. R. Zahn, A. Liu, T. Luhrs, R. Riek, C. von Schroetter, F. L. Garcia, M. Billeter, L. Calzolai, G. Wider, and K. Wuthrich, *PNAS,* 2000, **97**, 145–150.

27. C. Govaerts, H. Wille, S. B. Prusiner and F. E. Cohen, *PNAS*, 2004, **101,** 8342–8347

28. M. R. Eftink, *Method. Biochem. Anal.,* 1991, **35**, 127-205

29. D. M. Gakamsky, B. Dhillon, J. Babraj, M. Shelton and S. D. Smith, *J. R. Soc. Interface*, 2011, **8**, 1616–1621.

30. F. T. S. Chan, G. S. Kaminski Schierle, J. R. Kumita, C. W. Bertoncini, C. M. Dobson and C. F. Kaminski, *Analyst*, 2013, **138**, 2156–2162.

31. J. R. Alcala, E. Gratton and F. G. Prendergast, *Biophys. J.*, 1987, **51**, 597–604.

32. K. H. Schlick, C. K. Lange, G. D. Gillispie and M. J. Cloninger, *J. Am. Chem. Soc.*, 2009, **131**, 16608–16609.

33. U. Anand and S. Mukherjee, *Biochim. Biophys. Acta*, 2013, 1–11.

34. J. T. Vivian and P. R. Callis, *Biophys. J.*, 2001, **80**, 2093–2109

35. L. A. Munishkina and A. L. Fink, 2007, *Biochim. Biophys. Acta.*, 1768, 1862-1885

36. Y. Moriyama, D. Ohta, K. Hachiya, Y. Mitsui and K. Takeda, *J. Protein Chem.*, 1996, **15**, 265–272.

37. E. L. Gelamo and M. Tabak, *Spectrochim. Acta. A. Mol. Biomol. Spectrosc.*, 2000, **56A**, 2255–2271.

38. N. Tayeh, T. Rungassamy, J. R. Albani, *J. Pharm. Biomed. Anal.*, 2009, **50**, 107-116

39. S. Gonçalves, N. C. Santos, J. Martins-Silva and C. Saldanha, *J. Photochem. Photobiol. B.*, 2007, **86**, 170–176.

40. J. H. Brown, N. Volkmann, G. Jun, A. H. Henschen-Edman and C. Cohen, *PNAS*, 1999, **97**, 85–90

41. R. T. T. Gettens and J. L. Gilbert, *J. Biomed. Mater. Res. Part A*, 2006, 465–473.

42. M. Nag, D. Das, D. Bandyopadhyay and S. Basak, *Phys. Chem. Chem. Phys.*, 2015, **17**, 19139–19148.

43. R. Swaminathan, V. K. Ravi, S. Kumar, M. V. S. Kumar and N. Chandra, *Adv. Protein Chem. Struct. Biol.,* 2011, **84**, 63-111

44. T. Imoto, L. S. Forster, J. A. Rupley, and F. Tanaka, *PNAS*, 1974, **69**, 1151–1155

45. N. Schafheimer and J. King, *Photochem. Photobiol.*, 2013, **89**, 1106–1115.

46. J. Horwitz, M. P. Bova, L. L. Ding, D. A. Haley and P. L. Stewart, *Eye*, 1999, **13**, 403-408

47. L. Takemoto and C. M. Sorensen, *Exp. Eye Res.*, 2008, **87**, 496–501.

Chapter 2: Experimental

The spectroscopic techniques used throughout this work are described here. Experimental details specific to the studies reported in each chapter are presented in the individual Materials and Methods sections.

2.1 Samples

For spectroscopic measurements, unless stated otherwise, solution-phase samples were contained in a fused silica micro-cuvette with a capacity of 400µL and a path-length of 1 cm. Solid-state sample preparation is described in the appropriate chapters. All experiments were carried out at room temperature.

2.2 Absorption Spectroscopy

UV-visible absorption spectra were recorded using a Varian Cary 50 Bio UV-Visible Spectrophotometer and spectra were processed and analysed using Cary WinUV software.

2.3 Steady State Fluorescence Spectroscopy

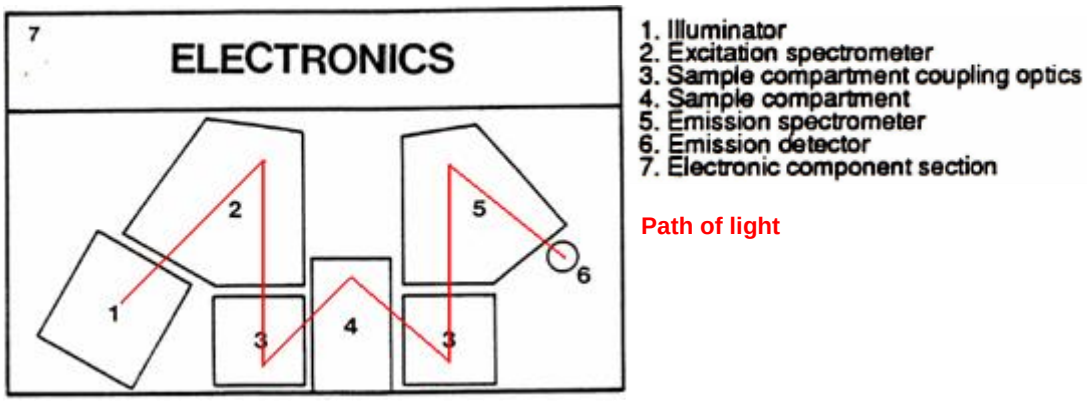

Figure 2.3a. System layout of FluoroMax-2 spectrofluorometer showing excitation and emission light paths[1]

Steady state fluorescence spectra were measured using a Fluoromax-P spectrofluorometer (Horiba Jobin-Yvon) in conjunction with the associated

FluorEssence™ software v.3.5. The basic layout of the fluorometer components is shown in Figure 2.3a. Light produced from the 150W continuous ozone-free Xenon lamp in compartment 1 is directed to the entrance slit of the excitation monochromator. The spectrofluorometer is equipped with Czerny-Turner spectrometers in both the excitation and emission arms, allowing for the acquisition of excitation and emission spectra. Before entering the sample compartment, a beam splitter directs 8% of the excitation light to a reference photodiode to account for differences in light intensity with changing wavelength and with time. The remaining light enters the sample compartment and excites the sample within. Fluorescence emission from the sample is collected at a right angle to the incident light and directed to the emission monochromator. Wavelength-resolved light exiting the emission monocrhomator is detected by a photon-counting photomultiplier which amplifies the signal of the low intensity light produced by the sample.

The entrance and exit ports of each monochromator have slits which control the bandwidth (and intensity) of the light entering the sample compartment (excitation) and the light detected by the photomultiplier (emission). The operation of the spectrometer was controlled by the associated Datamax software. Slit widths were set at a bandwidth of 5 nm for both excitation and emission unless stated otherwise. The wavelength increment, which determines the number of data points in a spectrum, was set to 1 nm and the integration time, i.e. the time for which photons are counted at each wavelength increment, was set typically to 1 second. Generally, integration time is increased with decreasing emission intensity to improve the signal-to-noise ratio collected from low intensity samples.

2.4 Time Resolved Fluorescence Spectroscopy

Acquisition of fluorescence decay data was carried out using a time-correlated single photon counting system (Edinburgh Instruments Ltd) in combination with a mode-locked Ti:sapphire laser system (Coherent Ltd), in the Collaborative Optical Spectroscopy, Micromanipulation and Imaging Centre (COSMIC) facility at The University of Edinburgh. The experimental system is shown schematically in Figure 2.4a.

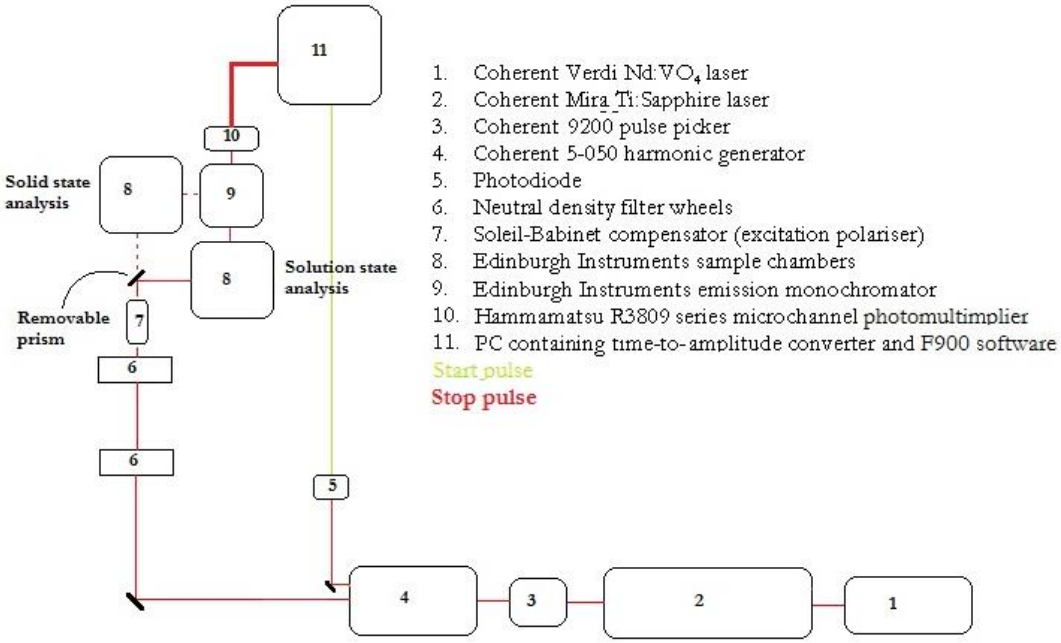

Figure 2.4a. Schematic of equipment used for acquisition of fluorescence decay data[2].

Excitation light was produced by a mode-locked Ti:Sapphire laser (2) which was pumped by a Neodymium:Vanadate (Nd:YVO4) continuous wave solid state laser (1). The power of the Nd:YVO4 laser was 9W throughout lifetime acquisition. The Ti:Sapphire laser produces pulsed light at a repetition rate of 76 MHz and a pulse width of 200fs. Using a Coherent 9200 pulse picker (3) the repetition rate was reduced to 4.75 MHz resulting in pulse emission every 210 ns. The excitation light then travelled to a harmonic generator (4) which acts to double or triple the frequency and so reduce the wavelength of the light, allowing for selection of the desired excitation wavelength. The light exiting the harmonic generator was split and approximately 10% was diverted to a fast photodiode (5) triggering the START pulse which then triggered the time-to-amplitude converter (TAC). The intensity of the laser light was controlled using neutral density filters (6).

Vertically polarised excitation light was obtained using a Soleil Babinet Compensator (7) the position of which is dependent on the wavelength of excitation light. To ensure the compensator was in the correct position a resolution value was set for each wavelength using Edinburgh Instrument's (EI) F900 software which was used to set the parameters for each experiment. Equation 6 shows the relationship between resolution and wavelength.

$$R = 41.62/\lambda \qquad \text{Equation 6}$$

The vertically polarized light was directed to the sample chamber (8) and aligned in the centre of the excitation window of a 400 µL capacity fluorescence cuvette. Emission light from the sample, collected at 90º to the excitation light, was passed through a polarizer set at an angle of 54.7º (the 'magic' angle) to remove any anisotropic effects from data collected. The emission wavelength was set using an EI M300 monochromator (9). To ensure no scattered light was detected during lifetime acquisition a bandpass filter was placed between the sample and monochromator. Fluorescence photons were detected using a Hamamstu R3809-50 microchannel plate photomultiplier (MCP) (10) and the STOP signal for the TAC was produced upon emitted photons striking the MCP.

Upon starting up the apparatus the system was optimised and the instrument response function (IRF) taken using a Ludox (colloidal silica) scattering solution which was contained in a 5 ml capacity fused quartz cuvette. Before taking the IRF the count rate of Ludox was reduced to the range of that of the sample, using the neutral density filters. These were also used to ensure that no sample gave a count rate above 30, 000 Hz which would result in damage to the MCP. The typical IRF for the system was 85ps full width at half maximum (FWHM). Steady state spectra were recorded, using an EI photon counting photomultiplier tube, to ensure the excitation light was at the correct wavelength and emission was recorded at the correct wavelength.

The collection of fluorescence decays was controlled using EI F900 software which allowed for experimental parameters to be set. Decay curves had a resolution of 4096 channels over a time range of 50ns, and signal was accumulated until 10,00 counts were reached in the maximum channel. Fitting of decay data was carried out using EI FAST software, using an iterative least-squares, reconvolution routine. The fitting range of the decay curves was from the maximum of the IRF to the point at which photon counts fell to 100 (10% of the maximum channel). The background level was fixed during the fitting and was determined from the average number of counts in channels before the rising edge of the decay curve (typical <5 counts). The magnitude and randomness of residuals and the value of the reduced χ^2 were used as criteria to determine the adequacy of the fit.

2.5 References

1. HORIBA, Jobin and Yvon Inc., *FluoroMax Spectrofluorometer – Operation and Maintainance*, SPEX Industries Inc., New Jersey

2. R. Neely, PhD thesis, The University of Edinburgh, 2005

Chapter 3: The Detection of Residual Protein on Surgical Instruments using an Epifluorescence Surface Scanner

3.1. Introduction

Current methods for detecting residual protein on reprocessed surgical instruments involve swabbing the instrument and observing a colour change as protein, which has been removed from the surface, reacts with a protein-specific reagent. Although such methods give a semi-quantitative result, as often the colour change is quicker and more intense as protein amounts increase, it has been shown that they are ineffective at detecting surface-bound protein which has not be removed during the cleaning process, therefore, significantly underestimating the amount of protein present. The limit of detection of the commonly used ninhydrin swab test was determined by Lipscomb *et al*[1] to be 9.25 μg of protein per cm^2, based on measurements of test samples consisting of mouse-brain homogenate deposited on stainless steel tokens. However, a more recent study by Nayuni *et al*[2] reported that the sensitivity obtained by Lipscomb *et al* was significantly overestimated because of the presence in brain homogenate of substantial quantities of free amino acids; the response of ninhydrin to amino acids is 40-fold more sensitive than its response to intact protein. Moreover, the latter study showed that a commercial ninhydrin test kit yielded negative results for test instruments that had visually detectable protein deposits. Taking these findings into consideration, a sensitive and quantitative method is required to ensure the safety of re-usable instruments but also to assess the standard of single use-instruments.

The need for quantitative protein detection techniques in Sterile Services Departments (SSDs) is reflected in recently updated guidance from the Department of Health on the management and decontamination of surgical instruments (medical devices) used in acute care, Health Technical Memorandum (HTM) 01-01, published in July 2016[3]. HTM 01-01 has been updated to take account of recent changes to the Advisory Committee on Dangerous Pathogens Transmissible Spongiform Encephalopathy (ACDP-TSE) Subgroup's general principles of decontamination, and requires that there should be ≤5 μg (BSA equivalent) of protein *in situ* on the side of any instrument tested. The guidance indicates that protein levels on an instrument

should be measured directly on the surface rather than by swabbing or elution as detection of proteins on the surface of an instrument gives a more appropriate indication of cleaning efficacy related to prion risk. This is because prion proteins are very hydrophobic and will, once dry, adhere strongly to surfaces and resist removal by swabbing or elution. Fluorescence is widely used in the life sciences as a non-destructive method for analysing biological systems, either via intrinsic fluorescence native to the molecule of interest or by labelling a molecule with an extrinsic fluorescent probe.

The sensitivity of fluorescence and specificity of binding of fluorescent probes makes the *in situ* fluorescence detection of residual protein on surgical instruments the methodology of choice. This chapter describes the use of the epifluorescence surface scanner (EFScan), in combination with *in situ* fluorescent labelling of the protein molecules with the fluorescein fluorophore, through reaction with fluorescein isothiocyanate (FITC), to quantify the amount of protein contamination on unused, single-use surgical instruments. Single-use (disposable) instruments are used clinically in the expectation that they offer superior cleanliness, and hence reduced risk, compared with reprocessed instruments. However, as shown in this chapter, single-use instruments may carry significant levels of protein contamination and may fail to meet the upper limit of 5 μg/side specified in HTM 01-01.

3.1.1. Surgical Instrument Manufacture

The first step in surgical instrument cleanliness is a high standard of manufacture, however, approximately 80% of the world's supply of surgical instrument are

Figure 3.1a. L+R - Images depicting the conditions under which the majority of the world's surgical instruments are manufactured[5]

manufactured in the sweatshops of Sialkot, Pakistan[4]. Conditions within these, often unlicensed, factories are unclean and unsafe. Figure 3.1a shows some of the working conditions within one of these factories showing operatives, some as young as 7, wearing no protective equipment and no gloves to protect surgical instruments from biological contamination. Although these instruments are processed to some degree following manufacture and often sterilised before use, sterile does not equate to clean. Analysis of the quality of surgical instruments procured for use in the UK found that 15% of instruments arrived with manufacturing defects including machining burrs and debris in the teeth of clamp devices[6], which could lead to severe

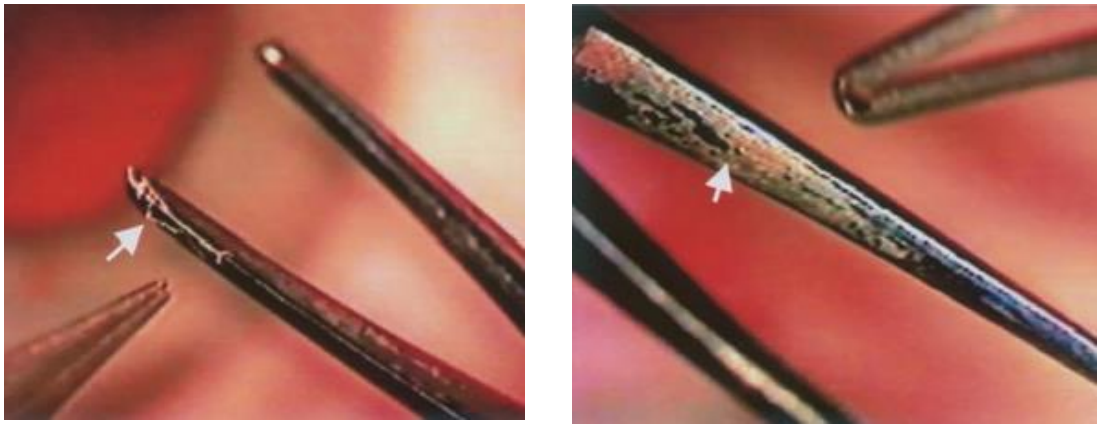

Figure 3.1b. Debris photographed before use in surgery on intra-ocular lens (IOL) introducers Left: Loose fibre attached to tip of IOL introducers, Right: Biological debris on the inside of IOL introducers[9]

surgical complications. This is particularly true in terms of ocular surgery in which cases of debris on processed instruments can lead to irritation and infection[7,8]. A number of cases have been reported in which machining burrs and, in one case, the tip of an instrument have been left in patients eyes following surgery. Following decontamination and sterilisation, debris is still an issue, including biological contamination. A study by Dinakaran and Kayakar[9] found that deposits, including loose fibres and biological deposits, were found in 62% of the 47 trays of reprocessed and in-use ocular surgical instruments analysed during the investigation (Figure 3.1b). Instruments were analysed by the surgeon under the operating microscope before use and any unusable instruments were rejected, however, the criteria for rejection was not reported meaning the instruments shown in Figure 3.1b may have been used for surgery. In a subsequent study by Leslie *et al*[8] debris flushed from phacoemulsification handsets was analysed via SEM imaging and it was found that bacterial colonies, squamous cells and fungal hyphae were identified among the debris. The implications of debris alone in surgical complications is perturbing,

however, biological deposits are more worrying still. Some bacteria and viruses and, as detailed in Chapter 1, prions are resistant to sterilisation procedures, therefore, subsequent studies on the quality of instrument manufacture and decontamination have aimed to determine the composition of biological debris, such as that shown in Figure 3.1b (Left), with the aim of detection and quantification of the material.

3.1.2. Early Total Protein Detection Experiments

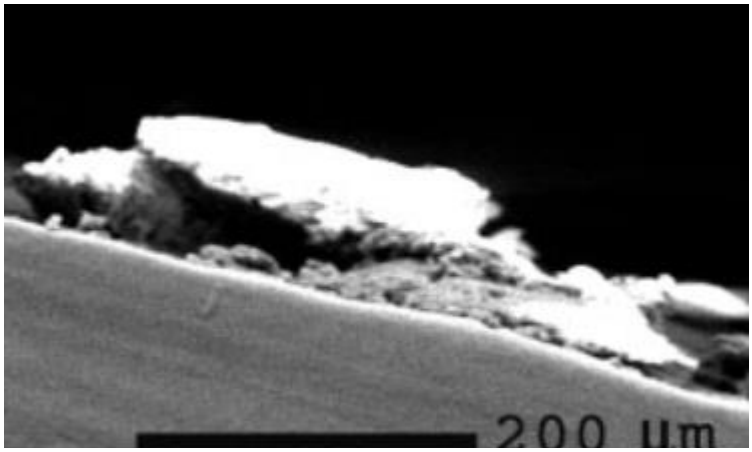

Figure 3.1c. A SEM image showing a thick deposit of protein on the blade of an instrument[5]

Early research at The University of Edinburgh, led by Baxter (Robert), Baxter (Helen) and Jones, focused on the use of argon:oxygen RF gas-plasma cleaning as a superior method of surgical instrument decontamination[10-12]. Initial analysis of the efficiency of the procedure involved scanning electron microscopy (SEM) to view deposits and energy-dispersive X-ray analysis (EDX) to identify the composition of the deposits. All of the instruments analysed had been cleaned to the standard of hospital SSDs before analysis; however, Figure 3.1c shows the extent of the contamination remaining on some of the instruments. EDX analysis showed that the majority of the contamination contained carbon, nitrogen, oxygen, sulfur, which is indicative of protein contamination. This combination of methods successfully located and identified proteinaceous contamination on surgical instruments; however, they do not give a quantitative understanding. Acid stripping studies followed, in which the surface of instruments were stripped and the washings analysed to give a quantitative measure of contamination. The amount of protein present ranged from 0 (although it should be noted that this was only the case for one instrument) to over 1000 µg/instrument, which is of the order of 10^{16} protein molecules, assuming a molecular mass of 10^5 Da. Although the complete removal of surface contamination

is probable, this method is not suitable for quality control in clinical SSDs as instruments are destroyed during stripping. Consequently, fluorescence analysis was chosen as a non-destructive and quantitative method for studying proteinaceous contamination via the detection of protein labelled with FITC.

3.1.3. Fluorescein

Fluorescein is a widely used fluorescent probe which exists in seven prototropic forms in aqueous solution over the pH range 1-10[13]. This prototropy occurs as a function of pH to which the intensity of fluorescein fluorescence is highly sensitive[13-16] (Figure 3.1d). Over the pH range 6-10 only the monoanion and dianion contribute to the fluorescence intensity[16]. As the pH increases the abundance of the dianion increases and so does the fluorescence. This is because the quantum yield of the dianion is 0.93 compared with 0.36 for the monoanion[13]. The photo-physics of fluorescein make it an ideal protein label as its excitation and emission wavelengths (λ_{ex} = 480 nm, λ_{em} = 510nm) do not overlap significantly with those associated with biomolecules, which tend to absorb in the UV region. Moreover, the isothiocyanate derivative of fluorescein (FITC) binds specifically and covalently to the amino terminal and primary amines of proteins[14,17]. The efficacy of FITC for the labelling of surface-bound protein was validated using a combination of SEM and fluorescence microscopy, as illustrated in Figure 3.1e.

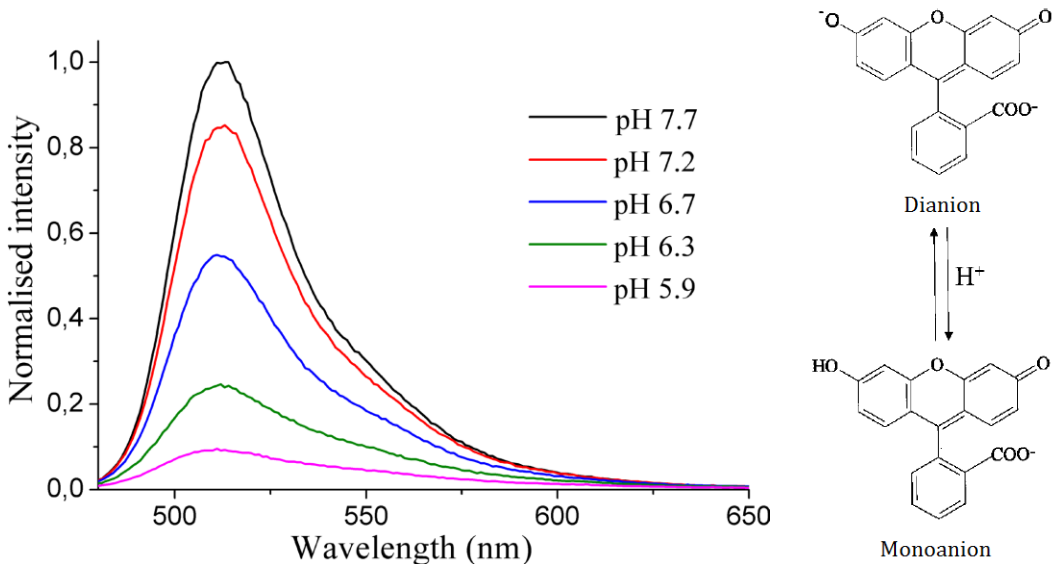

Figure 3.1d. pH dependence of fluorescein fluorescence and the structure of fluorescein monoanion and dianion[10]

SEM imaging was used to determine the spatial distribution of protein contamination prior to labelling, as exemplified in the left-hand image, which shows the tips of a surgical clamp. The protein appears as dark areas in the SEM as confirmed by elemental analysis using energy dispersive X-ray spectroscopic analysis. A fluorescence micrograph of the same area of this instrument, following FITC labelling, is shown in the right-hand image. It can be seen that there is excellent correspondence between the two images, confirming that the fluorescent labelling of the protein is effective and selective, with no detectable, non-specific adsorption of fluorophore on the protein-free metal surface.

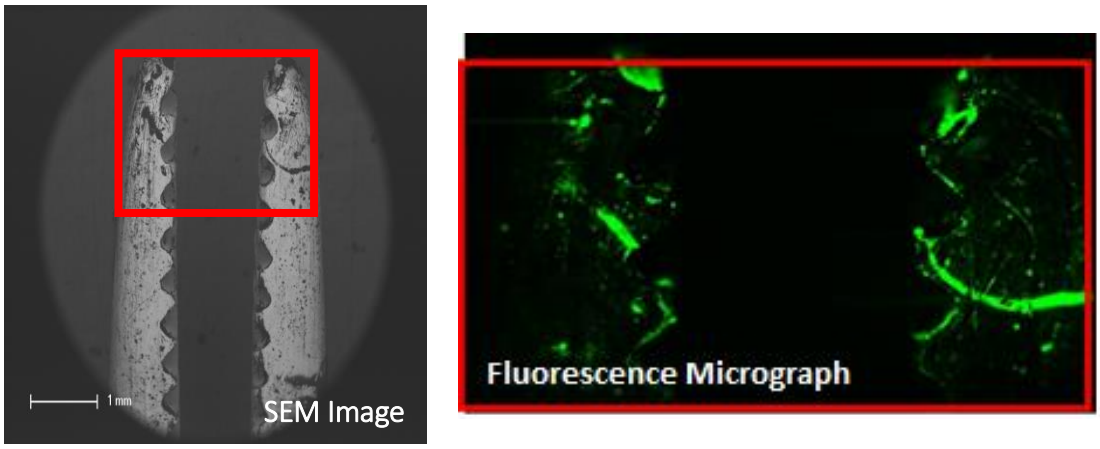

Figure 3.1e. The left-hand image shows a scanning electron micrograph of the tips of a surgical clamp prior to FITC labelling (scale bar 1 mm). The right-hand image shows a fluorescence micrograph of the area outlined in red in the SEM image, after FITC labelling.

3.1.4. The Epifluorescence Surface Scanner

The EFScan used in these studies is a commercial prototype system that was developed in partnership with Edinburgh Biosciences Ltd. Its design was based on a laboratory-built system that was developed previously in the Jones and Baxter groups at Edinburgh[18]. The EFScan (Figure 3.1f) comprises a fixed optical head, incorporating an LED excitation source and a photomultiplier detector, beneath which a scanning bed, on which the sample is mounted, is moved under computer control to build up a 2D raster image of the scanned area (maximum 110 x 72 mm^2). Software in the host computer captures and processes the fluorescence data to produce a 48x32 pixel image of the spatial distribution of fluorescence intensity over the scanned area. The pixel dimensions are 2.25 x 2.25 mm^2. This process takes approximately 15 minutes.

Figure 3.1f. The EFSCAN system. Top - the complete system, comprising the detection unit (optical head and scan bed), on the left, and the power supply/control units and laptop PC, on the right and Bottom - surgical instruments loaded on the scanning bed

The optical head employs an epifluorescence geometry, in which excitation and detection are conducted through the same objective lens, as illustrated in Figure 3.1g. This ensures exact coincidence of excitation and detection areas and enables efficient and quantitative detection of fluorescence intensity. This arrangement is based on a standard "filter cube", as used in fluorescence microscopes, which incorporates excitation and emission filters and a dichroic mirror to spectrally separate the fluorescence from scattered/reflected excitation light and prevent the latter from reaching the detector. The rejection of scattered/reflected excitation light is a major challenge to the sensitive detection of fluorescence from molecules on a metal surface, such as a surgical instrument. This is achieved in the EFSCAN system by the use of bandpass filters with an extremely high extinction ratio combined with an extremely high transmittance (~99%).

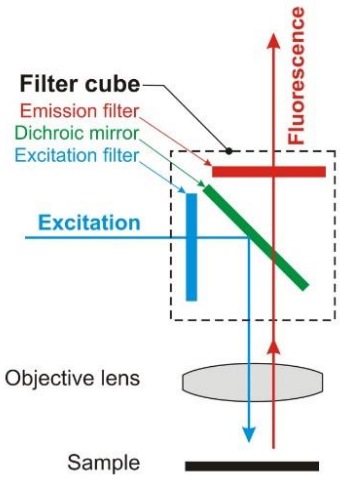

Figure 3.1g. Schematic diagram of the epifluorescence arrangement in the optical head, based in a standard filter cube

The spectral profiles of the filters and LED source, together with absorption and emission spectra of FITC are shown in Figure 3.1h. The excitation filter selects a band of wavelengths between 465 nm and 500 nm from the output of the LED source, cutting off the long wavelength 'tail' of the LED output that extends into the wavelength range of the FITC fluorescence. The dichroic mirror reflects wavelengths below 500 nm (the excitation light) and transmits wavelengths above 510 nm (the fluorescein fluorescence). The emission filter transmits a band of wavelengths from

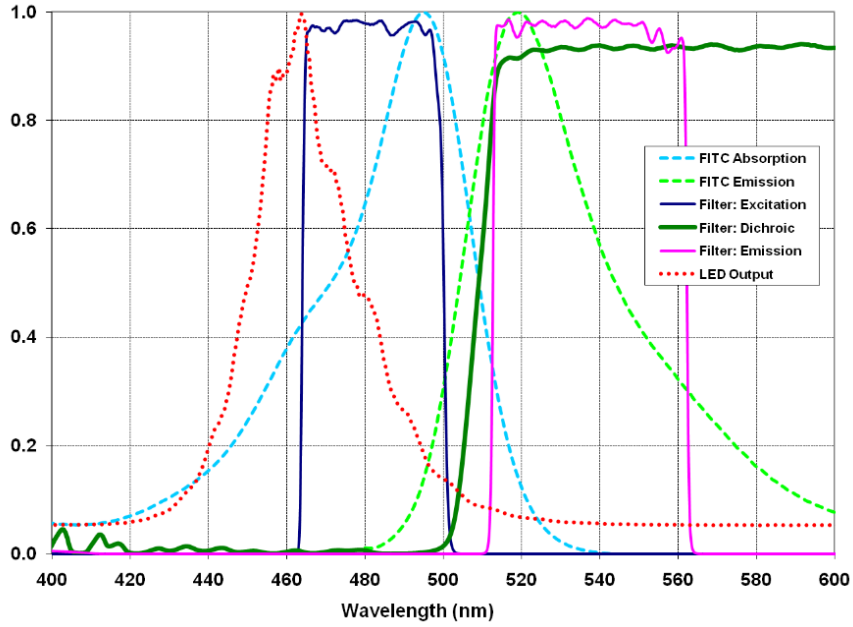

Figure 3.1h. Normalised plots of the absorption and emission spectra of the fluorescein fluorophore (dashed blue and green lines), the transmission plots for the excitation, dichroic and emission filters, and the measured spectral output of the LED array (dotted red line)

510 nm to 560 nm, covering the majority of the fluorescein emission spectrum. The complete optical system is shown in Figure 3.1i. The excitation arm contains the source, a lightweight packaged LED array device, collection lenses (L_1 and L_2), and a diffuser plate which is used to minimise the structure of the LED array at the sample plane. Two adjustable irises and additional lenses (L_3 and L_4) are used, in conjunction with the objective, to control the intensity of the illumination, and the beam diameter of the excitation illumination at the sample plane. The objective lens (NA ~ 0.5) is common to both the excitation and emission channels and collects the emitted fluorescence onto the 8 mm diameter effective area of the photomultiplier. With the need for only weak focussing of the emission, this means that the detection sensitivity is tolerant to variation of the distance between the sample surface and the optical head, within a range of a few mm, allowing for reliable measurements on surfaces which are not flat. The photomultiplier detector provides very high sensitivity combined with a large dynamic range. There is provision for the inclusion of additional filters in the excitation and emission arms, over and above those incorporated in the standard filter cube, to enhance discrimination against scattered excitation light. In the present work, a single excitation filter and two emission filters were used. The EFScan system employs phase-sensitive detection to render the detector insensitive to stray ambient light. Phase sensitive detection allows for amplification of a specific signal of interest by reducing noise outwith the range of the signal of interest. This is done by modulating the input signal at a reference frequency while the system measures the response from the sample at the specified

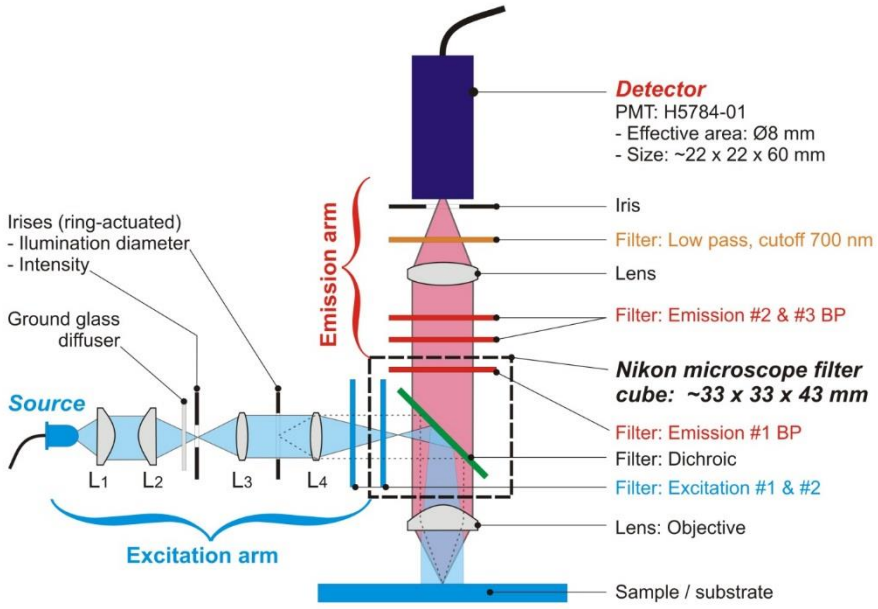

Figure 3.1i. Schematic diagram of the layout of the components of the optical head.

reference frequency, allowing for any noise, which is at a different frequency or phase to the signal of interest, to be identified and attenuated to zero. This enables the EFScan system to be used in normal room light without the need to make the scanning bed assembly light-proof. In the EFScan system phase-sensitive detection is achieved by modulating the output of the LED at 1 kHz and recording the output from the photomultiplier synchronously with the modulated excitation.

The Output

The raw data from the EFScan consists of a matrix of fluorescence intensity values, which is displayed in the form of a simple colour-coded, pixelated image on the laptop PC as the scan proceeds, as illustrated in Figure 3.1j. This gives an immediate indication of protein coverage and identification of hotspots. The numerical data are also exported to an Excel spreadsheet to allow for processing of the data to establish the amount of protein on the instrument. A detailed description of the calibration and data analysis is given in Section 3.2.

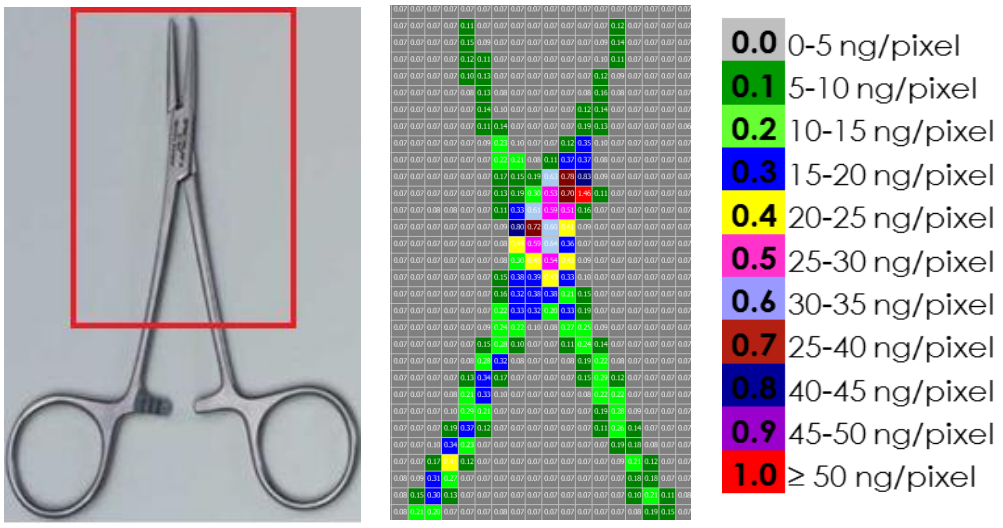

Figure 3.1j. Typical output of the EFScan system. The left-hand image indicates the area of the instrument scanned. The right hand image shows the raw data in the form of colour-coded pixels, where the colours indicate the level of protein (BSA equivalent) per pixel, according to the scale shown.

FITC-BSA was chosen as a simple, reproducible, commercially available protein standard for calibration of the EFScan. BSA is commonly used as a protein concentration standard; it has a molecular weight of 66,463 Da and consists of 583 amino acid residues. Inevitably, calibration involves the use of a model protein system, since the composition of the real protein residue on surgical instruments is

unknown. BSA is arguably a good model system, since serum albumin is the most abundant protein in blood plasma (the normal concentration of human serum albumin in blood is 0.5-0.8 mM). Nevertheless, it is important to recognise that the protein loads on surgical instruments that are reported in the present studies are expressed as FITC-BSA equivalents, i.e. the amount of FITC-BSA that would give a fluorescence intensity equivalent to that measured.

Previous Results of the EFScan System

Quantitative assessment of the efficiency of plasma cleaning resulted in a comprehensive study from the Baxter and Jones group (Edinburgh) which utilised SEM, EDX and EFScan analysis of a selection of reusable instruments. Comparison of EFScan data before and after decontamination showed that over 99% of the proteinaceous contamination had been removed[18]. Further work from the group examined a variety of instruments, including reprocessed, retired-from-use instruments from Edinburgh Royal Infirmary and reprocessed, in-use instruments from several SSDs in Scotland; this work is unpublished but has been reported to DH in Final Report reference 007/0204. For the retired-from-use instruments, total protein load (on one surface) ranged from 170 ng to 11.8 μg (FITC-BSA equivalent). 33% of instruments had a total protein load less than 1 μg, 65% had less than 2 μg, 80% had less than 3 μg and 90% had less than 4 μg. For the in-use instruments, the level of residual protein contamination was significantly less than for the retired instruments; 61% of the in-use instruments had a total protein load of less than 1 μg, compared with 33% of the retired instruments.

3.1.5. Alternative Methods for the Evaluation of Protein Residue on Surgical Instruments

Under the auspices of the same DH-funded research programme that supported development of the EFScan system, two other groups have developed and applied fluorescence-based methods for *in situ* detection of residual protein on surgical instruments. Keevil *et al*, University of Southampton, developed an episcopic differential interference contrast microscope and Perrett *et al*, Queen Mary University, London, developed a CCD-based detection system in combination with the o-phthaldialdehyde (OPA) protein detection reagent.

Episcopic Differential Interference Contrast/Epifluorescence (EDIC/EF) Microscopy

The Keevil group from the University of Southampton have carried out several studies on the detection and quantification of proteinaceous residue on a variety of surgical instruments[19-22]. Preliminary studies involved the use of SYPRO ruby in conjunction with epifluorescence microscopy to identify areas of protein contamination. Gross contamination was observed using episcopic differential interference contrast microscopy. Sampling was performed on distinct test areas of each instrument and the degree of contamination was established by implementation of a visual contamination index (0-4); where 0 indicates no detectable contamination and 4 indicates substantial soiling (>4.2 µg mm^{-2})[19]. Eight independent volunteers assessed the degree of contamination based on five photographed standards representing the 5 levels in the contamination index. These were compared to the test areas on the instruments. The method has since evolved to include Thioflavin T, which binds exclusively to amyloid deposits characteristic of CJD, resulting in a dual stain procedure capable of discerning between infectious and non-infectious protein contamination. The same scoring method as to the degree of contamination was used in these studies. Results show that at least 66% of instruments tested in all cases showed soiling at level 2 (42-420 ng mm^{-2}) or above on at least one of the test areas[19-21]. Dual stain studies on test instruments artificially contaminated with ME7 (murine scrapie) infected mouse brain homogenate have shown that, of the total protein contamination observed approximately 7% was identified to be amyloid[22]. These studies have utilised sophisticated detection and labelling techniques and produced results which support previous contamination studies, however, data analysis techniques could be improved. Visual inspection allows for human error and subjectivity and so reduces the reliability of results. Moreover, a large range of contamination is covered by the contamination index (0-4.2 µg mm^{-2} and above) but with low resolution. Therefore, the accuracy of the results is reduced.

'ProReveal Sensitive In-Situ Fluorescence Protein Detection Test'

A group led by Prof. David Perrett from Queen Mary University initially carried out studies on the effectiveness of instrument decontamination using *ex situ* protein analysis[23,24]. Selected areas of cleaned instruments (e.g. the working end of each instrument) were visually inspected and graded based on a contamination index ranging from 0-3 (0 no visible debris, 3 extensive visible debris). Subsequently, instruments were soaked in detergent with sonication and the wash liquids assayed

by staining with o-phthaldialdehyde/N-acetyl cysteine (OPA/NAC) followed by fluorescence analysis[23]. Results ranged from 0.3 µg to 3.85mg of protein per instrument for a selection of dental instruments[24] and 0.5 µg to 63.2 µg of protein per instrument for a set of dental files[25]. In another study, surgical instruments from various hospitals were analysed. Instrument sets had been routinely washed and sterilised ready for their next use before analysis. This study highlighted the difference in the standard between SSDs with the amount of protein removed per instrument ranging from 2 µg to 2.23 mg and up to 45 mg of residual matter[19]. The next stage in the research has involved the development of a detection system for *in situ* measurement of residual protein based on the use of OPA; this system is now being marketed under the tradename ProReveal[26]. An instrument of interest is placed on a sheet of non-fluorescent paper in the drawer of the ProReveal and sprayed with OPA solution. The instrument is analysed and an image of the instrument with an overlay of the fluorescence from protein-bound OPA is displayed. Furthermore, ProReveal software determines the amount of protein based on OPA fluorescence intensity and gives a pass or fail verdict based on a threshold set by the user. This is a novel and swift method of protein detection and is already tailored for use in a clinical setting, though improvements could be made. Although the use of OPA spray reduces the amount of reagent used; the small volumes may not be enough to penetrate thick deposits of proteinaceous material. This could result in an underestimate of protein contamination and a subsequent 'pass' for an instrument which may not be up to standards. Moreover, the safety data sheet for OPA states the users should 'avoid breathing vapours, mist or gas'[27].

The above mentioned techniques have successfully corroborated the fluorescence detection of proteinaceous contamination on surgical instruments; however, each has its shortcomings. A drawback which applies to all three techniques is the need to label samples before analysis. Labelling is time consuming and messy so is not an ideal step in a clinical quality control process. Ideally, analysis of protein contamination would be a label-free process; however, there are drawbacks to this. Spectral complexity and low fluorescence intensities from nanograms of residual protein would presumably plague such measurements but, perhaps a multi-parameter intrinsic fluorescence technique could prove successful.

3.2. Materials and Methods

3.2.1. Materials and sample preparation

Fluorescein isthiocyanate (FITC), Bovine serum albumin (BSA) (≥98%) and FITC-labelled BSA (FITC-BSA) were obtained from Sigma-Aldrich and used as received. A stock solution of FITC-BSA dissolved in distilled water at a concentration of 3mg/ml was frozen in aliquots of 2ml for future use.

For epifluorescence analysis of instruments, 10 mg of FITC was dissolved in 100 ml of carbonate buffer (0.84 g sodium hydrogen carbonate and 1 x sodium hydroxide pellet per 100 ml of buffer) at pH9 and instruments were soaked with light orbital shaking for 10 minutes at room temperature. The instruments were rinsed with water and left to dry before analysis. The labelling conditions are in keeping with those used in solution phase labelling of proteins with FITC[28], however, labelling time was reduced and labelling temperature increased.

3.2.2. Calibration

Stainless steel disks with a diameter of 5 mm were cut from 316L stainless steel sheets using a punch press provided by the UoE mechanical workshop. All tokens were washed in acetone, with vigorous orbital shaking for 15 minutes, rinsed with distilled water and left to dry before use. For epifluorescence analysis, tokens were

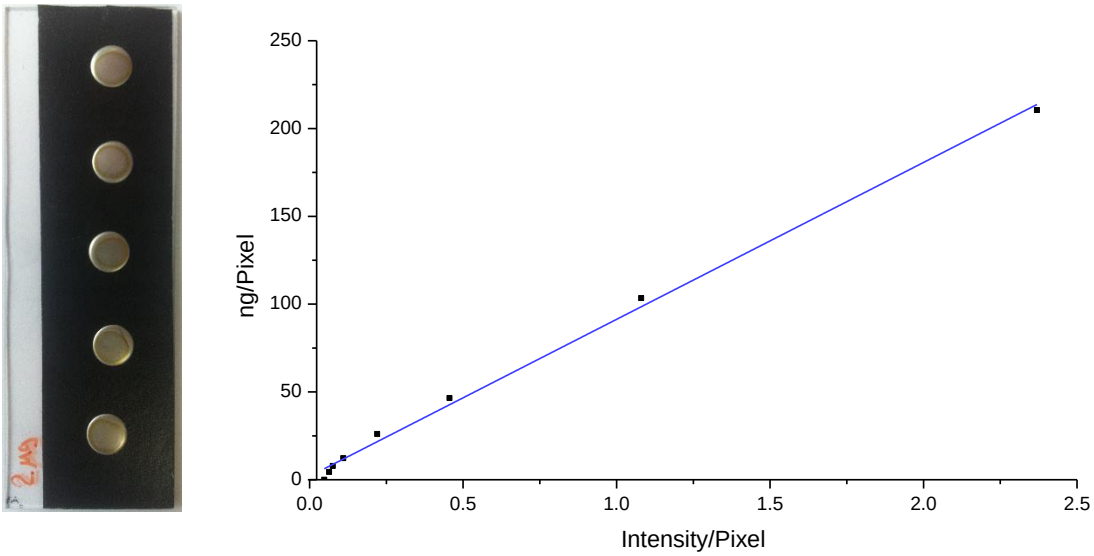

Figure 3.2a. Example set of calibration discs (left) and the calibration plot used for the disposable instruments study (right)

mounted onto double sided, non-fluorescent tape adhered to a glass slide and 20 µL of FITC-BSA solution at varying concentrations (0 – 2 µg per 20 µL) was pipetted onto the tokens and allowed to dry. Five tokens were used for each concentration to improve accuracy. A set of calibration discs is shown in Figure 3.2a (left). Following analysis using the EFScan, a calibration graph was produced (Figure 3.2a right) and the resulting equation was applied to fluorescence intensity (signal voltage) measured for each instrument to give the amount of protein. The method of data analysis used to obtain the calibration graph will be discussed in more detail in the next section. Furthermore, it should be noted that different calibration equations were used for the 3-centre study and the subsequent study of disposable instruments study as the response of the EFScan system changed following repair of the hardware between the projects. The equations used for the 3-centre study and the disposable instruments study were y = 50.4x - 0.147 and y = 89.0x + 1.98, respectively, where x is the measured intensity per pixel and y is the amount of protein (FITC-BSA equivalent) in ng/pixel.

3.2.3. Data Analysis

Together with the pixel by pixel image, an Excel spreadsheet is also produced by the EFScan software, displaying the numerical information in the pixel by pixel image and allowing processing of the data. Before application of the calibration, a background threshold is set to isolate the emission from the calibration disks or instrument; Figure 3.2b (right) shows typical data, after setting values below the

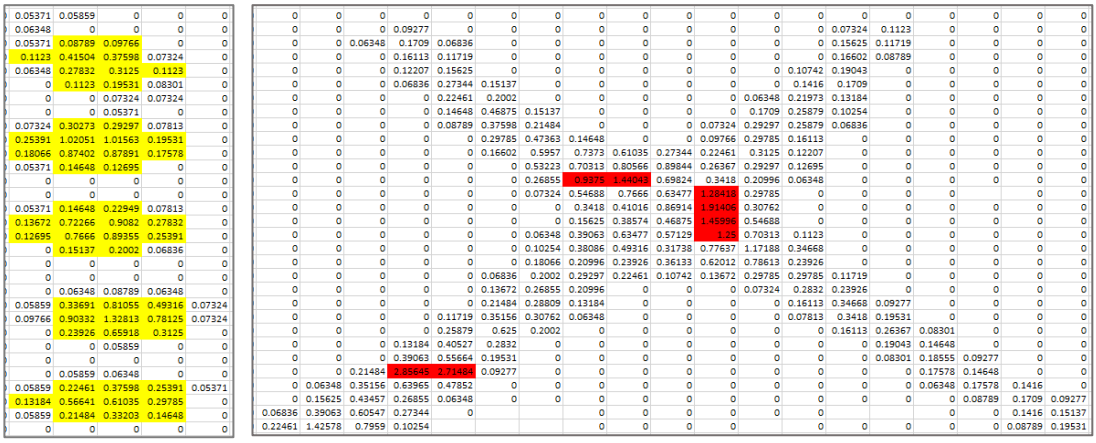

Figure 3.2b. On the left is shown Excel output from EFScan software showing a set of calibration discs (500ng/disc) with pixels above 10% of the peak value highlighted. On the right is shown data measured for the upper tip of instrument B8F from the disposable instruments study with hotspot values highlighted in red

threshold level to zero. For the calibration, the signal obtained from the plate on which instruments were mounted was used as the threshold value to allow for the scattering from blank discs to be observed. After disc areas were identified, the peak value for each disc was determined and all those pixels with values above 10% of the peak were selected and highlighted for analysis (Figure 3.2b left). The mean intensity per pixel was calculated and plotted against the mean protein load per pixel area to produce the calibration plot. Calibration plots could be fitted with a linear equation with R^2 value typically >0.98. The threshold value for the analysis of instruments was determined by evaluating the intensity/pixel from a blank disc and was set to 0.1 before the mid-project repair of the EFScan and 0.06 afterwards. Application of the calibration equation converts the measured fluorescence signal to amounts of protein in ng allowing for calculation of total protein per instrument, protein/mm^2 and the amount of protein in hotspot areas (Figure 3.2b right). The hotspot for each instrument is defined as the pixel containing the highest value. The limit of detection of the EFSCAN system is *ca* 0.15 femtomoles of protein per mm^2, equivalent to 0.1 ng of BSA per mm^2. This exceeds the sensitivity of the commonly used ninhydrin swab test by more than a thousand-fold.

3.2.4. Surgical Instruments

3-Centre Study of Single-use Instruments

The Perrett group (Queen Mary, London) obtained 40 identical, single-use mosquito forceps from Great Ormond Street Hospital, where they had been washed in Prolystica detergent. The instruments had been were procured from Unisurge Ltd. The instruments were randomly allocated to the three groups, 12 to each group, for 'blind' measurement, followed by submission of the results to the Department of Health for analysis. At the time of measurement, all three groups were under the impression that the instruments had been used prior to decontamination at Great Ormond Street Hospital. However, subsequently it became apparent that the instruments were unused. The twelve instruments measured in Edinburgh were labelled S1 to S12.

Farther Study of Single-Use Instruments

Twenty-five single-use (disposable) mosquito forceps were acquired from three different manufacturers; DMI Ltd., Instrapac and Qasco for assessment of pre-

existing surface contamination. Instruments were labelled and analysed straight from the packet and labelled Q1F-Q25F, B1F-B25F and I1F-I25F.

3.2.5. Epifluorescence surface analysis

Epifluorescence surface analysis was carried out using the EFSCAN system. To enable comparison with results from the Perrett group (ProReval system), which employs imaging of one side of the entire instrument with a CCD camera, both the working end (tip) and the handle section of each instrument were measured by carrying out two separate scans. Both sides of each instrument were scanned, making a total of four scans per instrument. The calculated total protein load (over the entire instrument) is slightly overestimated because of overlap between the tip scan and handle scan; about 15% of instrument was scanned twice.

3.2.6. Solid State Measurements

Fluorescence measurements on BSA crystals were carried out by mounting the crystals on double-sided, non-fluorescent, adhesive carbon tape (acquired from Agar scientific) fixed to a glass slide; optical fibres coupled to a fluorescence spectrometer were arranged as shown in Figure 3.2c.

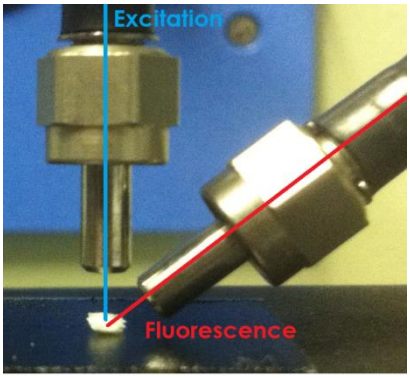

Figure 3.2c. Protein crystal fixed to non-fluorescent tape with optical fibres positioned above

3.3. Results and Discussion

3.3.1. Measurements on Unisurge Single-use Instruments and 3-Centre Study

The following measurements on single-use instruments were undertaken as part of a 3-centre blind study, to cross-validate the three different techniques used by the Edinburgh, Queen Mary and Southampton groups.

EFScan Results

S1				**S1F**			
Area scanned	Total intensity	Intensity /pixel	Intensity/ mm^2	Area scanned	Total intensity	Intensity /pixel	Intensity /mm^2
Upper	10.57	0.12	0.023	Upper	23.96	0.15	0.030
Lower				Lower			
S3				**S3F**			
Area scanned	Total intensity	Intensity /pixel	Intensity/ mm^2	Area scanned	Total intensity	Intensity /pixel	Intensity /mm^2
Upper	3.34	0.12	0.024	Upper	69.42	0.21	0.041
Lower	1.49	0.11	0.023	Lower	51.99	0.2	0.032
S10				**S10F**			
Area scanned	Total intensity	Intensity /pixel	Intensity/ mm^2	Area scanned	Total intensity	Intensity /pixel	Intensity /mm^2
Upper	7.94	0.15	0.030	Upper	43.33	0.18	0.027
Lower	3.43	0.12	0.024	Lower	59.01	0.24	0.044
S11				**S11F**			
Area scanned	Total intensity	Intensity /pixel	Intensity/ mm^2	Area scanned	Total intensity	Intensity /pixel	Intensity /mm^2
Upper	5.53	0.11	0.022	Upper	58.73	0.19	0.032
Lower	11.73	0.11	0.022	Lower	68.72	0.21	0.036
S12				**S12F**			
Area scanned	Total intensity	Intensity /pixel	Intensity/ mm^2	Area scanned	Total intensity	Intensity /pixel	Intensity /mm^2
Upper	8.29	0.12	0.023	Upper	49.1	0.19	0.029
Lower	9.78	0.15	0.029	Lower	37.57	0.16	0.024

Table 3.1. Fluorescence intensity detected on selected instruments analysed before labelling with FITC (designated S1, S3, etc.) and the corresponding intensities following labelling (designated S1F, S3F, etc.)

Before labelling, a sample of the instruments was scanned to determine if there was any background fluorescence from surface contamination. Table 3.1 shows the results obtained, in terms of fluorescence intensity, in comparison with the intensities measured following labelling with FITC. It can be seen that all four instruments sampled show measurable intrinsic fluorescence from surface contamination which must have similar spectral properties to fluorescein. This may be due to flavin adenine dinucleotide (FAD) which absorbs and emits in this wavelength range. However, with the exception of instrument S1, the fluorescence intensity pre-labelling is much less than that post-labelling.

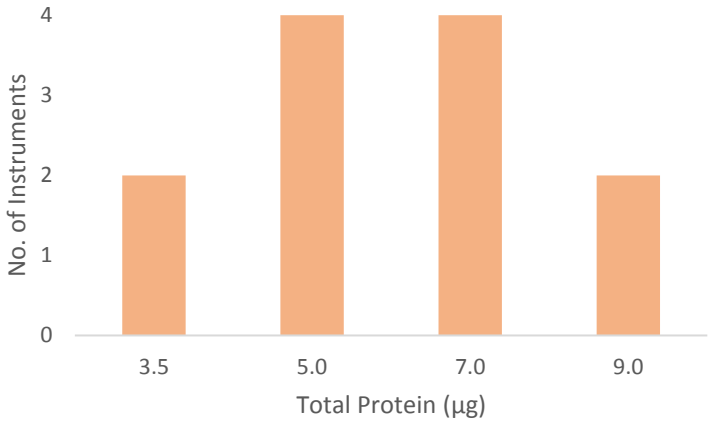

Figure 3.3a. Summary of measurements of total protein load (FITC-BSA equivalent) over the entire instrument. The intervals on the x-axis indicate total protein < 3.5 µg, 3.5-5 µg, ..., 7-9 µg

There is little correlation between the intensity of intrinsic background fluorescence and the corresponding FITC fluorescence which demonstrates the selective binding of FITC as high background fluorescence does not infer high FITC fluorescence and therefore high protein contamination. Table 3.2 (Page 54) gives the results of measurements after FITC labelling for all twelve instruments. The amount of protein load is expressed as total protein load (mass of equivalent number of moles of FITC-BSA) on each side of the instrument (and the sum over both sides) and protein surface density, i.e. the mass (FITC-BSA equivalent) per unit area, averaged over the area in which protein was detected, not the total area of the instrument. The total protein load, measured over the entire instrument (both sides), is summarised graphically in Figure 3.3a and ranges from 3.0 to 8.6 µg. The average load was 5.2 µg (standard deviation 1.8 µg, relative standard deviation 35%). This level of contamination is surprisingly high, given that these are unused instruments, and is comparable to the upper end of the range found for reprocessed instruments in the

previous studies discussed above. Nevertheless, on the basis of these measurements, all of the instruments would satisfy the HTM 01-01 requirement of ≤5 μg (BSA equivalent) of protein per side. The origin of the proteinaceous contamination on these instruments is unknown, but it must be assumed to be deposited during manufacture of the instruments. The variation in level of contamination from instrument to instrument could indicate that contamination occurs through directly handling the instruments during manufacture. The degree of transfer would depend on factors such as local sources of contamination (operative's hands, clothes, working environment), temperature (sweat), and the length of time the instrument was handled.

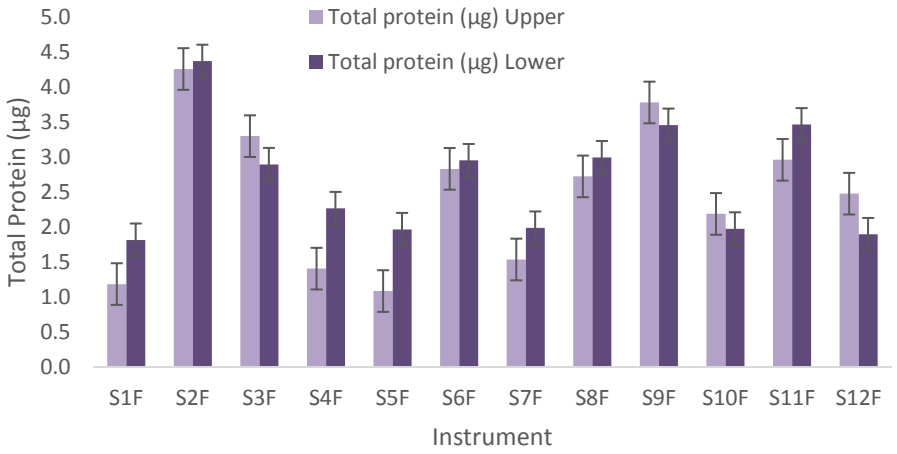

Figure 3.3b. Comparison of the total protein load (FITC-BSA equivalent) on each surface, for each instrument.

Looking at the distribution of contamination on each instrument, as summarised in Figure 3.3b, it can be seen that, in most cases, there is a similar level of contamination on both surfaces. (The two surfaces can be distinguished by manufacturer's marks.) The average load on surface 1 (upper surface) is 2.5 μg (SD 1.0 μg), the average load on surface 2 (lower surface) is 2.7 μg (SD 0.8 μg). Across the set of instruments, total protein on each surface of each instrument is comparatively consistent with a correlation coefficient of 0.87. This suggests that contamination has been transferred via handling during manufacture rather than placement on a contaminated surface. The distribution of protein between the two ends of the instruments, the working end (tip) and handle, is compared in Figure 3.3c. There are generally comparable levels of contamination at each end, although for five of the instruments (5,8,9,10 and 11), there is considerably more contamination present on

the handle than on the tip; the ratio of protein load on the handle to that on the tip was in the range 1.5-2.6 for these five instruments.

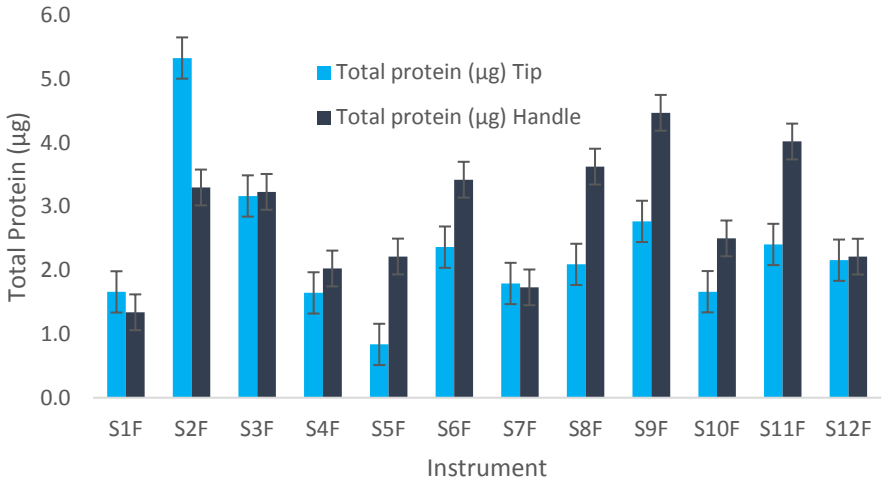

Figure 3.3c. Comparison of the total protein load (FITC-BSA equivalent) on the working end (tip) and the handle, for each instrument

Instrument number 2 shows an unusually high level of protein on the working end; the protein distribution over the entire instrument is shown by the contour plots in

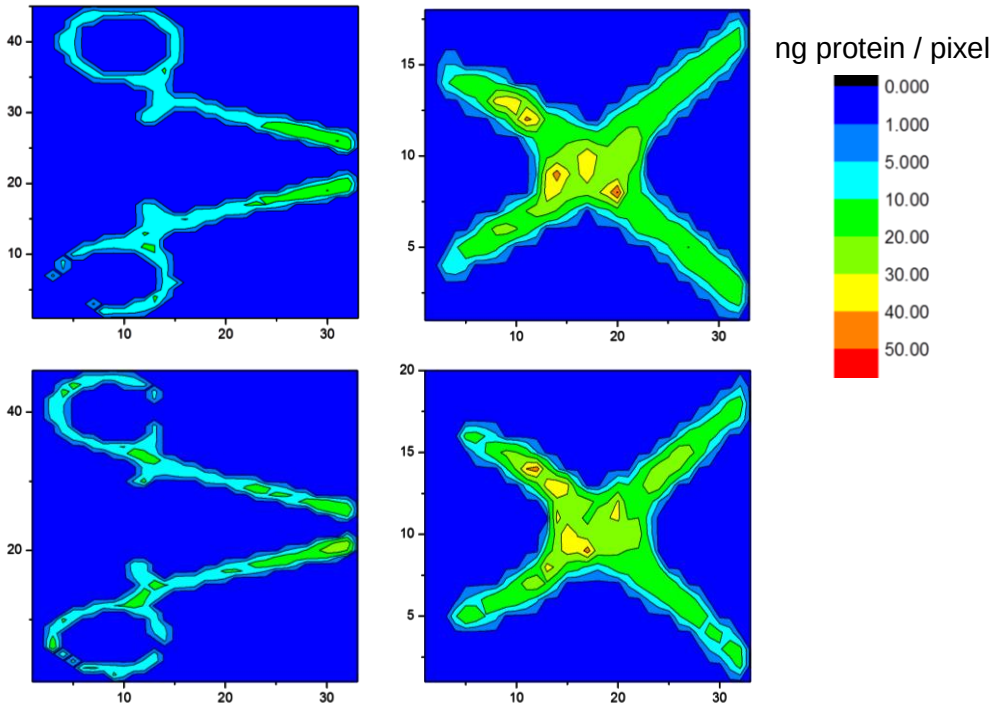

Figure 3.3d. Contour plots of surface protein density, shown as ng per pixel, where 1 pixel is equivalent to 5 mm², for instrument SF2.

Figure 3.3d. There is contamination at a level of 2 to 6 ng mm^{-2} (10-30 ng/pixel) over much of the surface, with several hotspots of about 10 ng mm^{-2} at the working end. There is considerable variation in hotspot values between instruments, showing a RSD of 32%, and, as illustrated in Figure 3.3e, little correlation between hotspot value and total protein contamination. It was observed that hotspots were often located on the joints and tips (working end) of the forceps, and on the thumb and finger rings of the handle. This reinforces the hypothesis that contamination is transferred during manufacture as those areas are handled most frequently.

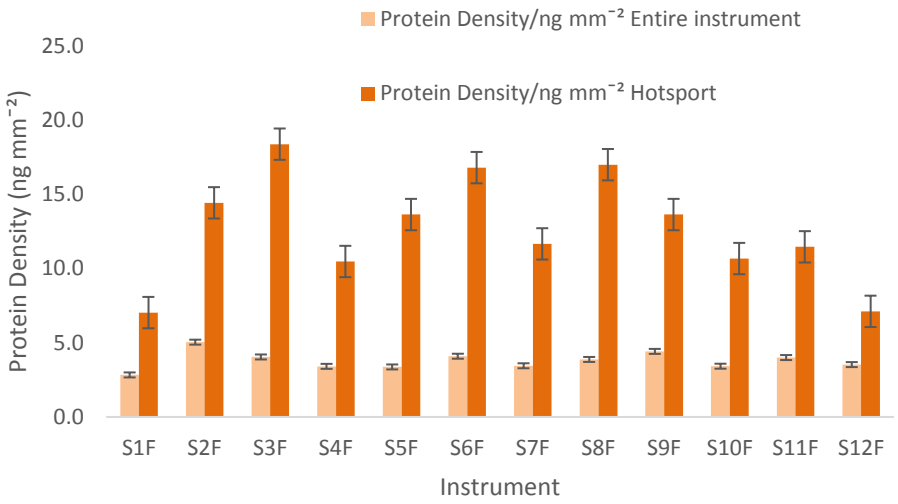

Figure 3.3e. Comparison of average surface density of protein and hotspot density, for each instrument

S1F					**S7F**				
Area Scanned	Total Protein (ng)	ng/ mm^2	HS ng/mm^2	Total µg	Area Scanned	Total Protein (ng)	ng/ mm^2	HS ng/mm^2	Total µg
Upper	1185	2.9	7.0	3.0	Upper	1536	3.3	6.3	3.5
Lower	1815	2.7	5.9		Lower	1987	3.6	11.7	
S2F					**S8F**				
Area Scanned	Total Protein (ng)	ng/ mm^2	HS ng/mm^2	Total µg	Area Scanned	Total Protein (ng)	ng/ mm^2	HS ng/mm^2	Total µg
Upper	4257	5.2	14.4	8.6	Upper	2723	3.8	13.6	5.7
Lower	4369	4.9	14.1		Lower	2993	4.0	17.0	
S3F					**S9F**				
Area Scanned	Total Protein (ng)	ng/ mm^2	HS ng/mm^2	Total µg	Area Scanned	Total Protein (ng)	ng/ mm^2	HS ng/mm^2	Total µg
Upper	3498	4.4	18.4	6.4	Upper	3779	4.5	13.6	7.2
Lower	2895	3.7	15.0		Lower	3456	4.4	12.2	
S4F					**S10F**				
Area Scanned	Total Protein (ng)	ng/ mm^2	HS ng/mm^2	Total µg	Area Scanned	Total Protein (ng)	ng/ mm^2	HS ng/mm^2	Total µg
Upper	1405	3.2	5.7	3.7	Upper	2187	3.6	10.5	4.2
Lower	2266	3.6	10.5		Lower	1975	3.2	10.7	
S5F					**S11F**				
Area Scanned	Total Protein (ng)	ng/ mm^2	HS ng/mm^2	Total µg	Area Scanned	Total Protein (ng)	ng/ mm^2	HS ng/mm^2	Total µg
Upper	1085	3.1	11.3	3.1	Upper	2960	3.8	9.9	6.4
Lower	1966	3.6	13.6		Lower	3463	4.2	11.5	
S6F					**S12F**				
Area Scanned	Total Protein (ng)	ng/ mm^2	HS ng/mm^2	Total µg	Area Scanned	Total Protein (ng)	ng/ mm^2	HS ng/mm^2	Total µg
Upper	2831	4.1	16.0	5.8	Upper	2476	3.8	7.1	4.4
Lower	2951	4.1	16.8		Lower	1894	3.3	5.9	

Table 3.2. The amounts of protein (FITC-BSA equivalent) detected on instruments S1F-S12F, expressed as total protein and surface protein density. The maximum surface protein density, the "hotspot" (HS) is also given.

5.3.2 Comparison of results from the Three Centres

The aim of the 3-centre blind study was to assess the reliability of fluorescence-based techniques for the detection of proteinaceous contamination and the consistency of results obtained using the three different methods. In this section the results obtained by the three groups are compared. The results from each group were submitted independently to the Department of Health for statistical analysis Dr Andre Charlette (Health Protection Agency). The results of that analysis are presented in Table 3.3. It should be noted that the Queen Mary group measured only one side of each instrument, whereas the Edinburgh and Southampton groups measured both sides. The Edinburgh (EFScan) measurements required two separate scans to cover the entire area of the instrument resulting in about 15% overestimate of protein load. The microscope-based system of the Southampton group only allows small areas to be imaged and selective measurements were made on tips, joints and handles.

Group	n	Instrument type	Mean (SD) protein load (µg)	Corr. coeff. (normal distribution)
Queen Mary	16	Mosquito forceps. (one side)	5.1 (2.4)	0.97
Edinburgh	12	Mosquito forceps. (both sides)	5.2 (1.8)	0.94
Edinburgh	12	Mosquito forceps.(one side u)	2.5 (1.1)	0.97
Edinburgh	12	Mosquito forceps. (one side l)	2.7 (0.8)	0.89
Southampton	12	Mosquito forceps. (both sides)	3.5 (0.7)	0.98
Southampton	12	Mosquito forceps. (one side u)	1.5 (0.5)	0.95
Southampton	12	Mosquito forceps. (one side l)	2.0 (0.7)	0.96

Table 3.3. Summary of results from the three groups, showing the number of instruments measured (n), the mean protein load and the correlation with the expectation based on a normal distribution.

As shown in Table 3.3, the mean results from the three groups are of similar magnitude, and all of the results showed a high level of correlation with expectations based on a normal distribution. The Edinburgh values lie between those obtained in Southampton and Queen Mary, with the former being about 1.5 times lower and the latter about 1.5 times higher. In view of the different labelling methods and measurement techniques used in the three groups, the consistency of the measurements is encouraging, and clearly confirm that microgram levels of protein contamination can be found on Unisurge single-use mosquito forceps. Most importantly, these results show the relevance of fluorescence techniques in the identification and quantification of proteinaceous residue on stainless steel surgical instruments.

3.3.3. Further Measurements on Single-use Instruments

Following the success of 3-centre study and the revelation that ready-to-use, single-use instruments have proteinaceous contamination in the region of micrograms after rinsing, it was resolved to look more extensively at the standard of cleanliness of other, single-use instruments. Twenty-five instruments were procured from each of

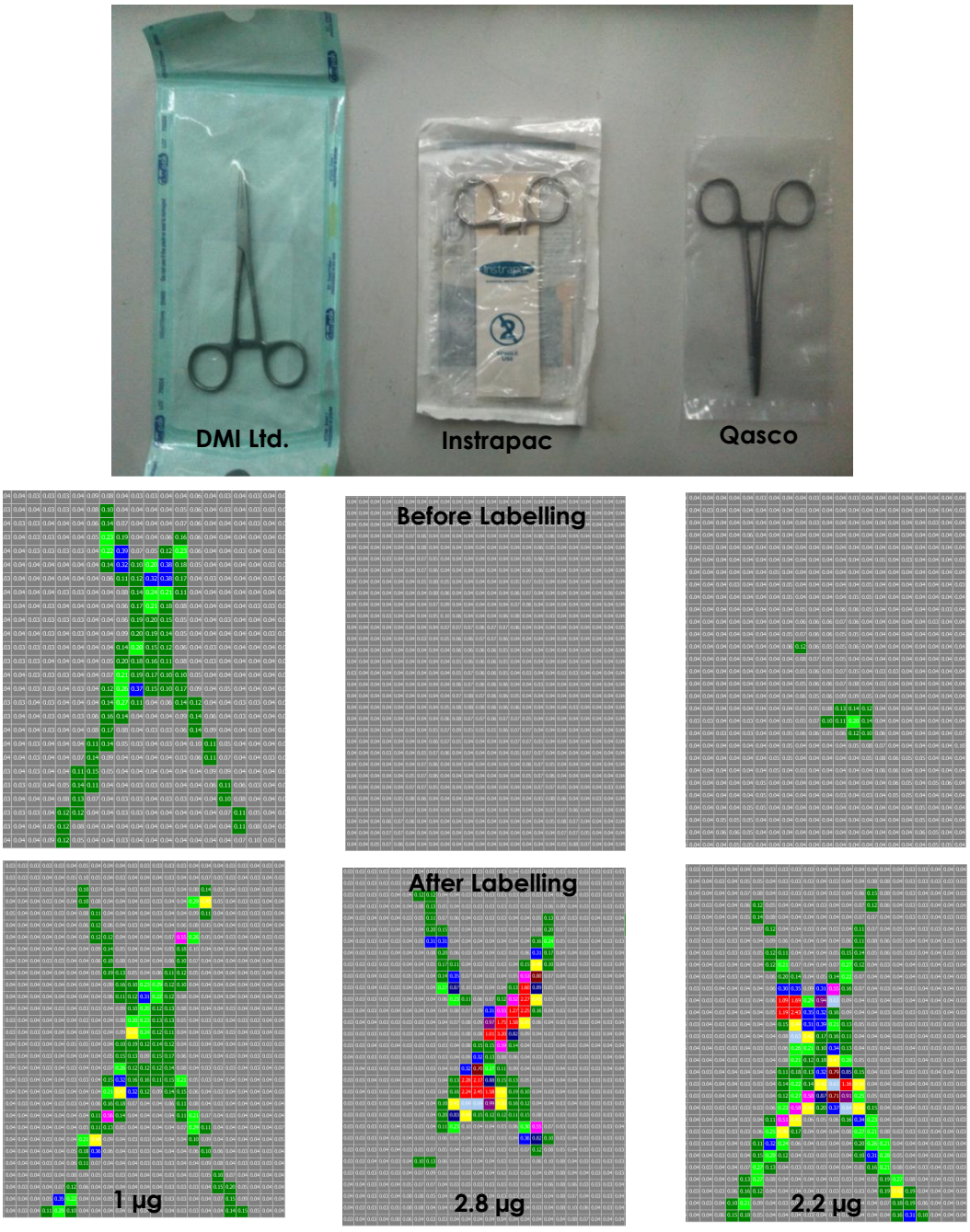

Figure 3.3f. Top - images of instruments in their packaging, as received, Bottom - typical EFScan data for instruments before and after FITC labelling

three manufacturers; Qasco, DMI Ltd. and Instrapac. Initial observations concentrated on the packaging used by each manufacturer. As is shown in Figure 3.3f (top) the packaging for DMI and Instrapac instruments is sealed and are marked as sterile whereas Qasco instruments were supplied in an open ended plastic slip, and, therefore, are not presented as ready-for-use. As exemplified by the EFScan data in Figure 3.3f (middle), some background fluorescence was observed before labelling and there was little correlation between background fluorescence and the corresponding FITC fluorescence (Figure 3.3f bottom), similar to previous findings for the Unisurge instruments. Table 3.4 shows a summary of the mean total amount of contamination detected per instrument, for each set of instruments. The complete results for all instruments are given in Appendix 3.1.

Manufacturer	n	Mean Total Protein (μg)	Mean Total Protein (μ mm^{-2})	%RSD	Correlation Coefficient
Qasco	25	19.4	4.0	28.2	0.9
DMI Ltd.	25	16.5	3.6	33.0	0.3
Instrapac	25	11.4	3.0	33.3	0.3

Table 3.4. Mean total protein levels determined from measurements on single-use instruments from 3 manufacturers; n is the number of instruments measured.

The mean levels of protein contamination were higher, in all cases, than for the Unisurge instruments. This is unsurprising, since the Unisurge instruments had been washed prior to measurement. Total protein contamination was found to decrease in the order Qasco (19.4 μg)> DMI Ltd. (16.5 μg)> Instrapac (11.4 μg). Considering the packaging of Qasco instruments it is unsurprising that they have the largest amount of protein contamination; however, the DMI instruments show only 15% less than the Qasco instruments, whereas Instrapac instruments display over 40% less contamination than Qasco instruments. This suggests that post manufacture processing of Instrapac instruments are of a higher standard than those for DMI Ltd. and, in particular, Qasco instruments. Nonetheless, it is clear that instruments from none of these suppliers can be considered to be clean, although those supplied by DMI and Instrapac may well be sterile. Compared with the results from the pilot study, mean totals for an entire instrument, for each manufacturer are significantly higher. This is to be expected as the instruments used for the pilot study were washed before analysis. Conversely, the average amount of protein per mm^2 for each manufacturer is comparable to the instruments analysed in the pilots study. This can again be explained by the fact that pilot study instruments were washed before analysis. The results presented here for mean protein load per instrument

represents the amount of protein averaged over the area on which protein was detected, not the amount of protein averaged over total area of the instrument. As the pilot study instruments had been washed, there was a smaller area to average over and conversely for the disposable instruments study. Further insight can be gained from the more detailed results in Table 3.5 on the protein load on each side of each instrument. The Qasco instruments show similar levels of contamination on both surfaces, with a correlation coefficient of 0.94. This is in keeping with the

Instrument	Amount of protein (µg)					
	Qasco		DMI Ltd.		Instrapac	
	Upper	Lower	Upper	Lower	Upper	Lower
1	7.5	7.0	5.4	5.7	3.1	3.2
2	5.5	7.8	5.9	5.5	2.7	7.3
3	6.9	7.6	5.2	5.7	3.9	4.5
4	7.8	10.0	6.0	5.0	4.4	5.3
5	10.3	13.4	8.0	6.9	5.7	6.1
6	12.0	11.3	6.5	5.9	6.7	8.6
7	9.1	9.5	8.2	12.0	6.9	11.4
8	9.7	9.4	10.0	15.8	11.6	4.9
9	9.6	9.9	9.0	8.8	4.0	5.9
10	9.6	10.8	18.4	8.3	12.0	5.6
11	11.2	11.0	7.2	17.4	10.1	5.2
12	10.6	10.0	10.2	7.5	7.4	6.7
13	8.1	8.4	7.9	9.7	4.3	4.1
14	6.8	7.0	8.3	10.1	3.7	4.1
15	7.9	8.1	7.7	6.5	4.7	9.9
16	16.1	19.1	8.6	9.3	4.9	6.0
17	12.9	16.1	6.9	8.3	7.9	9.5
18	9.2	9.6	8.1	19.6	6.9	6.7
19	13.0	16.3	9.9	12.2	4.3	3.8
20	13.0	9.6	8.5	9.3	4.5	4.0
21	8.0	7.0	4.8	4.6	3.3	3.3
22	7.8	8.1	5.0	5.9	3.9	4.4
23	6.8	7.5	5.4	5.2	3.7	2.4
24	7.7	7.6	7.3	7.1	5.0	5.3
25	7.9	8.0	6.9	6.1	5.9	5.3

Table 3.5. Amount of protein per side of each of 75 single-use instruments from three manufactures (25 instruments from each). Highlighting indicates those instruments that would have satisfied the HTM 01-01 criterion of ≤5 µg (BSA equivalent) of protein per side

observation for Unisurge instruments, again suggesting that contamination is transferred through indiscriminate handling during manufacture. Instrapac instruments, however, show a low correlation coefficient of 0.28, suggesting that the lower level of contamination on these instruments may have been acquired via contact with a contaminated surface following assembly. The DMI instruments also show a low correlation coefficient of 0.31, although they have high protein contamination, suggesting that contamination has been transferred via handling and contact with contaminated surfaces. Considering these results in the context of the new HTM 01-01 guidelines, remarkably, only 10 instruments (13%) out of all those analysed have protein levels below the 5 μg limit. Of these, none were from Qasco and only one was from DMI Ltd. Despite the fact that Instrapac instruments are significantly cleaner than those from Qasco and DMI, only 36% of the instruments analysed would have passed inspection. The introduction of a threshold value for the amount of protein per side of an instrument is a vital step forward in the improvement of quality control in SSDs; however, the question is raised as to whether an average value per side of an instruments is the most appropriate representation of the contamination.

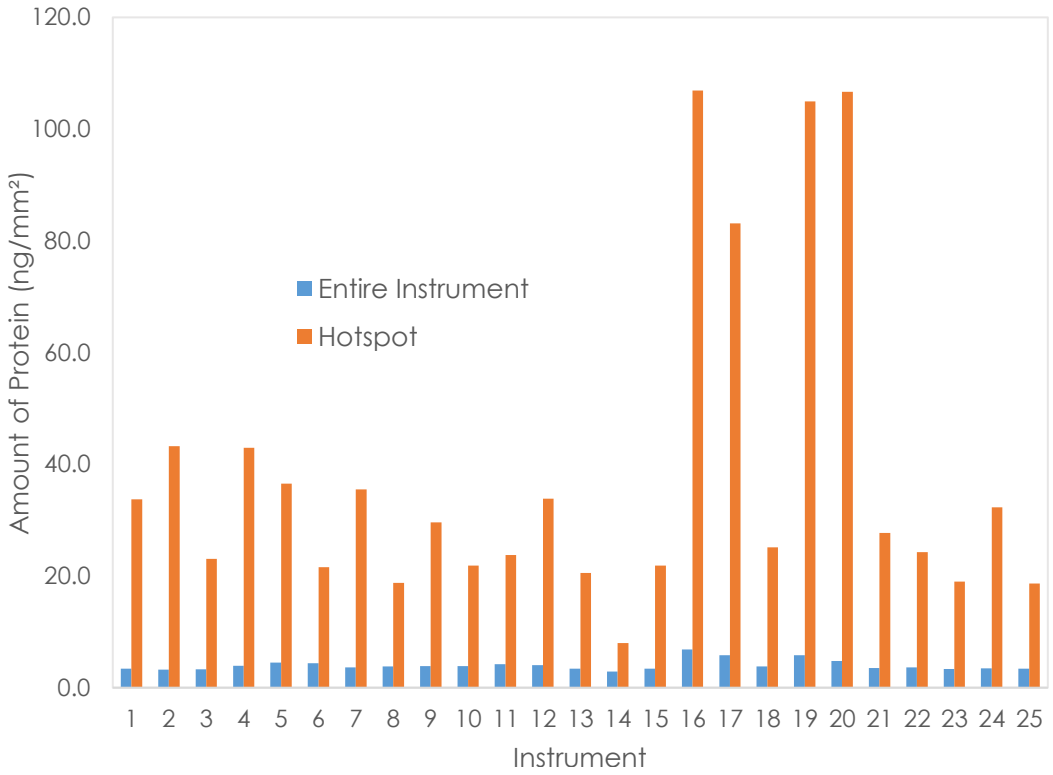

Figure 3.3g. Comparison of average surface protein density for the whole instrument and the corresponding hotspot surface density, for all Qasco instruments

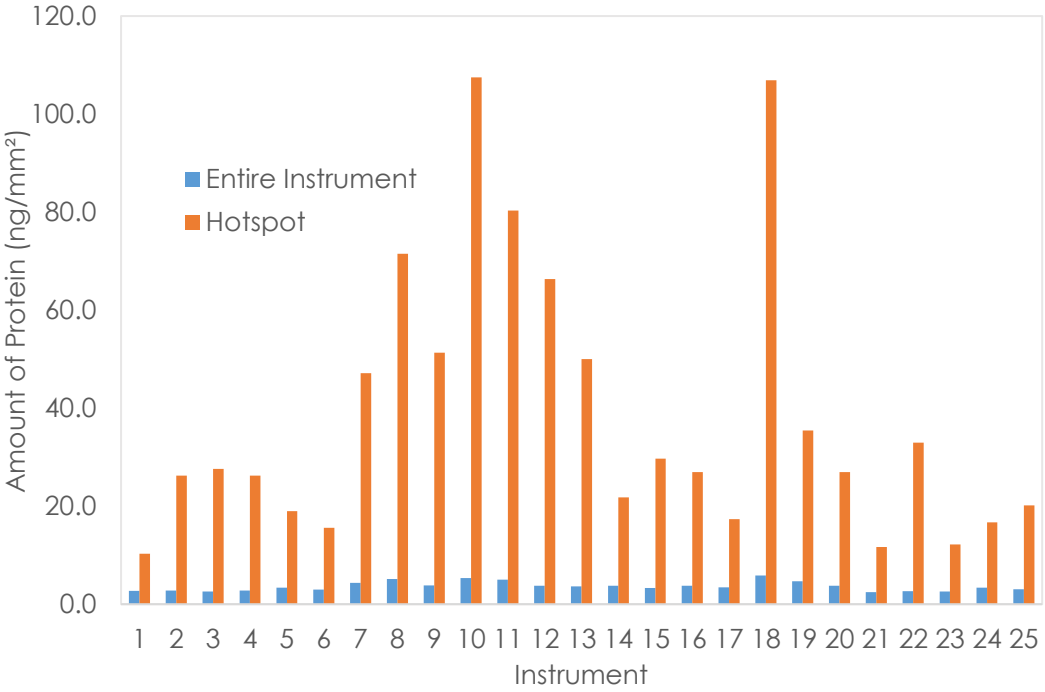

Figure 3.3h. Comparison of average surface protein density for the whole instrument and the corresponding hotspot surface density, for all DMI instruments.

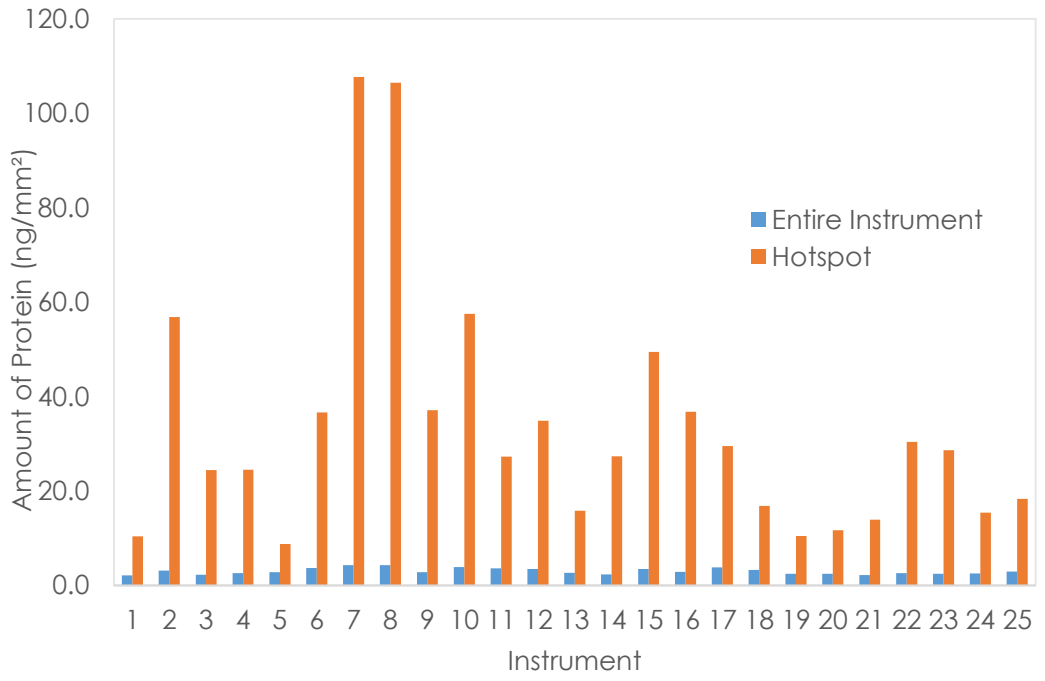

Figure 3.3i. Comparison of average surface protein density for the whole instrument and the corresponding hotspot surface density, for all Instrapac instruments

Figures 3.3g to 3.3i show the comparisons of average surface protein density for an entire instrument with the corresponding hotspot density, for each set of instruments. Evidently, hotspot values are significantly higher than those averaged over the entire instrument with hotspots averaging ten times more contamination for all sets of instruments. It should be noted that maximum hotspot values of around 100 ng/mm^2 for each set of instruments correspond to the saturation of the detector, therefore, even higher levels of contamination could be present. Figure 3.3j shows the distribution of protein between the working end and the handle for instrument Q23F. As was observed for Unisurge instruments, protein distribution is relatively uniform save for hotspots. For Qasco and Instrapac instruments hotspots were relatively evenly distributed between the thumb and finger rings of the handle and the tip whereas hotspots on DMI instruments were mainly found on the thumb and finger rings of the handle (See Appendix 2). As the tip of the forceps require through machining the handle will be touched more frequently and for prolonged periods. The fact that DMI instruments have more hotspot contamination on the handles suggests that the temperature of manufacturing conditions may contribute. The warmer the conditions of manufacture the more likely sweat will contribute to the transfer of

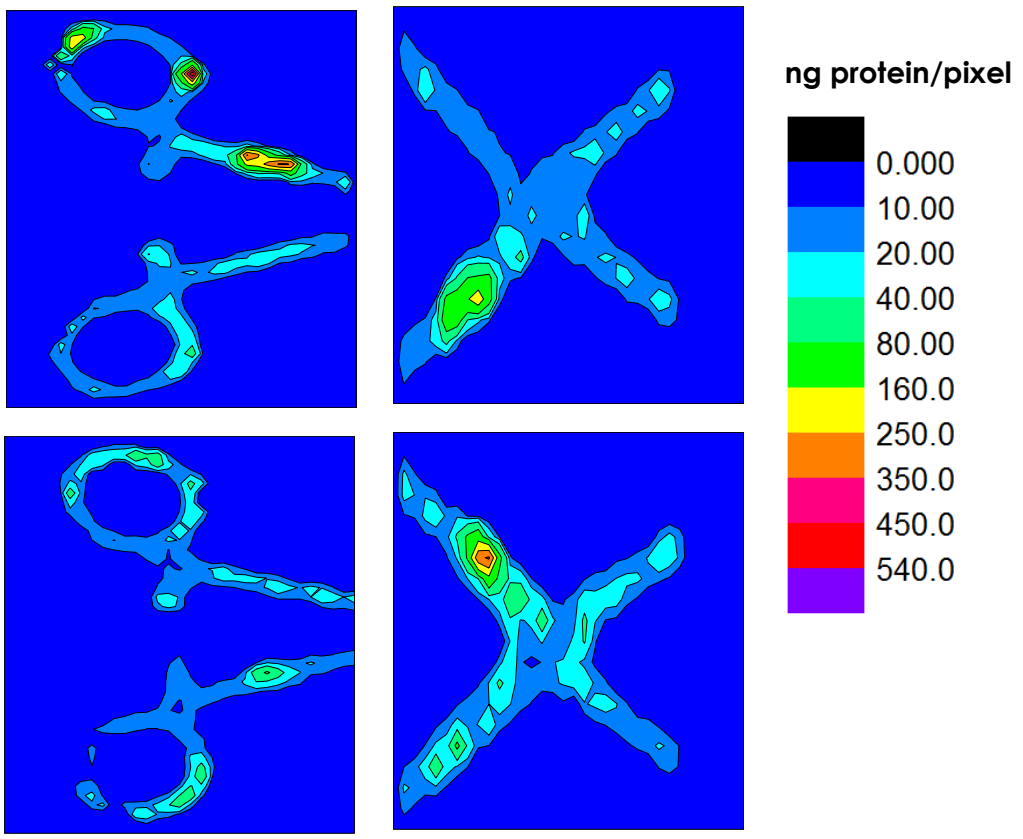

Figure 3.3j. Contour plots of surface protein density, shown as ng per pixel, where 1 pixel is equivalent to 5 mm^2, for instrument Q20F

contamination and therefore, hotspots. Hotspots represent areas of high protein concentration meaning a larger number of, possibly infectious, protein molecules and a thicker plaque. Contact with hotspot areas during surgery may be more likely to result in the transfer of proteinaceous material due to breaking away of upper layers of protein that are not directly bound to the surface of the instrument. Therefore, the inclusion of an additional threshold based on hotspot values may be advisable for quality control.

3.3.4. Development of EFSCAN Labelling Procedure

Given the introduction of a threshold for protein contamination in the HTM guidelines, devices capable of detecting and quantifying protein are now a necessity in SSDs. Commercial development of the EFScan system for use in a clinical setting requires not only refinement of the hardware, but also simplification of the labelling procedure. It was therefore decided to produce a labelling formulation in the form of a tablet, composed of FITC and the constituents of the buffer solution. Each tablet contained 10mg of FITC, 0.2g of sodium hydroxide powder and 0.8g of sodium hydrogen carbonate powder. The constituents were combined in a pestle and mortar and loaded into a pellet press. Resultant tablets had a diameter of 13 mm and were 3 mm thick. They dissolved in 100ml distilled water after 2 minutes of gentle shaking. Resulting solutions gave comparable pH, fluorescence intensities and identical spectral shapes to those made according to the labelling procedure in Section 3.2. Tablet integrity has not been compromised by short term storage in plastic centrifuge tubes, however further research is required to determine the overall lifetime of the tablets. Although the use of tablets makes labelling more straightforward, the labelling step is time-consuming and cumbersome, therefore, a label-free method of detection would be desirable. To determine the feasibility of label-free, intrinsic detection of protein residues, a thorough understanding of protein fluorescence in the solid state is essential.

3.3.5. Preliminary Investigation of Intrinsic Fluorescence of Solid-state BSA

Preliminary experiments to explore the feasibility of label-free detection focussed on BSA crystals, since BSA has been adopted as the standard for label-based detection. As explained in Chapter 1, protein fluorescence is dominated by emission from

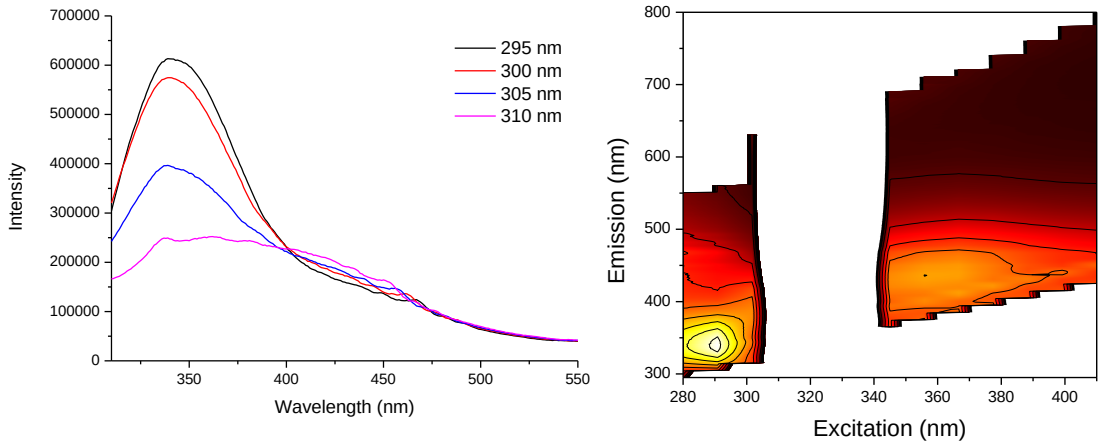

Figure 3.3k. Left - emission as a function of excitation wavelength for a BSA crystal Right - EEM of protein crystal (NB: Central spectra omitted for clarity)

tryptophan (Trp) and this characteristic emission was observed upon exciting BSA crystals at the absorption maximum for Trp (290 nm), however, as excitation wavelengths were increased a marked change in emission intensity and spectral position was observed. Figure 3.3k (left) shows the emission characteristics of a BSA crystal as a function of excitation wavelength, with the spectral position red shifting and spectral shape broadening with increasing excitation wavelength. Such excitation-dependence suggests that there is more than one ground state species present within the BSA crystal. As shown in Figure 3.3k (right), acquisition of an excitation-emission matrix (EEM) at excitation wavelengths ranging from 280 to 410nm clearly shows two distinct peaks, one at 340 nm (λ_{ex} = 290 nm) corresponding to Trp emission and one at 420 nm (λ_{ex} = 360 nm) corresponding to an unknown species. Furthermore, it became apparent that the presence of this species was associated with UV-irradiation of BSA, it was not an extraneous impurity. The encounter of such complexity in the fluorescence properties of BSA in the early stages of characterisation suggested that intrinsic-fluorescence-based protein detection may be problematic, and further experiments to investigate the nature and origin of the long-wavelength emitting species were undertaken, as presented in Chapter 4.

3.4. Conclusions

The EFSCAN system has been successfully utilised in the detection of ng mm^{-2} amounts of protein contamination on pre-washed, single-use mosquito clamps from Unisurge with an average value of 5.2 µg of protein per instrument for the 12 instruments analysed in the pilot study. These results were in close agreement with

those measured at Queen Mary University, London, and the University of Southampton in a 3-centre blind study. The consistency of the results between the three centres successfully demonstrated the effectiveness of fluorescence analysis in the quantitative detection of protein on surgical instruments. Of the three methods tested the author believes that the EFScan system shows the most promise as a commercial product. Although results are comparable, the Southampton method involves sampling of specific areas rather than an entire instrument, using a subjective system which ultimately leads to an underestimation of protein load with reduced repeatability. In terms of the ProReveal the stability of the OPA-protein complex has been called into question, suggesting that results may be flawed from the point of calibration. Despite small discrepancies this study, among others, has informed the revision of Department of Health guidelines for the decontamination of surgical instruments via the inclusion in the recently updated HTM 01-01 of a quantitative target of 5 µg (BSA equivalent) of protein per side of an instrument following washing. In keeping with the type of instrument analysed in the pilot study, a study into the cleanliness of single-use instruments straight from the packet from other manufacturers was carried out. The results showed that of the manufacturers surveyed, protein contamination decreased in the order Qasco > DMI > Instrapac with the average amount of protein per instrument for each manufacturer at 19.4, 16.5 and 11.4 µg respectively, indicating that ready-for-use, single use instruments are contaminated with protein levels comparable to that of reprocessed, re-useable instruments. This reveals the marked variation in standards between manufacturers and, combined with insight into manufacturing processes and standards, gives insight into the manner of protein transfer. As protective wear such as gloves and masks can be rare in some surgical instrument factories, biological contamination can be easily transferred from bare hands, drips of sweat, a sneeze, etc. For those instruments analysed from Qasco, DMI and Instrapac only 13% of instruments would have passed inspection under the new HTM 01-01 guidelines. This is compounded by the fact that hotspot values were 10 times higher than the averaged contamination over the surface of the instrument suggesting that an additional, hotspot threshold should be included to further reduce the risk of infection transmission and improve quality control. The addition of a threshold value in the HTM 01-01 necessitates the introduction of protein detection and quantification systems into SSDs, therefore, subsequent research aims to refine and commercialise the EFScan system.

3.5. Future Work

With such large amounts of protein found on ready-to-use single-use instruments it would be interesting to establish the cleanliness of re-useable instruments before their first use, although the standard of manufacture is much higher for re-usable instruments. It would also be pertinent to compare the cleanliness of manufacture between re-useable instrument suppliers to further establish discrepancies in procedures used to produce surgical instruments. Moreover, a comprehensive comparison of instruments obtained from different SSDs would highlight differences in the quality of procedures used to decontaminate re-useable instruments. Current studies have focused on a single instrument type, therefore, it would be pertinent to attempt analysis of a variety of instrument to highlight high and low risk instrument types.

3.6. References

1. I. P. Lipscomb, H. E. Pinchin, R. Collin, K. Harris and C. W. Keevil, *J. Hosp. Infect.*, 2006, **64**, 288–292.

2. N. K. Nayuni, E. Cloutman-Green, M. Hollis, J. Hartley, S. Martin and D. Perrett, *J. Hosp. Infect.*, 2013, **84**, 97–102.

3. HTM 01-01: Management and decontamination of surgical instruments: Part A – Management and provision https://www.gov.uk/government/uploads/system/uploads/attachment_data/file/536144/HTM0101PartA.pdf (accessed August 2016)

4. L. Tickle, 2015, *Why does so much of the NHS's surgical equipment start life in the sweatshops of Pakistan?*, Independent, 19th January http://www.independent.co.uk/life-style/health-and-families/features/why-does-so-much-of-the-nhss-surgical-equipment-start-life-in-the-sweatshops-of-pakistan-9988885.html (Accessed: January 2017)

5. British Medical Asscoation: *Is this Ethical Trade?*, 2016, https://www.bma.org.uk/features/isthisethicaltrade/ (Accessed January 2017)

6. T. Brophy, P. D. Srodon, C. Briggs, P. Barry, J. Steatham and M. J. Birch, *Ann R Coll Surg Engl*, 2006, **88**, 390–393

7. *R. S. Joshi, Nepal. J. Ophthalmol.*, 2016, **8**, 87-90

8. T. Leslie, D. A. Aitken, T. Barrie and C. M. Kirkness, *Eye*, 2003, **17**, 506–512

9. S. Dinakaran and V. V. Kayarkar, *Eye*, 2002, **16**, 281–284.

4. P. R. Richardson, A. C. Jones, R. L. Baxter, H. C. Baxter, A. G. Whittaker and G. A. Campbell, *Proc. SPIE*, 2004, **5502**, 291-294.

5. 1 H. C. Baxter, G. a Campbell, a G. Whittaker, a C. Jones, A. Aitken, a H. Simpson, M. Casey, L. Bountiff, L. Gibbard and R. L. Baxter, *J. Gen. Virol.*, 2005, **86**, 2393–2399.

6. H. C. Baxter, G. a Campbell, P. R. Richardson, a C. Jones, I. R. Whittle, M. Casey, a G. Whittaker and R. L. Baxter, *IEEE Trans. Plasma Sci.*, 2006, **34**, 1337–1344.

7. W. H. Sawyer and N. Klonis, *J. Fluoresc.*, 1996, **6**, 148–157.

8. R. Sjoback, J. Nygren and M. Kubista, *Spectrochim. Acta Part A*, 1995, **51**, L7–L21.

9. J. M. Alvarez-pez, L. Ballesteros, E. Talavera and J. Yguerabide, *J. Phys. Chem. A*, 2001, **105**, 6320–6332.

10. M. Bennet, M., PhD thesis, The University of Edinburgh, 2011

11. H. Maeda, N. Ishida, H. Kawauchijt and K. Tuzimura, *J. Biochem. Biochem.*, 1969, **63**, 777–783.

12. H. C. Baxter, P. R. Richardson, G. a Campbell, V. I. Kovalev, R. Maier, J. S. Barton, A. C. Jones, G. DeLarge, M. Casey and R. L. Baxter, *New J. Phys.*, 2009, **11**, 1–13.

13. I. P. Lipscomb, a K. Sihota, M. Botham, K. L. Harris and C. W. Keevil, *J. Hosp. Infect.*, 2006, **62**, 141–148.

14. I. P. Lipscomb, a K. Sihota and C. W. Keevil, *J. Clin. Microbiol.*, 2006, **44**, 3728–3733.

15. I. P. Lipscomb, a K. Sihota and C. W. Keevil, *J. Hosp. Infect.*, 2008, **68**, 52–58.

16. R. Hervé, T. J. Secker and C. W. Keevil, *J. Hosp. Infect.*, 2010, **75**, 309–313.

17. A. Smith, S. Letters, A. Lange, D. Perrett, S. McHugh and J. Bagg, *J. Hosp. Infect.*, 2005, **61**, 237–241.

18. M. Vassey, C. Budge, T. Poolman, P. Jones, D. Perrett, N. Nayuni, P. Bennett, P. Groves, A. Smith, M. Fulford, P. D. Marsh, J. T. Walker, J. M. Sutton and N. D. H. Raven, *Br. Dent. J.*, 2011, **210**, E14.

19. H. Murdoch, D. Taylor, J. Dickinson, J. T. Walker, D. Perrett, N. D. H. Raven and J. M. Sutton, *J. Hosp. Infect.*, 2006, **63**, 432–438.

20. Synoptic Healthcare, *ProReveal Sensitive In-Situ Fluorescence Protein Detection Test*, 2012, http://www.synopticshealth.com/assets/Articles/06synopticshealth.pdf (Accessed May 2016)

21. Sigma-Aldrich, Materials *Safety Data Sheet: Phthaldialdehyde Reagent (P0532),* Version 5.3, 2016.

28. Sigma Aldrich, Fluorescein Isothiocyanate Product Information Sheet, https://www.sigmaaldrich.com/content/dam/sigma-aldrich/docs/Sigma/Product_Information_Sheet/f7250pis.pdf

Appendix 3.1: Detailed Results from Measurements of Protein Contamination on Single-use Instruments from Three Manufacturers

Table A3a. Results for measurements on single-use instruments obtained from Qasco.

Q1F								
Area Scanned	Total Protein (ng)	ng/ pixel	ng/ mm^2	HS ng/ pixel	HS ng/ mm^2	Total (µg)	Total ng/pixel	Total ng/mm^2
Upper	7016.54	17.03	3.36	102.3	20.2	14.47	17.35	3.43
Lower	7452.60	17.66	3.49	170.8	33.7			
Q2F								
Area Scanned	Total Protein (ng)	ng/ pixel	ng/ mm^2	HS ng/ pixel	HS ng/ mm^2	Total (µg)	Total ng/pixel	Total ng/mm^2
Upper	7750.63	18.28	3.61	218.8	43.2	13.21	16.33	3.23
Lower	5723.20	14.87	2.94	87.1	17.2			
Q3F								
Area Scanned	Total Protein (ng)	ng/ pixel	ng/ mm^2	HS ng/ pixel	HS ng/ mm^2	Total (µg)	Total ng/pixel	Total ng/mm^2
Upper	7638.91	18.59	3.67	113.2	22.4	14.52	16.61	3.28
Lower	7116.14	15.37	3.04	116.7	23.1			
Q4F								
Area Scanned	Total Protein (ng)	ng/ pixel	ng/ mm^2	HS ng/ pixel	HS ng/ mm^2	Total (µg)	Total ng/pixel	Total ng/mm^2
Upper	9951.05	22.46	4.44	217.5	43.0	17.74	19.85	3.92
Lower	7371.59	16.34	3.23	93.6	18.5			
Q5F								
Area Scanned	Total Protein (ng)	ng/ pixel	ng/ mm^2	HS ng/ pixel	HS ng/ mm^2	Total (µg)	Total ng/pixel	Total ng/mm^2
Upper	13372.50	25.62	5.06	184.8	36.5	23.66	22.73	4.49
Lower	10779.88	20.42	4.10	81.8	16.2			
Q6F								
Area Scanned	Total Protein (ng)	ng/ pixel	ng/ mm^2	HS ng/ pixel	HS ng/ mm^2	Total (µg)	Total ng/pixel	Total ng/mm^2
Upper	11284.32	21.70	4.29	101.0	20.0	23.33	22.26	4.40
Lower	11721.45	22.20	4.39	109.3	21.6			
Q7F								
Area Scanned	Total Protein (ng)	ng/ pixel	ng/ mm^2	HS ng/ pixel	HS ng/ mm^2	Total (µg)	Total ng/pixel	Total ng/mm^2
Upper	9545.86	18.79	3.71	179.6	35.5	18.63	18.52	3.66
Lower	9013.09	18.10	3.58	79.2	15.6			
Q8F								

Area Scanned	Total Protein (ng)	ng/ pixel	ng/ mm^2	HS ng/ pixel	HS ng/ mm^2	Total (µg)	Total ng/pixel	Total ng/mm^2
Upper	9410.14	19.01	3.76	85.8	16.9	19.15	19.25	3.80
Lower	9499.42	19.00	3.75	94.9	18.7			
Q9F								
Area Scanned	Total Protein (ng)	ng/ pixel	ng/ mm^2	HS ng/ pixel	HS ng/ mm^2	Total (µg)	Total ng/pixel	Total ng/mm^2
Upper	9913.91	18.60	3.67	149.9	29.6	19.49	19.65	3.88
Lower	10344.08	22.54	4.45	145.1	28.7			
Q10F								
Area Scanned	Total Protein (ng)	ng/ pixel	ng/ mm^2	HS ng/ pixel	HS ng/ mm^2	Total (µg)	Total ng/pixel	Total ng/mm^2
Upper	10785.42	20.70	4.09	520.0	102.7	20.37	19.57	3.87
Lower	9798.32	18.84	3.72	104.5	20.6			
Q11F								
Area Scanned	Total Protein (ng)	ng/ pixel	ng/ mm^2	HS ng/ pixel	HS ng/ mm^2	Total (µg)	Total ng/pixel	Total ng/mm^2
Upper	10970.62	21.10	4.17	114.1	22.5	22.13	21.21	4.19
Lower	9849.89	18.83	3.72	120.2	23.7			
Q12F								
Area Scanned	Total Protein (ng)	ng/ pixel	ng/ mm^2	HS ng/ pixel	HS ng/ mm^2	Total (µg)	Total ng/pixel	Total ng/mm^2
Upper	10000.20	19.38	3.83	171.3	33.8	20.64	20.27	4.00
Lower	8916.59	17.76	3.51	108.9	21.5			
Q13F								
Area Scanned	Total Protein (ng)	ng/ pixel	ng/ mm^2	HS ng/ pixel	HS ng/ mm^2	Total (µg)	Total ng/pixel	Total ng/mm^2
Upper	8401.4	17.4	3.4	73.1	14.4	16.5	17.1	3.4
Lower	7993.4	16.5	3.3	104.1	20.6			
Q14F								
Area Scanned	Total Protein (ng)	ng/ pixel	ng/ mm^2	HS ng/ pixel	HS ng/ mm^2	Total (µg)	Total ng/pixel	Total ng/mm^2
Upper	6962.7	14.8	2.9	52.2	10.3	13.8	14.6	2.9
Lower	7157.9	15.2	3.0	40.4	8.0			
Q15F								
Area Scanned	Total Protein (ng)	ng/ pixel	ng/ mm^2	HS ng/ pixel	HS ng/ mm^2	Total (µg)	Total ng/pixel	Total ng/mm^2
Upper	8124.0	17.6	3.5	110.6	21.9	16.0	17.2	3.4
Lower	7970.8	17.0	3.3	75.3	14.9			
Q16F								
Area Scanned	Total Protein (ng)	ng/ pixel	ng/ mm^2	HS ng/ pixel	HS ng/ mm^2	Total (µg)	Total ng/pixel	Total ng/mm^2
Upper	19052.6	37.1	7.3	536.5	106.0	35.1	34.6	6.8
Lower	14802.9	29.5	5.8	541.3	106.9			
Q17F								

Area Scanned	Total Protein (ng)	ng/ pixel	ng/ mm^2	HS ng/ pixel	HS ng/ mm^2	Total (µg)	Total ng/pixel	Total ng/mm^2
Upper	16073.2	31.7	6.3	358.0	70.7	29.0	29.4	5.8
Lower	13481.1	28.1	5.5	420.8	83.1			
Q18F								
Area Scanned	Total Protein (ng)	ng/ pixel	ng/ mm^2	HS ng/ pixel	HS ng/ mm^2	Total (µg)	Total ng/pixel	Total ng/mm^2
Upper	9571.4	19.4	3.8	127.2	25.1	18.8	19.1	3.8
Lower	9730.2	19.9	3.9	106.3	21.0			
Q19F								
Area Scanned	Total Protein (ng)	ng/ pixel	ng/ mm^2	HS ng/ pixel	HS ng/ mm^2	Total (µg)	Total ng/pixel	Total ng/mm^2
Upper	16291.3	32.3	6.4	531.2	104.9	29.3	29.4	5.8
Lower	14336.8	29.1	5.7	527.7	104.2			
Q20F								
Area Scanned	Total Protein (ng)	ng/ pixel	ng/ mm^2	HS ng/ pixel	HS ng/ mm^2	Total (µg)	Total ng/pixel	Total ng/mm^2
Upper	9583.9	21.2	4.2	367.2	72.5	22.6	24.2	4.8
Lower	8706.3	18.2	3.6	539.9	106.7			
Q21F								
Area Scanned	Total Protein (ng)	ng/ pixel	ng/ mm^2	HS ng/ pixel	HS ng/ mm^2	Total (µg)	Total ng/pixel	Total ng/mm^2
Upper	7031.6	17.5	3.5	140.3	27.7	15.1	17.9	3.5
Lower	7342.7	16.7	3.3	130.7	25.8			
Q22F								
Area Scanned	Total Protein (ng)	ng/ pixel	ng/ mm^2	HS ng/ pixel	HS ng/ mm^2	Total (µg)	Total ng/pixel	Total ng/mm^2
Upper	7511.5	19.0	3.8	110.2	21.8	15.9	18.3	3.6
Lower	7427.7	16.8	3.3	122.8	24.3			
Q23F								
Area Scanned	Total Protein (ng)	ng/ pixel	ng/ mm^2	HS ng/ pixel	HS ng/ mm^2	Total (µg)	Total ng/pixel	Total ng/mm^2
Upper	7511.5	17.7	3.5	91.0	18.0	14.4	16.8	3.3
Lower	6083.3	14.1	2.8	96.2	19.0			
Q24F								
Area Scanned	Total Protein (ng)	ng/ pixel	ng/ mm^2	HS ng/ pixel	HS ng/ mm^2	Total (µg)	Total ng/pixel	Total ng/mm^2
Upper	7616.3	17.4	3.4	163.4	32.3	15.4	17.5	3.5
Lower	6982.3	15.8	3.1	118.0	23.3			
Q25F								
Area Scanned	Total Protein (ng)	ng/ pixel	ng/ mm^2	HS ng/ pixel	HS ng/ mm^2	Total (µg)	Total ng/pixel	Total ng/mm^2
Upper	7985.9	17.4	3.4	94.5	18.7	15.9	17.2	3.4
Lower	8077.2	17.4	3.4	56.5	11.2			

Table A3b. Results for measurements on single-use instruments obtained from DMI Ltd

B1F								
Area Scanned	Total Protein (ng)	ng/ pixel	ng/ mm^2	HS ng/ pixel	HS ng/ mm^2	Total (µg)	Total ng/pixel	Total ng/mm^2
Upper	5664.8	14.0	2.8	52.2	10.3	11.1	13.7	2.7
Lower	5426.5	13.4	2.6	46.9	9.3			
B2F								
Area Scanned	Total Protein (ng)	ng/ pixel	ng/ mm^2	HS ng/ pixel	HS ng/ mm^2	Total (µg)	Total ng/pixel	Total ng/mm^2
Upper	5526.2	13.7	2.7	45.2	8.9	11.4	14.0	2.8
Lower	5883.0	14.3	2.8	132.9	26.2			
B3F								
Area Scanned	Total Protein (ng)	ng/ pixel	ng/ mm^2	HS ng/ pixel	HS ng/ mm^2	Total (µg)	Total ng/pixel	Total ng/mm^2
Upper	5719.0	13.5	2.7	139.9	27.6	10.9	13.2	2.6
Lower	5204.7	12.9	2.5	44.7	8.8			
B4F								
Area Scanned	Total Protein (ng)	ng/ pixel	ng/ mm^2	HS ng/ pixel	HS ng/ mm^2	Total (µg)	Total ng/pixel	Total ng/mm^2
Upper	5025.3	12.8	2.5	53.9	10.6	11.0	13.9	2.8
Lower	6002.5	15.1	3.0	132.9	26.2			
B5F								
Area Scanned	Total Protein (ng)	ng/ pixel	ng/ mm^2	HS ng/ pixel	HS ng/ mm^2	Total (µg)	Total ng/pixel	Total ng/mm^2
Upper	6885.3	15.7	3.1	66.6	13.1	14.9	17.0	3.3
Lower	8049.2	19.5	3.6	96.2	19.0			
B6F								
Area Scanned	Total Protein (ng)	ng/ pixel	ng/ mm^2	HS ng/ pixel	HS ng/ mm^2	Total (µg)	Total ng/pixel	Total ng/mm^2
Upper	5942.9	14.7	2.9	48.7	9.6	12.4	15.2	3.0
Lower	6504.1	15.7	3.1	78.8	15.6			
B7F								
Area Scanned	Total Protein (ng)	ng/ pixel	ng/ mm^2	HS ng/ pixel	HS ng/ mm^2	Total (µg)	Total ng/pixel	Total ng/mm^2
Upper	11996.8	25.0	4.9	238.5	47.1	20.2	22.1	4.4
Lower	8173.2	18.8	3.7	174.8	34.5			
B8F								
Area Scanned	Total Protein (ng)	ng/ pixel	ng/ mm^2	HS ng/ pixel	HS ng/ mm^2	Total (µg)	Total ng/pixel	Total ng/mm^2
Upper	15827.6	31.5	6.2	361.9	71.5	25.8	26.1	5.2
Lower	9969.7	20.6	4.1	111.5	22.0			
B9F								

Area Scanned	Total Protein (ng)	ng/ pixel	ng/ mm^2	HS ng/ pixel	HS ng/ mm^2	Total (µg)	Total ng/pixel	Total ng/mm^2
Upper	8804.1	19.2	3.8	151.2	29.9	17.8	19.4	3.8
Lower	9016.8	19.6	3.9	259.8	51.3			
B10F								
Area Scanned	Total Protein (ng)	ng/ pixel	ng/ mm^2	HS ng/ pixel	HS ng/ mm^2	Total (µg)	Total ng/pixel	Total ng/mm^2
Upper	8311.8	17.5	3.4	89.2	17.6	26.7	26.9	5.3
Lower	18370.3	35.6	7.0	544.3	107.5			
B11F								
Area Scanned	Total Protein (ng)	ng/ pixel	ng/ mm^2	HS ng/ pixel	HS ng/ mm^2	Total (µg)	Total ng/pixel	Total ng/mm^2
Upper	17423.4	33.9	6.7	406.4	80.3	24.6	25.5	5.0
Lower	7198.6	15.9	3.1	82.7	16.3			
B12F								
Area Scanned	Total Protein (ng)	ng/ pixel	ng/ mm^2	HS ng/ pixel	HS ng/ mm^2	Total (µg)	Total ng/pixel	Total ng/mm^2
Upper	7461.5	16.9	3.3	90.6	17.9	17.6	19.2	3.8
Lower	10151.1	21.3	4.2	335.8	66.3			
B13F								
Area Scanned	Total Protein (ng)	ng/ pixel	ng/ mm^2	HS ng/ pixel	HS ng/ mm^2	Total (µg)	Total ng/pixel	Total ng/mm^2
Upper	9730.8	20.1	4.0	253.3	50.0	17.6	18.5	3.7
Lower	7887.5	16.9	3.3	60.4	11.9			
B14F								
Area Scanned	Total Protein (ng)	ng/ pixel	ng/ mm^2	HS ng/ pixel	HS ng/ mm^2	Total (µg)	Total ng/pixel	Total ng/mm^2
Upper	10063.7	20.8	4.1	110.2	21.8	18.4	19.2	3.8
Lower	8326.7	17.5	3.5	78.8	15.6			
B15F								
Area Scanned	Total Protein (ng)	ng/ pixel	ng/ mm^2	HS ng/ pixel	HS ng/ mm^2	Total (µg)	Total ng/pixel	Total ng/mm^2
Upper	6472.2	15.4	3.1	41.7	8.2	14.1	16.7	3.3
Lower	7655.8	18.0	3.6	150.3	29.7			
B16F								
Area Scanned	Total Protein (ng)	ng/ pixel	ng/ mm^2	HS ng/ pixel	HS ng/ mm^2	Total (µg)	Total ng/pixel	Total ng/mm^2
Upper	9327.0	19.8	3.9	136.4	26.9	17.9	19.1	3.8
Lower	8594.4	18.4	3.6	64.8	12.8			
B17F								
Area Scanned	Total Protein (ng)	ng/ pixel	ng/ mm^2	HS ng/ pixel	HS ng/ mm^2	Total (µg)	Total ng/pixel	Total ng/mm^2
Upper	8304.9	18.1	3.6	62.2	12.3	15.2	17.3	3.4
Lower	6902.9	16.4	3.2	87.9	17.4			
B18F								

Area Scanned	Total Protein (ng)	ng/ pixel	ng/ mm^2	HS ng/ pixel	HS ng/ mm^2	Total (µg)	Total ng/pixel	Total ng/mm^2
Upper	19608.3	38.9	7.7	541.3	106.9	27.7	29.7	5.9
Lower	8058.9	18.9	3.7	159.9	31.6			
B19F								
Area Scanned	Total Protein (ng)	ng/ pixel	ng/ mm^2	HS ng/ pixel	HS ng/ mm^2	Total (µg)	Total ng/pixel	Total ng/mm^2
Upper	12192.4	25.4	5.0	179.6	35.5	22.0	23.6	4.7
Lower	9851.6	21.7	4.3	148.6	29.3			
B20F								
Area Scanned	Total Protein (ng)	ng/ pixel	ng/ mm^2	HS ng/ pixel	HS ng/ mm^2	Total (µg)	Total ng/pixel	Total ng/mm^2
Upper	9264.5	19.9	3.9	136.4	26.9	17.8	19.2	3.8
Lower	8523.6	18.5	3.7	64.8	12.8			
B21F								
Area Scanned	Total Protein (ng)	ng/ pixel	ng/ mm^2	HS ng/ pixel	HS ng/ mm^2	Total (µg)	Total ng/pixel	Total ng/mm^2
Upper	4556.9	12.5	2.5	58.7	11.6	9.4	12.3	2.4
Lower	4801.8	12.2	2.4	59.1	11.7			
B22F								
Area Scanned	Total Protein (ng)	ng/ pixel	ng/ mm^2	HS ng/ pixel	HS ng/ mm^2	Total (µg)	Total ng/pixel	Total ng/mm^2
Upper	5160.6	14.8	2.9	52.6	10.4	10.9	13.6	2.7
Lower	4963.3	12.4	2.4	166.9	33.0			
B23F								
Area Scanned	Total Protein (ng)	ng/ pixel	ng/ mm^2	HS ng/ pixel	HS ng/ mm^2	Total (µg)	Total ng/pixel	Total ng/mm^2
Upper	5160.6	13.5	2.7	61.8	12.2	10.6	13.2	2.6
Lower	5398.8	12.9	2.6	57.8	11.4			
B24F								
Area Scanned	Total Protein (ng)	ng/ pixel	ng/ mm^2	HS ng/ pixel	HS ng/ mm^2	Total (µg)	Total ng/pixel	Total ng/mm^2
Upper	7088.5	17.4	3.4	84.4	16.7	14.4	17.2	3.4
Lower	7270.1	17.1	3.4	77.5	15.3			
B25F								
Area Scanned	Total Protein (ng)	ng/ pixel	ng/ mm^2	HS ng/ pixel	HS ng/ mm^2	Total (µg)	Total ng/pixel	Total ng/mm^2
Upper	6071.3	14.6	2.9	101.9	20.1	13.0	15.5	3.1
Lower	6910.1	16.3	3.2	74.8	14.8			

Table A3c. Results for measurements on single-use instruments obtained from Instrapac.

I1F								
Area Scanned	Total Protein (ng)	ng/ pixel	ng/ mm^2	HS ng/ pixel	HS ng/ mm^2	Total (µg)	Total ng/pixel	Total ng/mm^2
Upper	3203.4	10.5	2.1	36.0	7.1	6.3	10.8	2.1
Lower	3146.0	11.2	2.2	52.6	10.4			
I2F								
Area Scanned	Total Protein (ng)	ng/ pixel	ng/ mm^2	HS ng/ pixel	HS ng/ mm^2	Total (µg)	Total ng/pixel	Total ng/mm^2
Upper	7284.3	21.1	4.2	287.8	56.8	9.9	15.9	3.1
Lower	2651.5	9.5	1.9	17.3	3.4			
I3F								
Area Scanned	Total Protein (ng)	ng/ pixel	ng/ mm^2	HS ng/ pixel	HS ng/ mm^2	Total (µg)	Total ng/pixel	Total ng/mm^2
Upper	4496.0	11.9	2.3	36.5	7.2	8.4	11.6	2.3
Lower	3882.2	11.2	2.2	123.7	24.4			
I4F								
Area Scanned	Total Protein (ng)	ng/ pixel	ng/ mm^2	HS ng/ pixel	HS ng/ mm^2	Total (µg)	Total ng/pixel	Total ng/mm^2
Upper	5332.3	14.0	2.8	124.1	24.5	9.7	13.1	2.6
Lower	4382.6	12.3	2.4	71.8	14.2			
I5F								
Area Scanned	Total Protein (ng)	ng/ pixel	ng/ mm^2	HS ng/ pixel	HS ng/ mm^2	Total (µg)	Total ng/pixel	Total ng/mm^2
Upper	6051.5	14.5	2.9	37.3	7.4	11.7	14.1	2.8
Lower	5662.3	14.7	2.7	44.3	8.8			
I6F								
Area Scanned	Total Protein (ng)	ng/ pixel	ng/ mm^2	HS ng/ pixel	HS ng/ mm^2	Total (µg)	Total ng/pixel	Total ng/mm^2
Upper	8592.8	19.6	3.9	185.7	36.7	15.3	18.6	3.7
Lower	6717.2	17.5	3.5	105.4	20.8			
I7F								
Area Scanned	Total Protein (ng)	ng/ pixel	ng/ mm^2	HS ng/ pixel	HS ng/ mm^2	Total (µg)	Total ng/pixel	Total ng/mm^2
Upper	11389.2	26.8	5.3	545.2	107.7	18.3	21.8	4.3
Lower	6865.8	16.7	3.3	137.2	27.1			
I8F								
Area Scanned	Total Protein (ng)	ng/ pixel	ng/ mm^2	HS ng/ pixel	HS ng/ mm^2	Total (µg)	Total ng/pixel	Total ng/mm^2
Upper	4945.0	13.0	2.6	62.6	12.4	16.5	21.7	4.3
Lower	11567.5	30.4	6.0	539.1	106.5			
I9F								

Area Scanned	Total Protein (ng)	ng/ pixel	ng/ mm^2	HS ng/ pixel	HS ng/ mm^2	Total (µg)	Total ng/pixel	Total ng/mm^2
Upper	5937.8	16.3	3.2	187.8	37.1	10.0	14.2	2.8
Lower	4032.1	12.0	2.4	60.0	11.9			
I10F								
Area Scanned	Total Protein (ng)	ng/ pixel	ng/ mm^2	HS ng/ pixel	HS ng/ mm^2	Total (µg)	Total ng/pixel	Total ng/mm^2
Upper	5582.1	13.6	2.7	42.6	8.4	17.6	19.8	3.9
Lower	12000.3	25.1	5.0	291.3	57.5			
I11F								
Area Scanned	Total Protein (ng)	ng/ pixel	ng/ mm^2	HS ng/ pixel	HS ng/ mm^2	Total (µg)	Total ng/pixel	Total ng/mm^2
Upper	5216.8	13.4	2.7	51.7	10.2	15.4	18.2	3.6
Lower	10148.5	22.3	4.4	137.2	27.1			
I12F								
Area Scanned	Total Protein (ng)	ng/ pixel	ng/ mm^2	HS ng/ pixel	HS ng/ mm^2	Total (µg)	Total ng/pixel	Total ng/mm^2
Upper	6673.7	16.4	3.2	176.5	34.9	14.1	17.5	3.5
Lower	7443.5	18.6	3.7	137.2	27.1			
I13F								
Area Scanned	Total Protein (ng)	ng/ pixel	ng/ mm^2	HS ng/ pixel	HS ng/ mm^2	Total (µg)	Total ng/pixel	Total ng/mm^2
Upper	4059.7	12.8	2.5	80.1	15.8	8.3	13.7	2.7
Lower	4255.4	14.7	2.9	46.9	9.3			
I14F								
Area Scanned	Total Protein (ng)	ng/ pixel	ng/ mm^2	HS ng/ pixel	HS ng/ mm^2	Total (µg)	Total ng/pixel	Total ng/mm^2
Upper	4062.2	12.5	2.5	138.5	27.4	7.8	11.9	2.3
Lower	3738.4	11.2	2.2	30.3	6.0			
I15F								
Area Scanned	Total Protein (ng)	ng/ pixel	ng/ mm^2	HS ng/ pixel	HS ng/ mm^2	Total (µg)	Total ng/pixel	Total ng/mm^2
Upper	9864.4	22.0	4.3	250.2	49.4	14.6	17.6	3.5
Lower	4717.4	12.4	2.4	50.8	10.0			
I16F								
Area Scanned	Total Protein (ng)	ng/ pixel	ng/ mm^2	HS ng/ pixel	HS ng/ mm^2	Total (µg)	Total ng/pixel	Total ng/mm^2
Upper	6032.8	15.7	3.1	186.1	36.8	10.9	14.6	2.9
Lower	4888.8	13.5	2.7	63.9	12.6			
I17F								
Area Scanned	Total Protein (ng)	ng/ pixel	ng/ mm^2	HS ng/ pixel	HS ng/ mm^2	Total (µg)	Total ng/pixel	Total ng/mm^2
Upper	9494.3	20.6	4.1	111.9	22.1	17.4	19.2	3.8
Lower	7902.4	17.7	3.5	149.5	29.5			
I18F								

Area Scanned	Total Protein (ng)	ng/ pixel	ng/ mm^2	HS ng/ pixel	HS ng/ mm^2	Total (µg)	Total ng/pixel	Total ng/mm^2
Upper	6682.4	16.1	3.2	73.1	14.4	13.5	16.5	3.3
Lower	6857.6	16.8	3.3	85.3	16.9			
I19F								
Area Scanned	Total Protein (ng)	ng/ pixel	ng/ mm^2	HS ng/ pixel	HS ng/ mm^2	Total (µg)	Total ng/pixel	Total ng/mm^2
Upper	3790.1	12.2	2.4	52.2	10.3	8.1	12.6	2.5
Lower	4260.2	12.9	2.6	53.0	10.5			
I20F								
Area Scanned	Total Protein (ng)	ng/ pixel	ng/ mm^2	HS ng/ pixel	HS ng/ mm^2	Total (µg)	Total ng/pixel	Total ng/mm^2
Upper	3984.0	12.0	2.4	45.2	8.9	8.5	12.5	2.5
Lower	4516.6	13.0	2.6	59.1	11.7			
I21F								
Area Scanned	Total Protein (ng)	ng/ pixel	ng/ mm^2	HS ng/ pixel	HS ng/ mm^2	Total (µg)	Total ng/pixel	Total ng/mm^2
Upper	3313.0	11.2	2.2	70.5	13.9	6.6	11.0	2.2
Lower	3258.3	10.9	2.1	41.2	8.1			
I22F								
Area Scanned	Total Protein (ng)	ng/ pixel	ng/ mm^2	HS ng/ pixel	HS ng/ mm^2	Total (µg)	Total ng/pixel	Total ng/mm^2
Upper	2367.2	15.0	3.0	153.8	30.4	8.4	13.2	2.6
Lower	3918.9	11.6	2.3	87.5	17.3			
I23F								
Area Scanned	Total Protein (ng)	ng/ pixel	ng/ mm^2	HS ng/ pixel	HS ng/ mm^2	Total (µg)	Total ng/pixel	Total ng/mm^2
Upper	2367.2	10.6	2.1	26.4	5.2	6.1	12.3	2.4
Lower	3749.9	13.8	2.7	145.1	28.7			
I24F								
Area Scanned	Total Protein (ng)	ng/ pixel	ng/ mm^2	HS ng/ pixel	HS ng/ mm^2	Total (µg)	Total ng/pixel	Total ng/mm^2
Upper	5339.6	13.0	2.6	77.9	15.4	10.4	12.8	2.5
Lower	5045.1	12.7	2.5	74.4	14.7			
I25F								
Area Scanned	Total Protein (ng)	ng/ pixel	ng/ mm^2	HS ng/ pixel	HS ng/ mm^2	Total (µg)	Total ng/pixel	Total ng/mm^2
Upper	5302.7	14.3	2.8	92.7	18.3	11.2	14.9	2.9
Lower	5873.0	15.4	3.0	76.2	15.0			

Appendix 3.2: Occurrence of Hotspots on Instruments Acquired from Qasco, DMI and Instrapac

Table A3d. Comparison of hotspot values for each area scanned with the maximum hotspot for each instrument highlight

Instrument	Hotspot (ng)			
	DH	DT	UH	UT
Q1F	45.2	170.8	45.2	102.3
Q2F	51.7	87.1	50	218.8
Q3F	60	116.7	50.4	113.2
Q4F	50.8	93.6	62.2	217.5
Q5F	61.3	81.8	73.1	184.8
Q6F	85.8	109.3	74	101
Q7F	62.6	79.2	54.3	179.6
Q8F	94.9	75.7	85.8	53.9
Q9F	64.4	145.1	149.9	62.2
Q10F	104.5	68.7	67	110.6
Q11F	96.2	120.2	34.6	114.1
Q12F	108.9	60.9	54.3	171.3
Q13F	104.1	55.2	59.1	73.1
Q14F	29.5	40.4	52.2	39.5
Q15F	40.4	75.3	49.5	110.6
Q16L	541.3	277.3	331	536.5
Q17L	420.8	340.6	358	274.2
Q18L	106.3	95.8	127.2	61.8
Q19L	527.7	55.6	531.2	217.5
Q20L	539.9	217.1	87.9	367.2
Q21L	63.9	130.7	140.3	72.7
Q22L	122.8	83.6	68.7	110.2
Q23L	96.2	63.9	38.6	91
Q24L	118	108	46	163.4
Q25L	54.3	56.5	94.5	51.3
Occurrence of hotspot	**7**	**5**	**5**	**8**
B1F	33.8	46.9	45.2	52.2
B2F	132.9	59.1	27.7	45.2
B3F	44.7	40.4	58.3	139.9
B4F	132.9	74	29.5	53.9

B5F	96.2	85.8	66.6	57.8
B6F	67.4	78.8	41.7	48.7
B7F	69.2	174.8	238.5	191.3
B8F	65.2	111.5	361.9	257.2
B9F	259.8	23.4	86.2	151.2
B10F	544.3	538.6	88.4	89.2
B11F	40.4	82.7	406.4	326.6
B12F	335.8	185.2	90.6	41.7
B13F	54.3	60.4	253.3	45.6
B14F	78.8	33.4	110.2	46.9
B15F	52.2	150.3	39.9	41.7
B16L	54.8	64.8	95.4	136.4
B17L	87.9	70	48.7	62.2
B18L	75.3	159.9	541.3	266.4
B19L	148.6	83.6	176.1	179.6
B20L	54.8	64.8	95.4	136.4
B21L	59.1	22.5	58.7	30.3
B22L	166.9	25.5	52.6	31.7
B23L	57.8	29.5	39.9	61.8
B24L	77.5	34.7	68.3	84.4
B25L	74.8	59.6	101.9	40.8
Occurrence of hotspot	**9**	**2**	**7**	**7**
I1F	52.6	19.4	36	19
I2F	15.9	17.3	23.8	287.8
I3F	20.3	123.7	36.5	33.4
I4F	39.9	71.8	34.7	124.1
I5F	43.4	44.3	37.3	32.5
I6F	88.4	105.4	185.7	68.3
I7F	137.2	85.8	483.7	545.2
I8F	516.4	539.1	62.6	46.9
I9F	60	41.2	187.8	118
I10F	215.3	291.3	42.6	33
I11F	123.7	138.1	50	51.7
I12F	137.2	92.7	176.5	75.3
I13F	36.9	46.9	61.8	80.1
I14F	30.3	29.9	138.5	26.9
I15F	26.4	50.8	250.2	74.4
I16L	53	63.9	53	186.1

I17L	149.5	89.2	111.9	102.8
I18L	40.8	85.3	73.1	46
I19L	53	50	27.7	52.2
I20L	59.1	57.8	26.9	45.2
I21L	41.2	38.6	70.5	37.3
I22L	87.5	45.6	153.8	78.8
I23L	110.6	145.1	26.4	18.6
I24L	74.4	23.8	77.9	42.6
I25L	76.2	65.7	92.7	55.6
Occurrence of hotspot	**4**	**7**	**9**	**5**

Chapter 4: Fluorescence Studies of Proteins in the Solid State

4.1 Introduction

Tryptophan (Trp) fluorescence has been used extensively to characterise the microenvironment of proteins and the direct environment of tryptophan within proteins[1,2]. Information gained via fluorescence analysis of Trp gives insight into protein structure and dynamics, protein-protein/protein-DNA interactions and protein environment. Moreover, Trp fluorescence can be used to monitor the effect of UV exposure on proteins as its fluorescence characteristics change under light stress[3-10]. The effect of UV exposure on proteins is a vital area of research as protein photo-damage has been implicated in a variety of age-related maladies.

4.1.1 Tryptophan Photochemistry

Trp has been well characterised as a probe for protein structure, dynamics and interactions, moreover, photo-degradation products of Trp are becoming a popular diagnostic tool for protein photo-damage. The photo-degradation of Trp has been shown to produce a multitude of photoproducts as shown in Figure 4.1a**.** There are two main processes by which Trp is converted to these photoproducts which are known as type I and type II photo-oxidation[4,9-12], although Trp is most likely converted via the type II reaction[10]. In Type II photo-oxidation excited state photosensitizers such as N-formylkynurenine (NFK), which are produced during enzymatic Trp metabolism as well as during Trp photo-oxidation, or even Trp itself, transfer their energy to ground state molecular oxygen[9,10,13]. This produces excited singlet oxygen which can go on to react with aromatic substrates such as Trp.

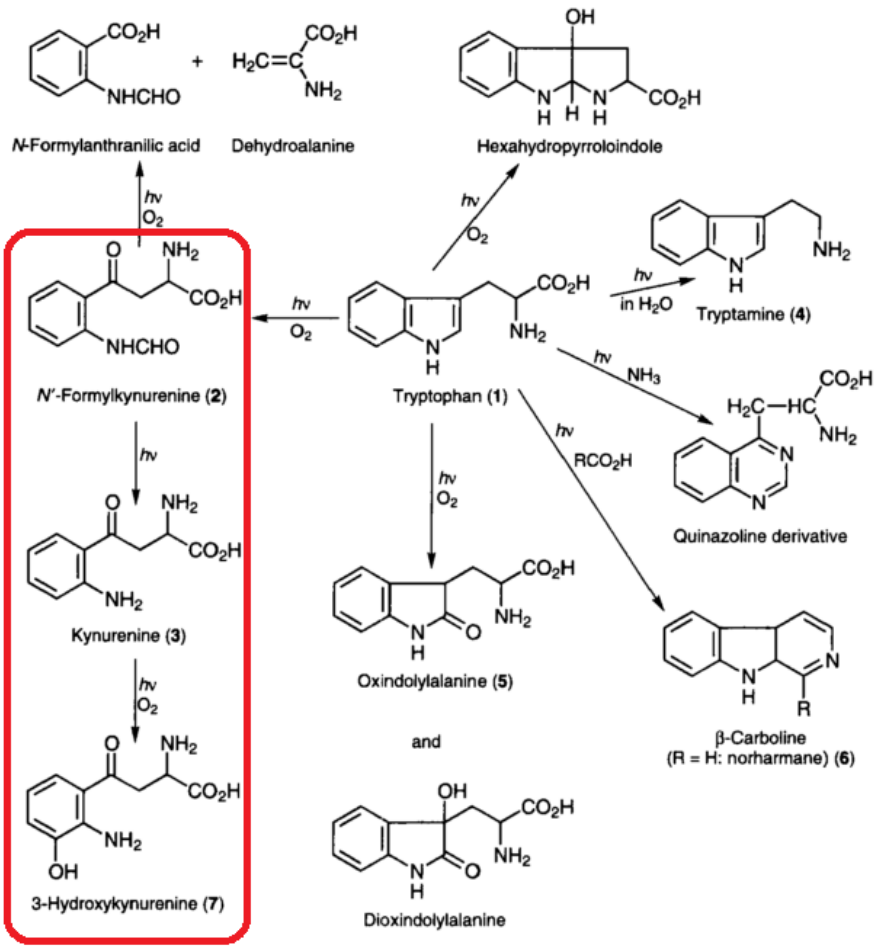

Figure 4.1a. Photoproducts of Trp. The predominant products are highlighted in red[10]

The most predominant photo-oxidation products of Trp are NFK, kynurenine and 3-hydroxykynurenine (3OHK) which are known as kynurenine-related Trp derivatives (KRTDs). Over time, Trp is converted into these intermediates upon irradiation; this can be observed visually as a colourless solution of Trp will eventually turn yellow when left in the sun[10] and yellow is the colour attributed to NFK, kynurenine and 3-OHK[8-9,13]. Moreover, the photo-oxidation of Trp to NFK was recently shown, via fluorescence analysis, to occur in solutions of human serum albumin (HSA) in the presence of a sensitizer[14]. The fluorescence spectral characteristics of NFK and kynurenine show that the peak emission wavelengths for NFK and kynurenine are at 420nm and 435nm, respectively, as shown in Figure 4.1b (bottom left and right)[9]. The photo-oxidation of Trp has been observed in a variety of protein systems and has implications in cataracts and the photo-yellowing of wool and hair. Moreover, the presence of KRTDs is used as an indicator of oxidative stress[15,16]. It should be noted that, although kynurenine emits at 435 nm in solution, in the solid state kynurenine emission shifts to 500 nm.

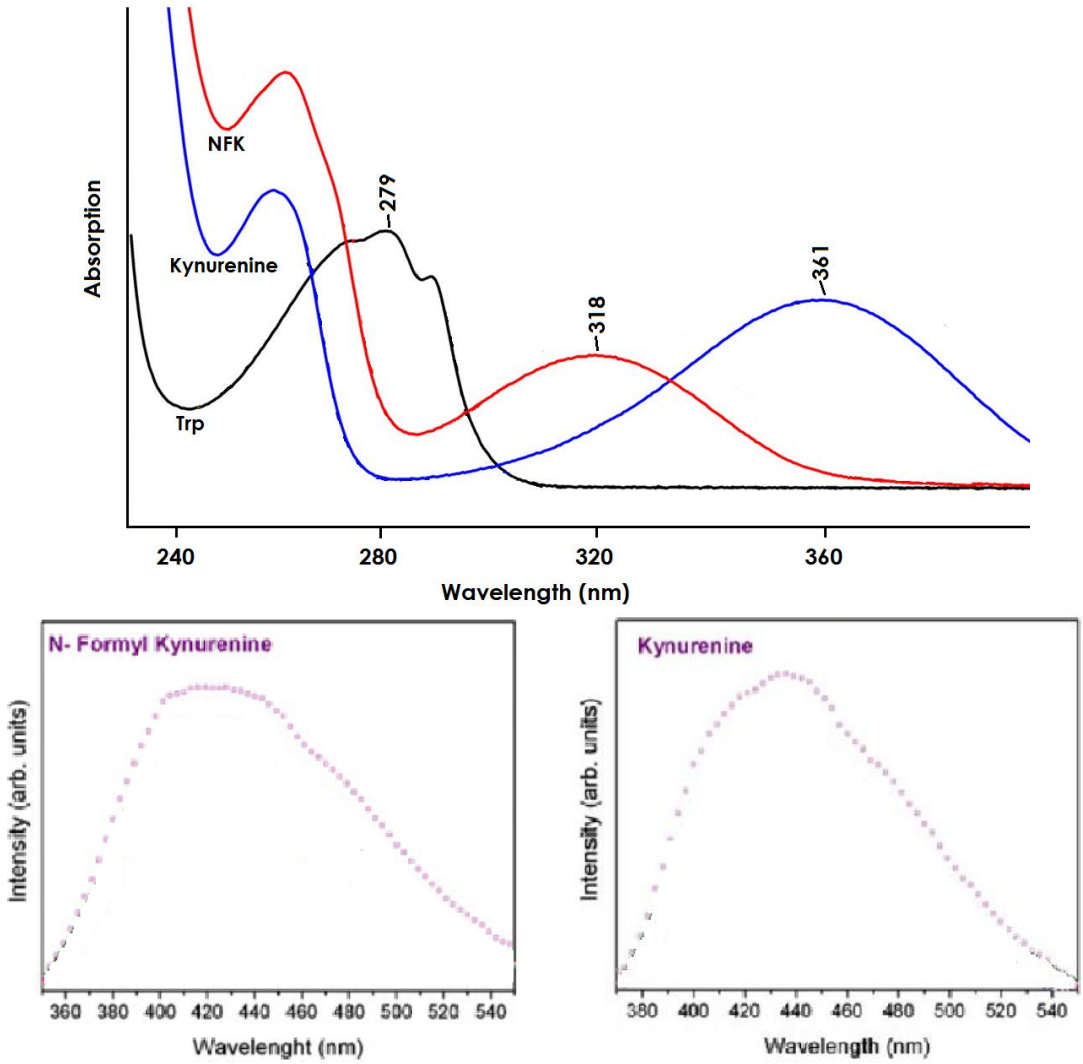

Figure 4.1b. Top - Absorption spectra of Trp, NFK and kynurenine[15], Bottom - Emission characteristics of NFK (left) and kynurenine (right) in solution[9]

4.1.2 Tryptophan Oxidation in Proteins

Trp photo-oxidation in proteins occurs over time, especially in those proteins which are regularly exposed to light, as they have evolved to resist the effects of UV exposure. However, Trp photo-oxidation plays a significant role in the formation of cataract and has been found to occur in wool and hair.

Cataracts

The proteins present in eye lenses are produced during embryonic development, experiencing a low turnover throughout life[3,4]. Consequently, these proteins, namely crystallins, boast efficient UV protection pathways; however, as a large proportion of these proteins are the same age as the individual, time takes its toll. It has been proposed that protein structural changes caused by Trp photo-degradation is one of the main causes of age-related cataracts in humans and higher mammals[3-5,17]. Crystallins are essential to the conservation of lens transparency[3] and must stay soluble to maintain their function. However, UV-induced production of KRTDs, which can react with these crystallins to form insoluble aggregates, results in clouding of the lens. This process begins with increased, long-wavelength fluorescence as KRTDs build up in the lens and is followed by visible yellowing, from here the accumulation of protein damage causes denaturation of chaperone proteins, cross-linking and aggregation of crystallins resulting in clouding of the lens. See Chapter 5 for more detail on crystallins and cataracts.

Photo-yellowing of Wool and UV-Damaged Hair

The photo-yellowing and weakening of wool has been attributed to Trp photo-oxidation in the keratin fibres of which wool is composed. As indicated above, several Trp photoproducts, such as kynurenine, are yellow in colour[12,10] suggesting that it is these species that contribute to the photo-yellowing of wool. It has been shown that converting Trp residues to oxindolylalanine reduces the degree of yellowing in irradiated wool[10], reinforcing the view that Trp photo-products are the main contributor to the yellowing of wool. The conversion of Trp to its photoproducts is also a problem in hair strands. Although pigments in the outer cuticle of hair protect the inner keratin cortex from UV light, over time the pigments become degraded or bleached[9]. Following this, light is able to penetrate the cuticle and degrade the keratin within; this light exposure has been found to produce significant loss of Trp[9]. Pande and Jachowicz[7] found that there is a significant difference between the emission characteristics of the tip and root of a hair strand[9] i.e. the oldest and youngest parts of the strand. It was shown that the tip was void of a Trp peak with increased emission around 460nm, whereas the root showed a strong Trp emission peak. Moreover, irradiation of yak hair showed a decrease in Trp emission intensity with time. Longo *et al*[7] also showed this trend when irradiating human hair. Additionally, the spectral characteristics of the photoproducts formed upon the loss of Trp were isolated and the compounds identified as NFK and kynurenine.

4.1.3 Protein on Stainless Steel Surfaces

One of the main objectives of this project was to establish a method for intrinsic detection of protein adsorbed onto stainless steel and to do so, the way in which proteins interact with stainless steel surfaces must be understood. Protein adsorption onto solid surfaces is a common process which is a well-known problem in the food industry and numerous factors influence the degree of adsorption e.g. net charge, protein size and temperature. Adsorption is protein-dependent[18-20] and is mainly governed by an increase in entropy achieved when surface water and salt are lost and the protein structure rearranges[20,21]. This dependency comes down to the considerable differences between proteins which determine the response of a protein to external parameters.

Proteins tend to rearrange as the solvent shell evaporates and they begin to adsorb onto the surface; this adjustment of conformation can mean that proteins have more than one bound state[20]. Generally, proteins adsorb most efficiently at their isoelectric points, however, ionic strength can play a significant role. Fukuzaki *et al*[18] have shown that an increase in ionic strength from 10^{-3} to 10^{-1} resulted in the adsorbed amount of BSA increasing from 2.5 mg m^{-2} to over 15 mg m^{-2}. The effect of temperature is also a factor and it was found that in the range of 40-80 °C the amount protein adsorbed increased from 2 mg m^{-2} to 14 mg m^{-2}. It has also been shown that the ions present in a protein solution can affect the extent of adsorption. A study by Poleunis et al using time-of-flight secondary-ion mass spectrometry (ToF-SIMS) has shown that the metal constituent of salts in solution form particles at the steel surface and that, in the case of BSA, protein bound preferentially around these spots[22]. Moreover, the type of metal influenced BSA adsorption with NaCl/CaCl mixtures giving weak BSA signals and NaCl/MgCl giving significantly higher BSA signals. The susceptibility of proteins to their external environment would theoretically allow for controlled desorption of proteins from stainless steel surfaces under optimised conditions, however, even extreme conditions do not remove all adsorbed protein. It has been observed that treatment with strong surfactants such as sodium dodecyl sulfate and high temperatures of 200 °C far from remove adsorbed protein[23].

Although there is some literature on the fluorescence characteristics of protein adsorbed onto stainless steel, it is scarce. This chapter aims to elucidate the emission observed from Trp residues in proteins in the solid state and adsorbed onto stainless

steel. The proteins studied were the serum proteins bovine serum albumin (BSA), bovine fibrinogen (BFG) and bovine γ-globilins, hen egg white lysozyme and bovine α- and γ-crystallins. Their structure and function are described in Chapter 1.

4.2 Materials and Methods

4.2.1 Materials and Sample Preparation

Solid state samples of tryptophan, kynurenine, BSA, Fibrinogen, γ-Globulin, Lysozyme, α-crystallin and γ-crystallin were acquired from Sigma-Aldrich and stored in accordance with manufacturer's instructions.

4.2.2 Solution State Analysis

Stock protein samples were prepared by dissolving crystalline protein in de-ionised water at a concentration of 3 mg/ml; 3 ml aliquots of stock solution were frozen for each protein analysed. For analysis, aliquots were defrosted in a fridge and the solution diluted with de-ionised water accordingly.

4.2.3 Solid State Analysis

For steady-state analysis protein crystals were mounted on to double sided, non-fluorescent, adhesive carbon tape (Agar scientific) – often used for SEM and EDX applications - fixed to a glass slide. Optical fibres, coupled to the fluorescence spectrometer, were arranged as shown in Figure 4.2a (top). The same optical set-up was used for the steady state analysis of protein adsorbed onto stainless 316L stainless steel disks.

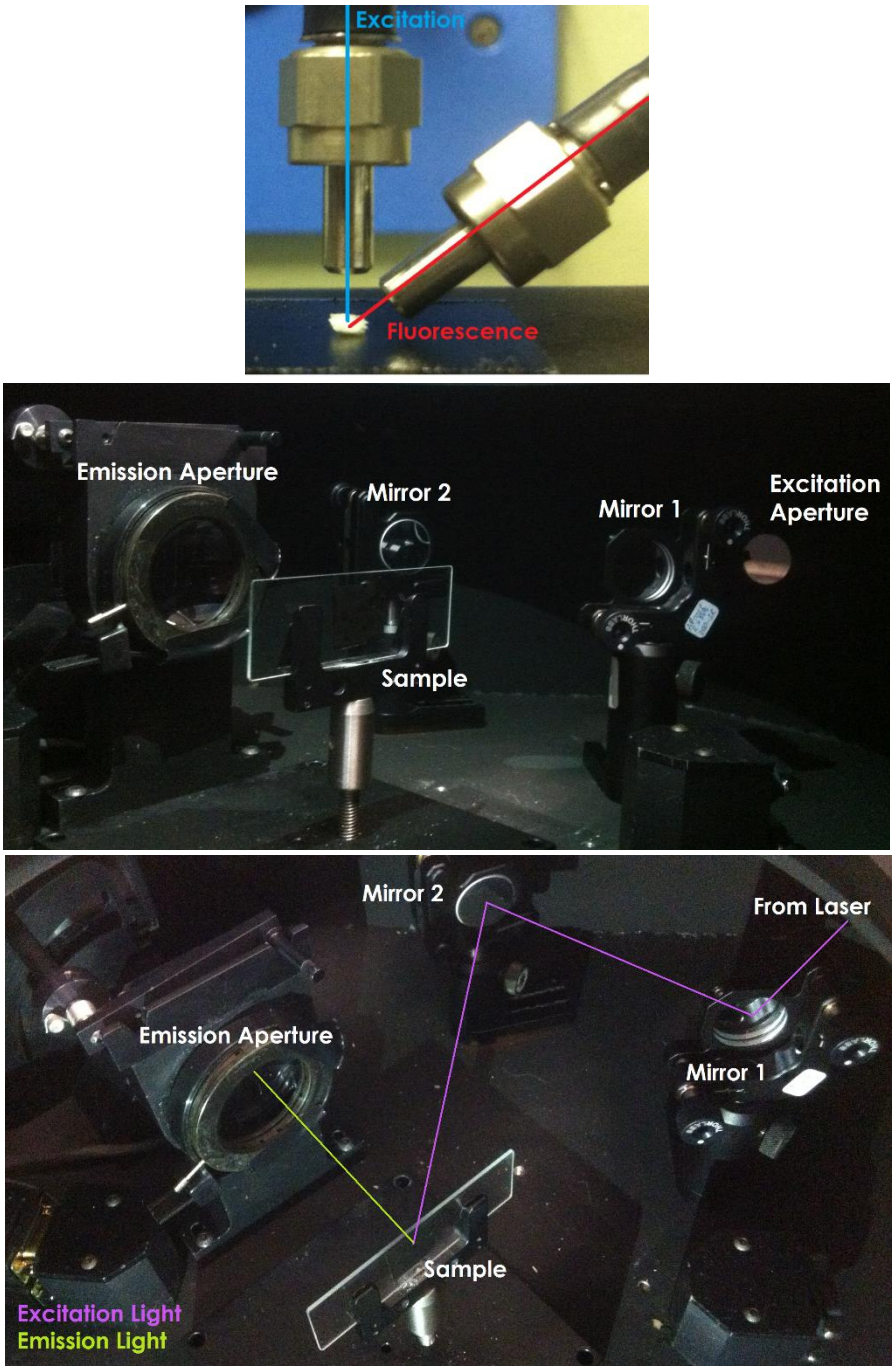

Figure 4.2a. Top - Protein crystal fixed to non-fluorescent tape with optical fibres positioned above for steady state analysis, Middle – Image of set-up within the sample chamber for the measurement of solid state fluorescence lifetimes, Bottom – Time-resolved set-up showing path of light

Samples for time resolved analysis were prepared correspondingly and mounted into the sample chamber (Figure 4.2a middle and bottom). The slide mounted sample was held in a plate filter holder and secured in–line with the emission aperture. A 310 nm long-pass filter was placed in front of the exit aperture to ensure no excitation light

reached the detector. Excitation light from the laser was direct through the centre of the excitation aperture onto the first of two aluminium mirrors with 85% reflectance efficiency. Mirror 1 was manoeuvred to direct the excitation light onto mirror 2 which was manoeuvred to direct the light onto the sample. The sample position was optimised to give a strong signal and neutral density filters were used to reduce the signal intensity to 10 000 counts for the lifetime acquisition for each sample. The excitation wavelength for all lifetime measurements was 282 nm and the detection wavelength was 340 nm for all of the protein analysed in this study, excluding BSA. During BSA analysis it was possible to collect a suitable IRF, however, limitations of the set-up used meant that this was not the case for the other proteins. BSA lifetimes represent a global fit between 330, 340 and 350 nm emission wavelengths. Lifetime acquisition took approximately 8 minutes for each emission wavelength. The exposure of crystalline samples to excitation light on the timescale of the measurement lead to a slight decrease of approximately 1000 to 2000 counts for each sample due to photo-degradation of Trp residues. In the case of BSA a decrease of approximately 4000 counts was observed.

4.2.4 Irradiation of Samples

Samples were irradiated using the optical set-up shown in Figure 4.2a (top) with the fibres coupled to the fluorescence spectrometer. The desired irradiation wavelength was set and the excitation slit opened to 5 nm while the emission slit remained closed. Samples were irradiated for 60 minutes at each irradiation wavelength. Both the sample and apparatus remained in place throughout the sequential photo-bleaching and analysis process.

4.2.5 Eggometer MK2

The Eggometer system, which was designed, built and developed within the Jones group for another project, consists of two measurement arms contained within a robust metal enclosure. One arm measures reflectance via an ocean optics fibre reflectance probe, the other performs an epi-fluorescence measurement on a sample. The reflectance arm was not used in this work.

The fluorescence arm of the Eggometer comprises of an Ocean Optics 290nm LED (LLS-290) and an Ocean Optics USB 2000+ spectrometer optimized for 180-780nm

detection, which are linked to a dichroic cube (Thorlabs CM1-DCH/M) containing a Semrock long pass dichroic mirror with a cut-off at 310 nm (Semrock FF310-Di01-25x36). The LED is coupled to the cube via a 600 um core Ocean Optics optical fibre connected to a lens holder which contains a collimating lens. The excitation light is reflected by the dichroic up to the sample surface through the top of the main chamber. Returning fluorescence from the sample passes through the dichroic and is collected by a second lens into a 600um core fibre where it is guided to the spectrometer. There is a further filter on the excitation side of the dichroic cube to limit the broad spectrum of the LED to below the emission spectrum of Trp. The details of the system are illustrated in the schematic in Figure 4.2b.

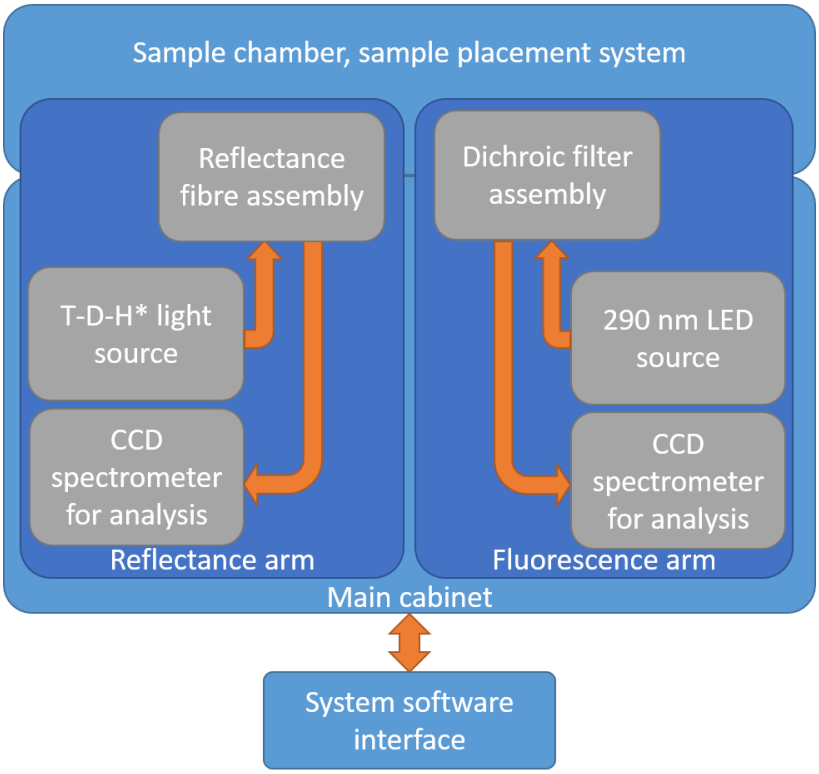

Figure 4.2b. Block diagram of the Eggometer MK2 system – only the fluorescence arm (right) of the assembly was used in this study *Tungsten-Deuterium-Halogen

All of the optical components are placed below the sample making for rapid easy sample placement above the dichroic cube, the system is shown below measuring an awkward sample, a chicken egg, with the main components highlighted. A Matlab program was written to integrate with the spectrometers to record spectra and perform any necessary calculations. To set the correct integration time for the spectrometer a sample is placed above the dichroic cube and the integration time adjusted to maximize signal whilst avoiding saturation which occurs at 55000

counts. The sample is then removed and a background spectrum is recorded with the instrument lid closed. This is then subtracted by software from any subsequent measurements. Disks loaded with varying amounts of protein were fixed onto non-fluorescent tape adhered to a glass slide and the slide placed face down on the excitation aperture for analysis.

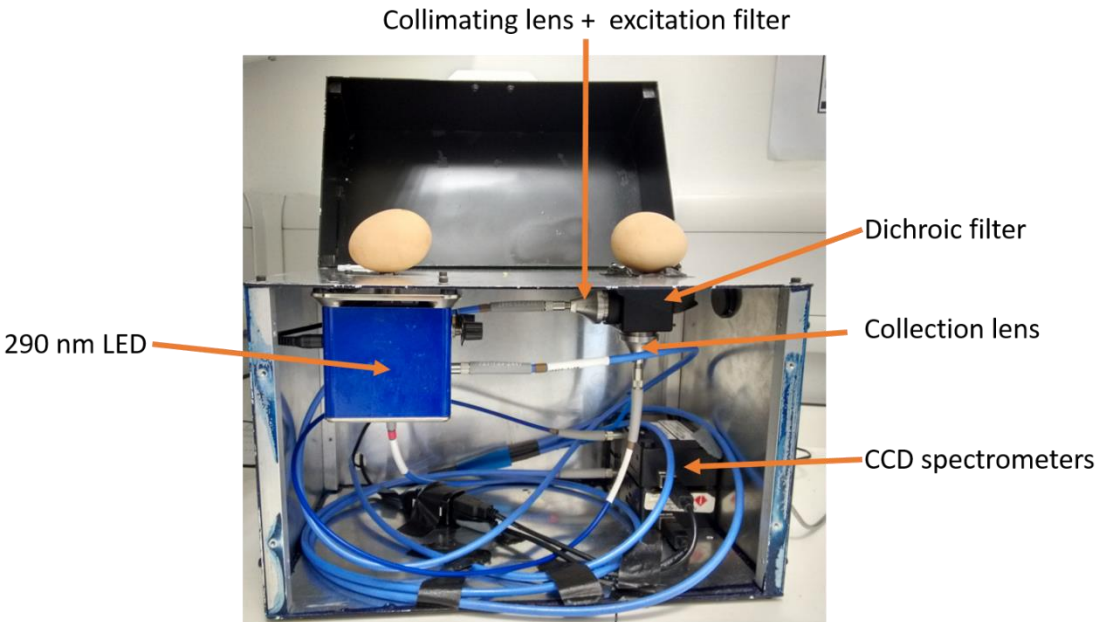

Figure 4.2c. Image of the inside of the Eggometer MK2

4.3 Results and Discussion

4.3.1 Investigation of photo-oxidation in BSA

Analysis of proteins in the solid state began with the investigation of photo-oxidation in BSA. Although analysis of the literature supports that the long wavelength emission observed from BSA (Chapter 3) can be attributed to NFK and kynurenine, confirmation is essential to understanding the fluorescence observed from other proteins in the solid state. To confirm the underlying process that occurs upon irradiating BSA, an irradiation study was carried out. A single BSA crystal was irradiated sequentially at 290 nm, 320 nm and 360 nm for 60 minutes and an EEM recorded before irradiation and after irradiation at each wavelength. Figure 4.3a shows how the fluorescence characteristics of a BSA crystal changes with irradiation.

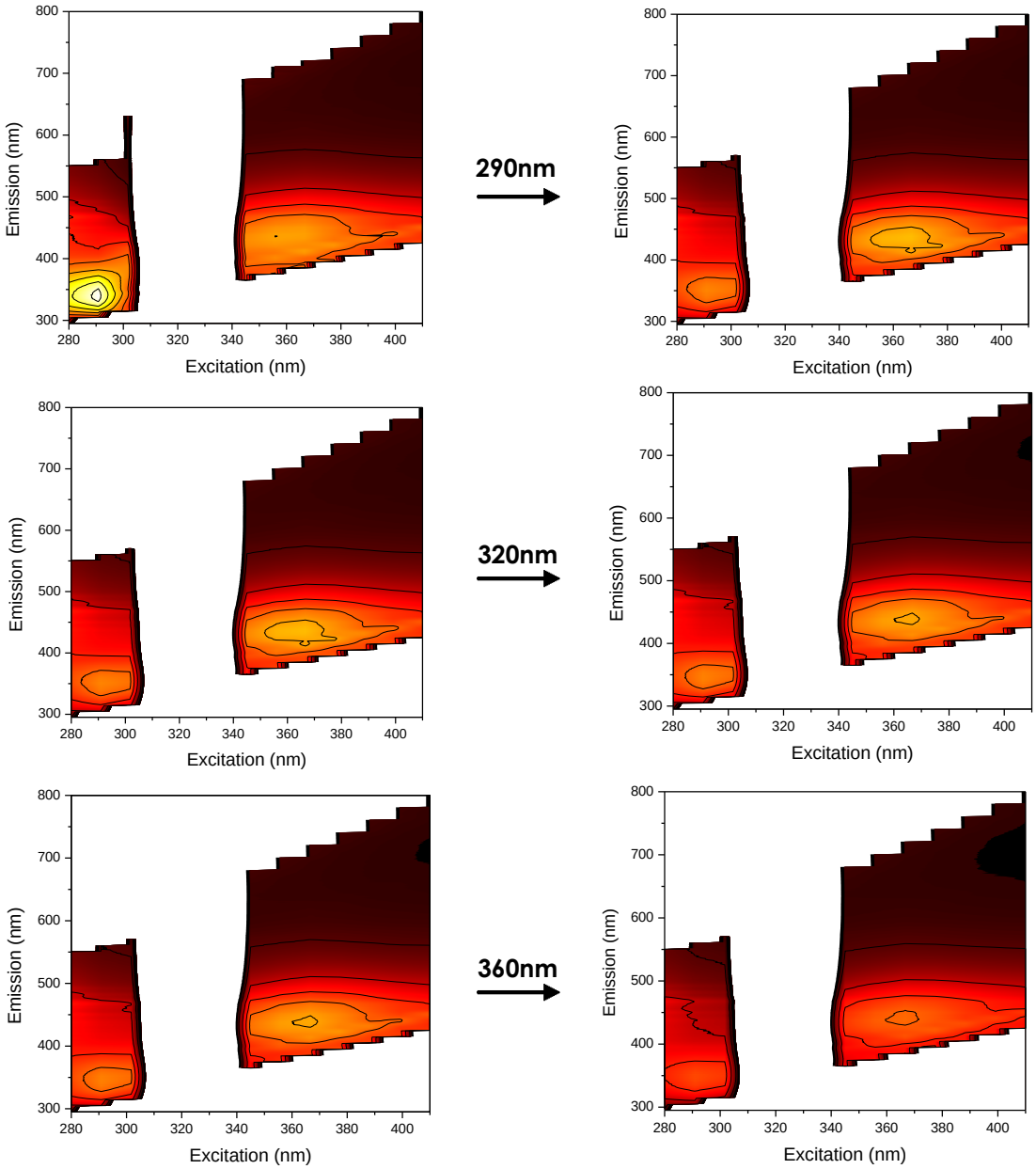

Figure 4.3a. Change in emission characteristics for a BSA crystal irradiated at 290 nm, 320 nm and 360 nm NB: Spectra excited from 310nm – 350 nm are omitted for clarity

Before irradiation a strong Trp emission at 340 nm is observed, with an excitation maximum around 290 nm, as well as some long-wavelength emission around 425 nm, with an excitation maximum around 360 nm. The presence of the long-wavelength emission indicates that some photo-degradation of the Trp had already occurred, prior to these experiments. Following irradiation at 290 nm, the absorption maximum for Trp, emission intensity at 340 nm fell by 51% and a 5% increase in emission intensity at 425 nm was observed, indicating the conversion of Trp to NFK.

The decrease in Trp emission intensity on irradiation greatly exceeds the observed increase in NFK emission. This suggests that the fluorescence quantum yield of the Trp that is destroyed is much greater than that of the NFK that is formed. However, it may also indicate the formation of non-fluorescent photoproducts that are not apparent in these measurements.

To confirm the formation of NFK, the crystal was irradiated at the absorption maximum for NFK, 320nm, which induced a decrease in emission intensity at 420 nm and a shift of the long wavelength emission to 435 nm. These observations suggest that a proportion of the NFK originally present, as well as that produced during irradiation at 290 nm was converted to kynurenine. Further confirmation was achieved by irradiating the crystal at the absorption maximum for kynurenine, 360 nm, and observing the bleaching of the long wavelength emission. Upon oxidation, kynurenine is converted to 3OHK which has an extremely low quantum yield[24], suggesting that irradiation at 360 nm resulted in conversion of kynurenine to 3OHK.

As is evident, irradiation of a BSA crystal results in the following photo transformation Trp > NFK > kynurenine > 3OHK. The interaction of singlet oxygen with BSA in solution under sensitized conditions has been shown by Gimenez *et al*[25] to result in the conversion of Trp residues to NFK with the exposed Trp 134 preferentially oxidized over the buried Trp 213. This is unsurprising as exposed residues will come into contact with more singlet oxygen ($^1O_2$), however, modelling of BSA interacting with $^1O_2$ revealed that $^1O_2$ can diffuse into the BSA structure towards buried residues such as Trp 213, aided by highly hydrophobic surrounding residues. It is proposed that initiation of the reaction in the solid state occurs via direct radical production associated with Type I photo-oxidation, and that the reaction propagates via Type II photo-oxidation. Type I photo-oxidation occurs when Trp absorbs incident light to create excited states or radicals which can then go on to react intrinsically or with nearby residues. As a consequence of this photochemistry and its effect on Trp fluorescence, it is clear that BSA is not suitable for use as a calibration standard for the intrinsic fluorescence of surface-bound protein. To determine whether a suitable standard for the intrinsic detection of protein could be found, other possible protein standards were studied.

4.3.2 Fluorescence Characterisation and Irradiation of Fibrinogen, γ-Globulins and Lysozyme

The serum proteins fibrinogen (BFG) and γ-globulins are concentrated in the blood and are highly likely to be present on re-usable surgical instruments; making them promising candidates as fluorescence standards. Another candidate comes in the form of lysozyme which is commonly used in assays and is known as the 'physicist's protein', therefore, lysozyme was also considered as a possibility,

Fibrinogen

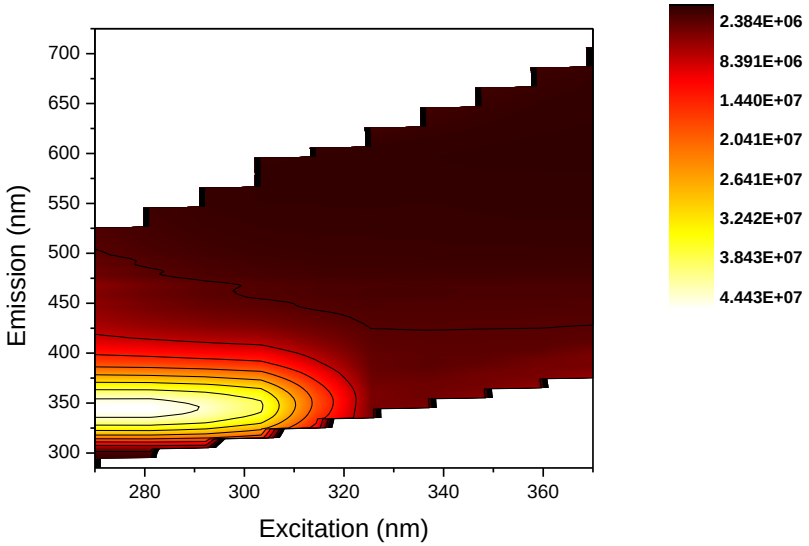

Figure 4.3b. EEM of a BFG crystal prior to irradiation

Due to the size of BFG it is highly likely that it will make up a considerable proportion of proteinaceous contamination remaining on reprocessed surgical instruments. BFG differs greatly from BSA in its Trp content, containing a very large number of Trp residues, 72. Figure 4.3b shows the emission characteristics of BFG in the solid state, showing that emission is dominated by Trp fluorescence at 345 nm with no long wavelength emission, unlike BSA which showed some NFK emission prior to irradiation. This suggests that BFG may be more photo-stable, with respect to Trp photo-oxidation, than BSA, however, irradiation studies were carried out to determine the effect of UV exposure on Trp emission.

Irradiation at 290 nm induced a large, 62% decrease in Trp emission intensity at 345 nm, however, no long-wavelength emission emerged (Figure 4.3c). Subsequent sequential irradiation at 320 nm and 360 nm produced no further significant decrease in Trp fluorescence (Table 4.1) and no measureable change in long wavelength emission. The small decrease in Trp emission intensity following 320 nm

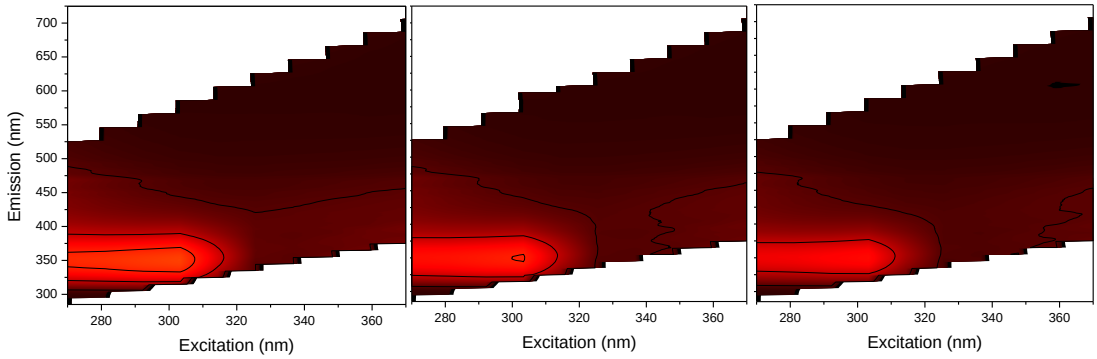

Figure 4.3c. EEM for the irradiation series of a BFG crystal Left - EEM following 290 nm irradiation, Middle - EEM following 320 nm irradiation and Right - EEM following 360 nm irradiation (scale is the same as that in Figure 4.3b)

irradiation may be due to weak absorption in the long-wavelength tail of the Trp absorption spectrum. However, the small effect of irradiation at 360 nm cannot be due to absorption by Trp and suggests some indirect effect on Trp fluorescence as a result of photochemistry of a non-fluorescent photoproduct that absorbs at this wavelength. Although no long-wavelength emission was evident in the EEMs, when emission spectra were analysed individually a small change in spectral position was observed (Figure 4.3d). Following irradiation, the peak emission intensity shifts from 345 nm to 350 nm. As mentioned in the introduction, Trp emission is red-shifted with increasing polarity. This suggests that the Trp residues that are resistant to photo-bleaching in BFG are present in a more polar environment than those that are destroyed. Additionally, the observed shift may be partly due to the creation of a

Protein	Decrease in emission intensity (%)		
	290 nm	320 nm	360 nm
BSA	49	50	61
Fibrinogen	62	69	74
γ-Globulins	30	34	37
Lysozyme	36	44	51
α-Crystallin	54	58	53
γ-Crystallin	60	64	66

Table 4.1: Percentage decrease in Trp emission intensity for BFG, γ-globulins, lysozyme, α-crystallin and γ-crystallin following sequential irradiation at 290 nm, 320 nm and 360 nm, for 60 minutes at each wavelength

small population of NFK and kynurenine resulting in a red-shift of the summed emission from all fluorophores present. However, analysis of individual spectra excited at 320 nm and 360 nm (data not shown) show a negligible change in emission intensity with irradiation, suggesting that photo-oxidation of Trp to NFK and kynurenine is not the dominant process occurring upon irradiation of BFG. The photobleaching observed here can likely be attributed to photo-ionisation of Trp[26]. UV irradiation below 300 nm is known to ionise Trp to the Trp cation[27-29]. The Trp cation can be reduced by electron back-transfer, in which case photo-ionisation is merely a reversible quenching process, or it can be deprotonated to yield a Trp radical which can undergo further irreversible reactions with other residues, resulting in photo-bleaching. Although much less widely reported than photo-oxidation, Trp photo-ionisation has been observed previously to be a mechanism of photo-bleaching of intrinsic protein fluorescence (in solution).

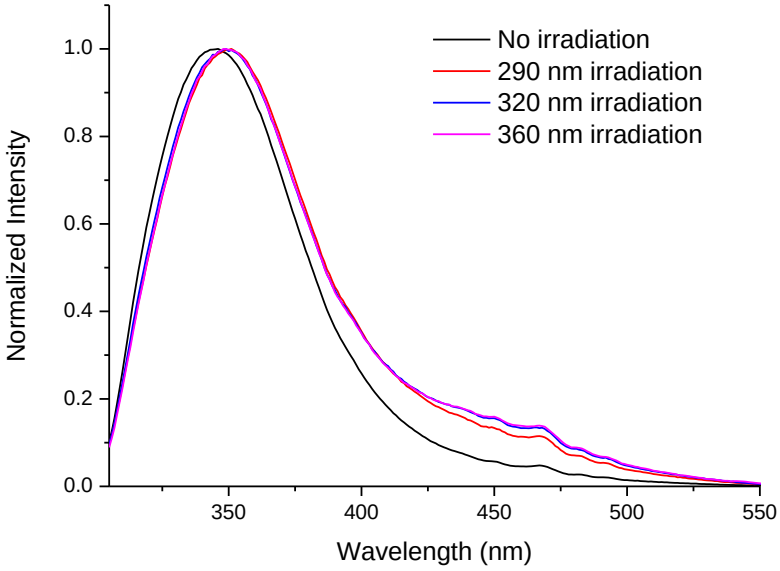

Figure 4.3d. Change in position and shape of emission spectrum for a BFG crystal excited at 290 nm (black), following irradiation at 290 nm (red), following irradiation at 320 nm (blue), following irradiation at 360 nm (pink).

Although a significant fraction of the Trp residues in BFG are susceptible to photo-bleaching, photo-oxidation does not appear to occur on a measurable scale. Moreover, the photo-bleaching is sufficiently slow that on the timescale of the measurement of an emission spectrum (approx. 2.5 minutes) emission intensity at 345 nm was not appreciably affected. These observations suggest that BFG may be a suitable candidate as a standard for the intrinsic detection of protein on steel.

Lysozyme and γ-Globulins

Lysozyme is more comparable in Trp content to BSA, containing 6 Trp residues, whereas γ-globulins contain a range of Trp quantities. These proteins showed similar behaviour to BFG upon irradiation. No long-wavelength emission was observed before irradiation and substantial photo-bleaching was induced by irradiation at 290 nm, causing a ~30% decrease in Trp emission intensity at 340 nm (Table 4.1); no emission intensity was observed a longer wavelengths, although there was a slight shift in Trp emission wavelength, as seen for BFG. As with BFG, subsequent irradiation at 320 nm and 360 nm produced a further small decrease in emission intensity. The timescale of photo-bleaching was such that there was negligible change in Trp emission intensity during the time taken to measure an emission spectrum (approx. 2.5 minutes). The similarity in fluorescence changes compared with BFG suggest that a similar photochemical process occurs in all of these proteins. Although emission intensity decreases significantly following irradiation of lysozyme and γ-globulins, the fractional decrease in intensity is only approximately half that observed for BFG. This suggests that a smaller fraction of the Trp residues are susceptible to photo-ionisation and/or those residues that are not susceptible to photo-bleaching display a higher quantum yield. The similarity in fluorescence changes compared with BFG suggest that a similar process occurs in all of these proteins. This is corroborated by the observed shift in Trp emission wavelength following irradiation of lysozyme and γ-globulins. These observations are upheld by the position of Trp residues in BFG, lysozyme and γ-globulins. As shown in Chapter 1, the majority of Trp residues found in these proteins are buried in the core of the protein structure and are therefore quenched and less likely to photo-ionise.

These observations are promising as, although some Trp residues are susceptible to photo-bleaching following extensive irradiation, on the timescale of a single emission measurement there is little change in Trp emission intensity; making both γ-globulins and lysozyme possible candidates for a fluorescence standard.

Fluorescence Characterisation and Irradiation of Crystallins

Crystallins are of particular interest in the present context as they are proteins which have evolved to resist photo-oxidation. Within the ocular lens, crystallins undergo extremely low metabolic turnover and those found in the centre of the lens are present from birth, however, protein damage does not become obvious until old age, when cataracts begin to form. Fluorescence characterisation of α-crystallin, which

are composed of A and B chains with 1 and 2 Trp residues respectively, and γ-crystallins, which contain 4 or 5 Trp residues, showed that, once again, no long-wavelength emission was observed before irradiation. Following irradiation at 290 nm, emission intensity at 340 nm decreased by 54% for α-crystallin and 60% for γ-crystallin (Table 4.1). Subsequent irradiation at 320 nm and 360 nm caused negligible changes in emission intensity at 340 nm. A slight red-shift of the emission spectra also occurred on irradiation, as was observed for BFG, lysozyme and γ-globulins. It is notable that Trp in these crystallin proteins, although apparently resistant to photo-oxidation, undergoes photo-bleaching, attributed to photo-ionisation, on a short timescale, under the present experimental conditions. This photo-degradation process does not occur in the lens, implying that photo-ionisation of Trp either does not occur or is reversible under the prevailing physiological conditions. This observation may be explained by work from Chen *et al*[3] which shows that in γD-crystallin Trp residues are protected via energy transfer between residues followed by electron transfer to the protein backbone. In γD-crystallin, energy transfer is observed between two sets of paired proteins; Trp 130 to Trp 156 and Trp 42 to Trp 68, therefore quenching the fluorescence of Trp 130 and Trp 42. This is followed by electron transfer from Trp 156 and Trp 68 to the protein backbone, therefore quenching the fluorescence of the remaining Trp residues. This serves to reduce the incidence of excited state reactions which could lead to covalent damage of the protein and such processes may contribute to the resistance of the other proteins studied to photo-oxidation.

The positional dependency of Trp photo-bleaching within a protein (in anaerobic solution) has been studied by Pigault and Gerard[30] and it was found that several factors are involved in this complex process. The most important element in the susceptibility of Trp residues to photo-bleaching was found to be the tertiary structure of the protein i.e. the polarity of Trp local environment. Generally, the more polar the environment, or the closer the Trp residue is to the surface of the protein, the more susceptible the residue is to photo-bleaching. This would suggest that the red shift in Trp emission observed following irradiation of the proteins analysed in this study is likely to be attributed to the creation of a small population of NFK and kynurenine or, perhaps, an effect of the products of Trp photo-ionisation, as the population of Trp residues remaining following irradiation are more likely to be found in a less polar environment to those that were bleached. To a far lesser extent the primary structure of the protein and the proximity of other amino acids due to the tertiary and quaternary conformation of the protein also contribute to photo-

bleaching susceptibility, however, no specific amino acid sequences or spatial arrangements have been identified as deleterious. It should be noted that differences in Trp photo-bleaching in the solution and solid phase are little studied and a comprehensive investigation into the effect of Trp local environment in each state would prove useful in understanding the complexities of Trp photo-bleaching in proteins.

4.3.3 Characterisation of Fibrinogen Fluorescence on Stainless Steel

The aforementioned characterisation and irradiation of proteins relevant to the intrinsic detection of proteinaceous contamination on surgical instruments suggests that BFG, γ-globulins and lysozyme may be suitable candidates as reference standards. BFG is a very large protein, therefore it is likely to adsorb strongly to surfaces and be present on reusable surgical instruments following surgery. Moreover, the emission intensity of BFG is high due to the large Trp content and remains so even after UV exposure, therefore, BFG was taken forward for analysis on steel. The next step in determining the suitability of BFG as a standard was to characterise its fluorescence on a stainless steel surface. Figures 4.3e and f show the decrease in emission intensity for 20 µL droplets of BFG drying onto stainless steel.

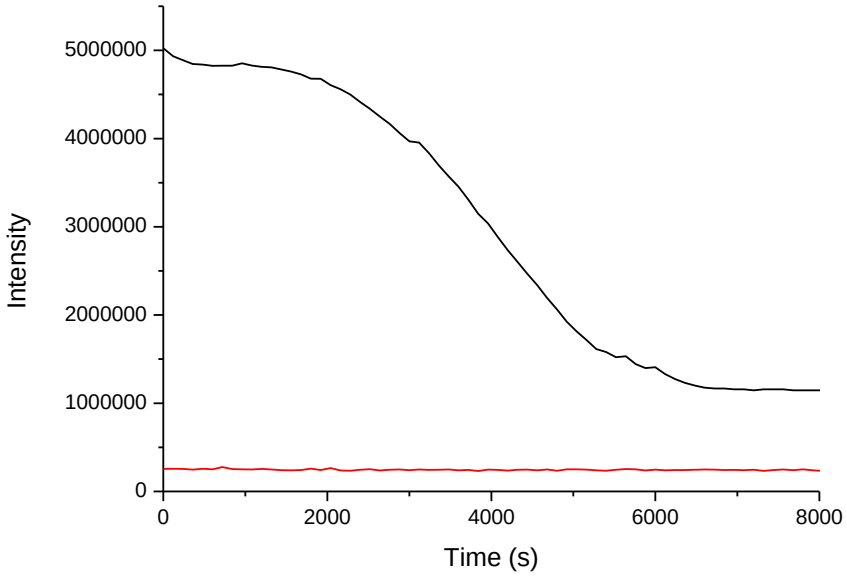

Figure 4.3e. Emission intensity as a function of time of an 8.8µM droplet of fibrinogen drying onto a stainless steel disc. A blank disk is shown in red

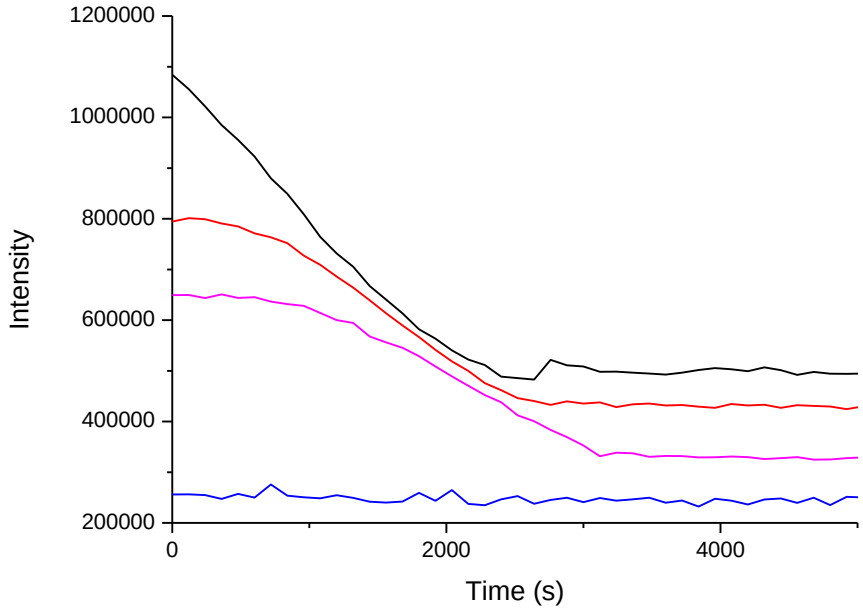

Figure 4.3f. Emission intensity as a function of time for a 880 nM (black), 88 nM (red), 8.8nM (pink) droplet of fibrinogen drying onto a stainless steel disc. A blank disk is shown in blue

A significant decrease in emission intensity of, on average, 50% (Table 4.2) is observed as the protein dries and adsorbs on to the stainless steel surface. Upon adsorption, Trp fluorescence is quenched due to energy transfer from Trp to the stainless steel surface, this quenching can be observed as a function of time as water is lost from the droplet and the Trp residues interact more closely with the stainless steel surface. Such a degree of quenching poses a problem as the concentrations of protein found on surgical instruments, although high in terms of the transfer of disease, is low in terms of Trp detection. To establish the limit of detection of BFG, steel discs loaded with varying amounts of BFG were analysed using prototype instrumentation designed specifically to detect and measure Trp fluorescence.

Concentration	Decrease in emission intensity(%)
8.8 μM	77
880 nM	54
88 nM	46
8 nM	49

Table 4.2: Percentage decrease in emission intensity for droplets of decreasing concentration drying onto stainless steel

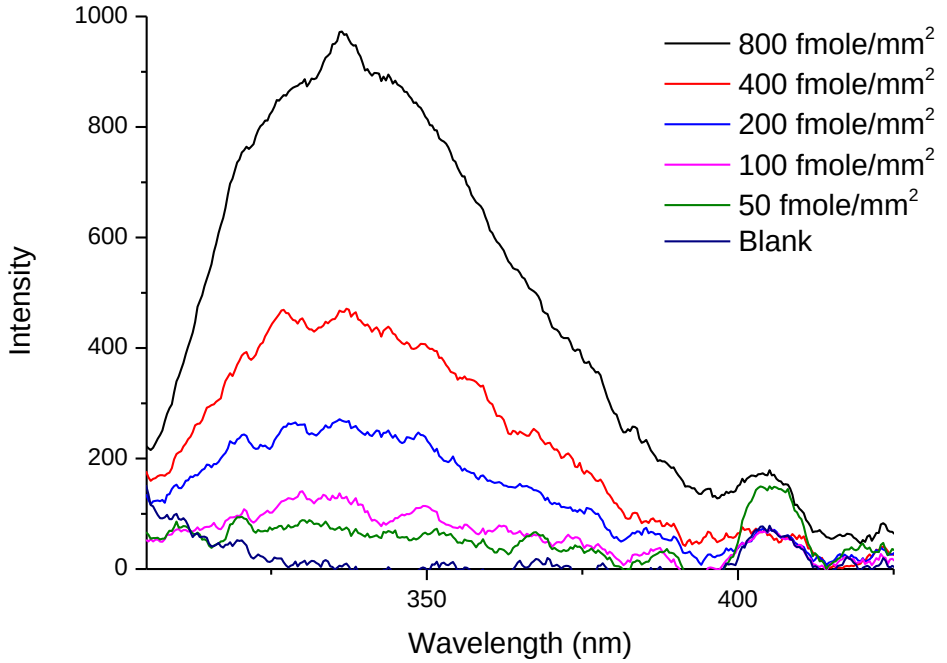

Figure 4.3g. Emission intensity as a function of amount of fibrinogen loaded onto stainless steel discs

Figure 4.3g shows the decrease in emission intensity as the amount of BFG loaded onto the discs decreases. Despite the quenching of Trp emission by the stainless steel surface, emission can be reliably observed down to 0.375 µM which equates to 200 fmole mm^{-2} of BFG (14.5 pmole mm^{-2} of Trp). This is a promising result as the instrumentation used was designed to detect Trp from sources with stronger emission, therefore, further development would likely result in an even lower limit of detection, closer to that of the current EFScan system which is 0.15 femtomoles of BSA per mm^2. These results suggest that intrinsic detection of protein adsorbed onto stainless steel is possible and, with further development of instrumentation, lower limits of detection are likely to be reached; whether or not these detection limits will be comparable to those achieved using FITC remains to be seen.

4.3.4 Time Resolved Analysis of Protein Crystals and Protein Adsorbed Onto Stainless Steel

To further understand the fluorescence characteristic described above, time-resolved measurements of BSA, Fb, lysozyme and γ-globulins crystals were carried out, in addition to the analysis of BFG adsorbed onto stainless steel.

BSA Crystal Before and After Irradiation

The fluorescence decay of Trp in BSA was measured for a solution of BSA and for crystalline BSA before and after irradiation at 290 nm. The decay parameters are given in Table 4.3.

	A-factors				Lifetimes / ns				<τ>/ns
	A_1	A_2	A_3	A_4	τ_1	τ_2	τ_3	τ_4	
Solution	0.21	0.20	0.26	0.34	0.10	0.79	2.8	6.3	3.0
Crystal Before Irradiation	0.45	0.13	0.29	0.13	0.06	0.70	2.1	4.4	1.3
Crystal After Irradiation	0.46	0.26	0.21	0.07	0.09	0.63	1.7	3.9	0.83

Table 4.3. Fluorescence decay parameters for BSA in solution and for a BSA crystal before and after irradiation at 290 nm. <τ> is the average lifetime.

As shown in Table 4.3, the Trp fluorescence decay in BSA, in all three systems, is best described by four exponential components with typical lifetimes of ~0.1 ns, ~0.7 ns, ~2 ns and ~4 ns. This indicates that Trp experiences a wide range of quenching interactions, ranging from extremely quenched (τ_1) to unquenched (τ_4). In solution phase, the amplitudes (A factors) of or populations representing the four lifetime components are all similar in magnitude, indicating similar populations of the emitting Trp species in the different protein environments represented by the lifetimes. On going from solution to the crystalline state, the shortest and longest lifetimes decrease significantly, indicating that the change in phase causes a change in local environment of these Trp species that results in increased quenching. There is also a significant increase (by a factor of 2) of the population of the shortest lifetime component, suggesting a change in protein conformation on crystallisation that results in almost half the Trp population existing in a highly quenched environment. Following irradiation, the lifetime values do not vary significantly, however, there is marked decrease (by about 50%) in population of the longest lifetime component (A_4). It is clear that irradiation induces the oxidation of those Trp residues which are the least quenched. These residues are likely to be Trp 134 which is exposed on the surface of the protein and will therefore be more accessible to oxidation. Moreover, their longer excited state lifetimes means that photochemical reactions can compete effectively with other non-radiative decay processes. There is also a noticeable decrease in the population of moderately quenched Trp (A_3). This may be due to photo-oxidation, but could also be due to photo-ionisation. The occurrence of photo-

ionisation, as well as photo-oxidation, in BSA could account for the discrepancy between the large decrease in Trp fluorescence and the small increase in NFK fluorescence, observed in the steady-state measurements (section 4.1).

Examination of the average lifetime indicates the effect of photo-degradation on the fluorescence quantum yield. The average lifetime decreases from 1.3 ns to 0.83 ns on irradiation, corresponding to a decrease in quantum yield (QY) of about 35%. The photo-bleaching of the fluorescence intensity is thus disproportionate to the number of Trp residues destroyed, since those residues with the highest QY are selectively photo-oxidised leaving behind a less fluorescent population.

NB: Due to time constraints BSA was the only protein analysed before and after irradiation. Additionally, analysis of lifetime data at longer wavelengths (420/435 nm), corresponding to NFK and kynurenine, was not possible for the same reason.

Lysozyme and γ-Globulins Crystals

The fluorescence decay parameters of lysozyme and γ-globulins, in solution and the crystalline state, are shown in in Table 4.4. (Measurements were not made on irradiated crystals because of lack of time).

	A-factors				Lifetimes /ns			
	A_1	A_2	A_3	A_4	τ_1	τ_2	τ_3	τ_4
Lysozyme Solution	0.47	0.27	0.20	0.06	0.09	0.52	1.8	4.4
Lysozyme Crystal	0.50	0.27	0.17	0.05	0.10	0.62	1.9	4.6
γ-Globilins Solution	0.43	0.36	0.17	0.05	0.07	0.49	1.5	4.4
γ-Globilins Crystal	0.48	0.24	0.20	0.08	0.07	0.68	2.0	4.7

Table 4.4. Fluorescence decay parameters for lysozyme and γ-globulins, in solution and solid phase.

The two proteins show rather similar decay parameters and, in both cases, there is no significant difference between solution-phase and solid-state decay properties. The decay parameters of these proteins differ significantly from those of BSA prior to irradiation in that they show only a very small fractional population (a few percent) of the longest lifetime, surface-exposed Trp species (most likely Trp 62 in lysozyme). This is consistent with the observed resistance of these proteins to Trp photo-oxidation. It is interesting to note that the decay parameters of these proteins (unirradiated) resemble those of BSA after irradiation, that is to say that the photo-

oxidation-resistant Trp residues in all three proteins appear to exist in molecular environments where they experience similar quenching interactions.

Fibrinogen Crystal and Fibrinogen on Stainless Steel

As BFG is a potential candidate as a fluorescent standard for intrinsic protein detection its lifetime characteristics on the surface of stainless steel were also analysed. The fluorescence decay parameters of crystalline BFG and those of BFG deposited on stainless steel are given in Table 4.5. Unlike the other proteins, the fluorescence decay of Trp residues in crystalline BFG is best described by three exponential terms; the very short (< 0.1 ns) lifetime component is absent. The population of the longest lifetime component (A_4) is much greater than in the other crystalline proteins, resulting in an average lifetime (and hence QY) that is twice that of crystalline BSA. Upon adsorption onto steel at a surface density of 0.4 nmole mm^{-2} all lifetime values decrease and a fourth, shorter lifetime of 0.24 ns is observed, although this has a very small population of only 2%. The populations of the unquenched (A_4) and moderately quenched (A_3) component decrease substantially. These observations are consistent with quenching of the Trp fluorescence as a result of interaction of the residues with the stainless steel surface. The overall effect of the quenching is a reduction of average lifetime from 2.6 ns to 1.5 ns. When the amount of BFG on the surface is decreased to 0.2 nmole mm^{-2} the lifetimes decrease further and there is substantial shift in population to the shortest lifetime component, as a much greater proportion of the Trp residues are subject to efficient quenching by the stainless steel surface. The average lifetime is reduced to 1.0 ns. Again, it is interesting to note that the decay parameters of BFG adsorbed onto stainless steel resemble those of a BSA crystal after irradiation and of lysozyme and γ-globulin crystal before irradiation. This indicates that, upon adsorption, the Trp residues of BFG exist in more quenched molecular environments and, therefore, will be more resistant to photo-chemical reactions.

	A-factors				Lifetimes/ns				<τ>/ns
	A_1	A_2	A_3	A_4	τ_1	τ_2	τ_3	τ_4	
Fibrinogen Crystal		0.35	0.43	0.22		0.94	2.6	5.4	2.6
BFG on steel 0.4 nmole mm^{-2}	0.02	0.55	0.33	0.10	0.24	0.65	2.0	4.8	1.5
BFG on steel 0.2 nmole mm^{-2}	0.44	0.26	0.22	0.08	0.10	0.67	1.9	4.5	1.0
BFG on steel 0.1 nmole mm^{-2}	0.45	0.28	0.21	0.06	0.12	0.65	1.8	4.3	0.87

Table 4.5. Fluorescence decay parameters for solid BFG and BFG deposited on steel in varying amounts. <τ>is the number-average lifetime.

On decreasing the amount of BFG by half once again, the population distribution, the component lifetimes and the average lifetime, and hence quantum yield, remain reasonably consistent. This consistency of quantum yield is encouraging with respect to the establishing a quantitative relationship between intrinsic fluorescence intensity and protein load, but requires further verification by lifetime measurements at lower surface protein densities.

At the surface densities used in these measurements, the BFG deposits are estimated to be of the order of 10^3 to 10^4 monolayers thick (assuming that there is uniform surface coverage, and the area occupied by a BFG molecule is of the order of 10^{-16} m^2). Therefore only a very small fraction of the protein deposit will be in direct contact with the metal surface. The efficiency with which the Trp fluorescence is quenched can be explained by energy transfer between Trp residues within the protein deposit and thence to the metal surface, resulting in quenching of the fluorescence of residues that are not in close proximity to the surface.

4.4 Conclusion

The results presented here show that the position of Trp residues within the protein structure has a considerable effect on how they interact with UV light. In the case of BSA, Trp residues are close to the surface and therefore have high quantum yields and long lifetimes. In this situation UV irradiation induces rapid photo-oxidation of Trp residues to NFK and kynurenine which, as a consequence, makes BSA unsuitable for use as a fluorescence standard in the intrinsic detection of proteinaceous contamination on surgical instruments. The analysis of the serum proteins BFG and γ-globulins and 'the physicists' protein' lysozyme show markedly different results. The majority of Trp residues in these proteins are quenched, with short lifetime so they are less likely to react following UV irradiation, however, this does not remove the possibility of bleaching of these residues. Despite the majority of residues having shortened lifetimes, significant bleaching of Trp fluorescence was observed suggesting that the environment of these residues is conducive to bleaching rather than oxidation. This is corroborated by the observation that photo-ionisation of Trp at wavelengths below 300 nm can lead to the production of a Trp radical which can then go on to react, bleaching Trp emission. It is proposed that in the case of solid BFG, lysozyme and γ-globulins, photo-ionisation is the dominant process governing the bleaching of Trp emission. To determine if such a process was present in those proteins which have evolved to resist photo-oxidation, eye lens crystallins

were analysed. Analysis of α- and γ-crystallins yielded similar results to those observed for the serum proteins and lysozyme, suggesting once again that photo-ionisation is the dominant process in the destruction of Trp residues in crystalline proteins.

Analysis of these proteins has highlighted BFG, lysozyme and γ-globulins in particular as strong candidates as standards in the intrinsic detection of protein and the analysis of BFG on a stainless steel surface has strengthened hypothesis that intrinsic detection of protein adsorbed on to stainless steel is possible. Although fluorescence is significantly quenched following adsorption onto the stainless steel surface, protein amounts as low as 200 fmole mm^{-2} of BFG could be detected using prototype equipment. Additionally, quenching of Trp residues upon adsorption may be beneficial as increased quenching implies increased photo-chemical stability. Moreover, analysis of the fluorescence lifetimes of BFG on stainless steel suggests that variation in the amount of protein on the surface should not significantly affect the lifetimes recorded. This could mean that both steady state and time resolved measurements could be used in combination to detect and quantify residual protein remaining on cleaned surgical instruments.

4.5 Future Work

In light of the research conducted so far, it has been realised that much more can be done to strengthen the outcomes already established. Further analysis of BFG, γ-globulins and lysozyme in the form of time based irradiation at 290 nm would determine at which point irradiation become deleterious and gives insight into the irradiation times that each protein could withstand. On a similar note, a power series could reveal at which point incident light is weak enough to avoid significant bleaching but still give an appropriate detection limit. Comprehensive analysis of protein on steel is required to determine the detection limit of intrinsic fluorescence for BFG, γ-globulins and lysozyme. This will allow for definitive identification of the most suitable candidate as a standard for subsequent studies. Combined with further time-resolved analysis on steel down to lower concentrations, to determine the reliability of lifetime measurements following adsorption onto steel, a highly precise and sensitive technique could be developed for use in sterile services departments.

4.6 References

1. J. T. Vivian and P. R. Callis, *Biophys. J.*, 2001, **80**, 2093–2109.

2. F. T. S. Chan, G. S. Kaminski Schierle, J. R. Kumita, C. W. Bertoncini, C. M. Dobson and C. F. Kaminski, *Analyst*, 2013, **138**, 2156–2162.

3. J. Chen, D. Toptygin, L. Brand and J. King, *Biochemistry*, 2008, **47**, 10705–10721.

4. M. J. Davies and R. J. Truscott, *J. Photochem. Photobiol. B.*, 2001, **63**, 114–125.

5. D. M. Gakamsky, B. Dhillon, J. Babraj, M. Shelton and S. D. Smith, *J. R. Soc. Interface*, 2011, **8**, 1616–1621.

6. P. Dolashka, I. Dimov, N. Genov, I. Svendsen, K. S. Wilson and C. Betzel, *Biochim. Biophys. Acta*, 1992, **1118**, 303–312.

7. C. M. Pande and J. Jachowicz, *J. Soc. Cosmet. Chem.*, 1993, **122**, 109–122.

8. R. S. Davidson, *J. Photochem. Photobiol. B Biol.*, 1996, **33**, 3–25.

9. V. M. Longo, a da Silva Pinheiro, J. R. Sambrano, J. a M. Agnelli, E. Longo and J. a Varela, *Int. J. Cosmet. Sci.*, 2013, **35**, 539–545.

10. K. Schafer and H. Hocker, *J. Soc. Dye. Colour.*, 1997, **113**, 350–355.

11. D. Creed, *Photochem. Photobiol.*, 1984, **39**, 537–562.

12. G. J. Smith, *J. Photochem. Photobiol. B Biol.*, 1995, **27**, 187–198.

13. M. Sun and S. Zigman, *Photochem. Photobiol.*, 1979, **29**, 893–897.

14. L. O. Reid, E. A. Roman, A. H. Thomas, and M. L. Dántola, *Biochemistry*, 2016, **55**, 4777-4786

15. T. M. Dreaden Kasson, S. Rexroth and B. A. Barry, *PLoS One*, 2012, **7**, DOI:10.1371/journal.pone.0042220

16. T. M. Dreaden, J. Chen, S. Rexroth and B. A. Barry, *J. Biol. Chem.*, 2011, **286**, 22632–22641.

17. G. M. Stutchbury and R. J. W. Truscott, *Exp. Eye Res.*, 1993, **57**, 149–155.

18. S. Fukuzaki, H. Urano and K. Nagata, *J. Ferment. Bioeng.*, 1995, **80**, 6–11.

19. A. Vallee, V. Humblot and C.-M. Pradier, *Acc. Chem. Res.*, 2010, **43**, 1297–1306.

20. M. Rabe, D. Verdes and S. Seeger, *Adv. Colloid Interface Sci.*, 2011, **162**, 87–106.

21. W. Norde, F. Macritchie, G. Nowicka and J. Lyklema, *J. Colloid Interface Sci.*, 1986, **112**, 447–456.

22. C. Poleunis, C. Rubio, C. Compre and P. Bertrand, *Surf. Interface Anal.*, 2002, **34**, 55–58.

23. 1 Y. S. Hedberg, M. S. Killian, E. Blomberg, S. Virtanen, P. Schmuki and I. Odnevall Wallinder, *Langmuir*, 2012, **28**, 16306–16317.

24. J. Dillon, R.-H. Wang and S. J. Atherton, *Photochem. Photobiol.*, 1990, **52**, 849–854.

25. R. E. Giménez, V. Vargová, V. Rey, M. B. E. Turbay, I. Abatedaga, F. E. Morán Vieyra, V. I. Paz Zanini, J. H. Mecchia Ortiz, N. E. Katz, V. Ostatná and C. D. Borsarelli, *Free Radic. Biol. Med.*, 2016, **94**, 99–109.

26. H. H. Kim, Y. M. Lee, J. K. Suh and N. W. Song, *Photochem. Photobiol. Sci.*, 2007, **6**, 171–180.

27. T. B. Truong, *J. Phys. Chem.*, 1980, **84**, 964–970.

28. M. Bazin, L. K. Patterson and R. Santus, *J. Phys. Chem*, 1983, **87**, 189–190.

29. J. F. Baugher and L. I. Grossweiner, *J. Phys. Chem.*, 1977, **81**, 1349-1354

30. L. O. Reid, E. A. Roman, A. H. Thomas, and M. L. Dántola, *Biochemistry*, 2016, **55**, 4777-4786

Chapter 5. Investigation of the Fluorescence Characteristics of Porcine Ocular Media and the Induction of Cataract via Photo-oxidation

5.1 Introduction

Cataract is the leading cause of blindness worldwide. Currently, 90% of cases occur in developing countries; however, with the ageing Western population, the prevalence of cataract is set to increase[1-3]. Current methods of treatment are invasive, involving surgery to replace the affected lens with an intraocular implant[4], and recovery time is in the region of weeks. Moreover, clinical diagnosis is performed visually using a slit lamp and the Lens Opacities Classification System or the Age-Related Eye Disease Study as references to determine the type and severity of the cataract[5]. This not only leads to a subjective diagnosis but the cataract must be visible and impairing vision before it can be diagnosed; therefore, it would be advantageous to develop a more reliable and quantitative method of diagnosis and a less invasive method of treatment. The fluorescence of the crystalline lens was first noted by Regnauld in 1858 and a study by Hosoya in 1929 noted that the fluorescence observed in the lenses of elderly patients was red-shifted compared to lenses from younger patients[6]. Many studies have noted changes in the fluorescence of lenses with age, which correspond with the fluorescence observed in lenses with cataract. The observed red-shift in fluorescence can be attributed to the build-up of yellow/brown chromophores and their derivatives within the proteins and solution of the lens[7]. These changes can be observed long before any impairment of vision and studies suggest that fluorescence detection could be a powerful tool in the early diagnosis of cataract[8,9]. Additionally, identification and characterisation of the chromophores involved could lead to a non-invasive, light-based method for cataract treatment. This chapter reports the results of experiments carried out at Edinburgh Biosciences in Livingston (the industrial partner in the PhD CASE studentship) to investigate the fluorescence characteristics of healthy lenses and to explore the feasibility of creating and analysing cataract in vitro.

5.1.1 Structure of the Eye and Types of Cataract

Apart from focusing and detecting light, the components of the eye, namely the cornea, lens and vitreous humour, protect the retina from ultraviolet (UV) damage.

The cornea plays multiple roles: providing structural stability, protection of the inner components and the majority of the eye's refractive power[10,11]. It is mainly composed of a precisely arranged 3-dimensional matrix of collagen, which determines its shape and transparency to visible light. The principal functions of the lens are to fine tune the focus of light from the cornea onto the retina and to block the transmission of UVA light (315-400 nm) to the retina. The lens is largely formed of transparent cells called lens fibres which have a highly structured cytoskeleton and, when mature, contain no organelles[12,13]. These features are important factors in maintaining lens transparency. Lens fibres are tightly and precisely packed with crystallin proteins which increase the refractive index of the lens without compromising transparency. The lens protects the retina from UV light due to the presence of protective chromophores (PChs) which, upon excitation, deactivate via innocuous pathways, such as vibrational relaxations and intramolecular proton transfer[14], thus reducing the likelihood of photochemical damage.

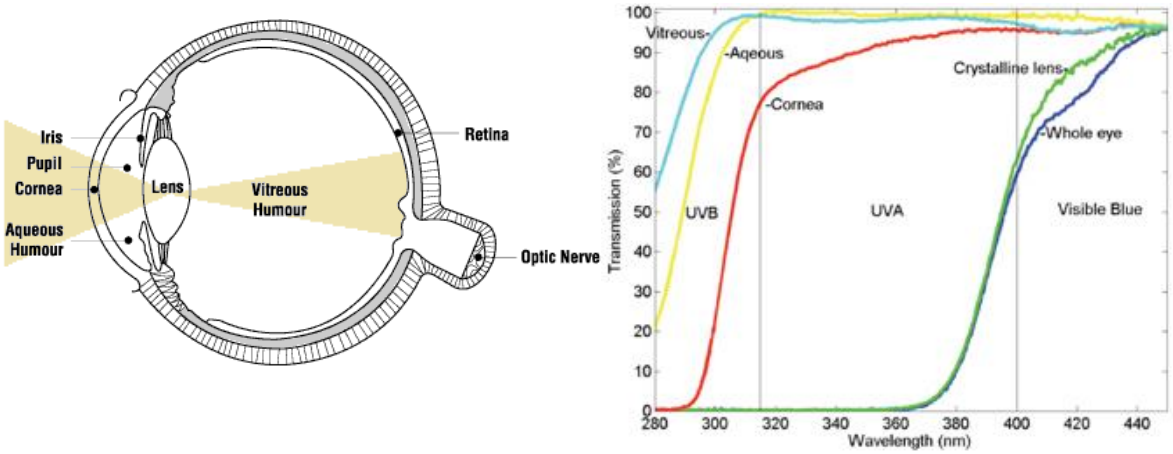

Figure 5.1a. Left: Diagram of the eye showing the light path through the optical components to the retina, Right: Transmission spectra of the ocular media[15]

Figure 5.1a (left) shows the structure of the eye and the transmission spectra of the ocular media (right), confirming that the cornea filters out the majority of UVB light (280-315 nm). As expected from the transmission characteristics, the lens absorbs the majority of light below 380 nm. The main chromophores within the lens which are responsible for absorbing harmful wavelengths are known as kynurenine-related tryptophan derivatives (KRTDs) and the most abundant are kynurenine (KN), 3-hydroxykynurenine (3-OHKN), 3-hydroxykynurenine O-β-D-glucoside (3OHKG), 4-(2-amino-3-hydroxyphenyl)-4-oxobutanoic acid glycoside (AHBG), and glutathionyl-3-hydroxykynurenine glycoside (GSH-3OHKG)[7,14, 16,17]. These molecules are created in the lens via catabolism of tryptophan (Trp) that is transported to the lens via the

aqueous humour. PChs, such as KRTDs, are present in the lens to protect the retina by absorbing light in the UV and in the region of 300 nm – 400 nm; with an absorption maximum at 365 nm[14,16]. However, they are intrinsically unstable[18,3] due to the vulnerability of the so-called 'kynurenine side chain' to deamination. This deamination reaction allows covalent attachment of KRTDs such as kynurenine, 3-OHK and 3-OHKG to crystallin proteins[19], which not only disrupts the structure of the protein, leading to aggregation but covalent attachment of 3-OHKG has been shown to account for at least 50% of age-related lens yellowing[20]. Some filters such as n-formylkynurenine (NFK) and kynurenine are photosensitisers and the gradual accumulation of these filters and their derivatives within the lens can lead to sensitisation of tryptophan within lens proteins to photo-oxidation[18]. This, in turn, leads to the accumulation of photo-oxidation products such as NFK, kynurenine and 3-OHK within the protein structure which can go on to react, further disrupting crystallin structure. Furthermore, NFK, kynurenine and 3-OHK are yellow compounds[21] and their accumulation within the lens and lens proteins contributes to the overall yellowing of the lens with age.

The effects of the aforementioned processes are concentrated by the extremely low metabolism within the lens and the fact that crystallin proteins cannot be replaced and must therefore last a lifetime[22]. This accumulation of damage to crystallins and disruption of the lens environment leads predominantly to photo-yellowing and protein aggregation and is clearly illustrated in Figure 5.1b (left). Lenses ranging in age from 6 month to 91 years show how lens damage amasses to yellowing and opacity of the lens eventually resulting in complete inhibition of light transmission through the lens i.e. cataract. This is corroborated in Figure 5.1b (right) which shows how the transmission characteristics of the lens change with age; at birth light above 300 nm is transmitted with light above 400 nm transmitted with 100% efficiency; however, by 25 years only light above 400 nm is transmitted and at only 80% efficiency, indicating the accumulation of KRTDs, by 82 years transmission above 400 nm is at 30%, indicating the accumulation of protein damage, aggregation and ultimately cataract.

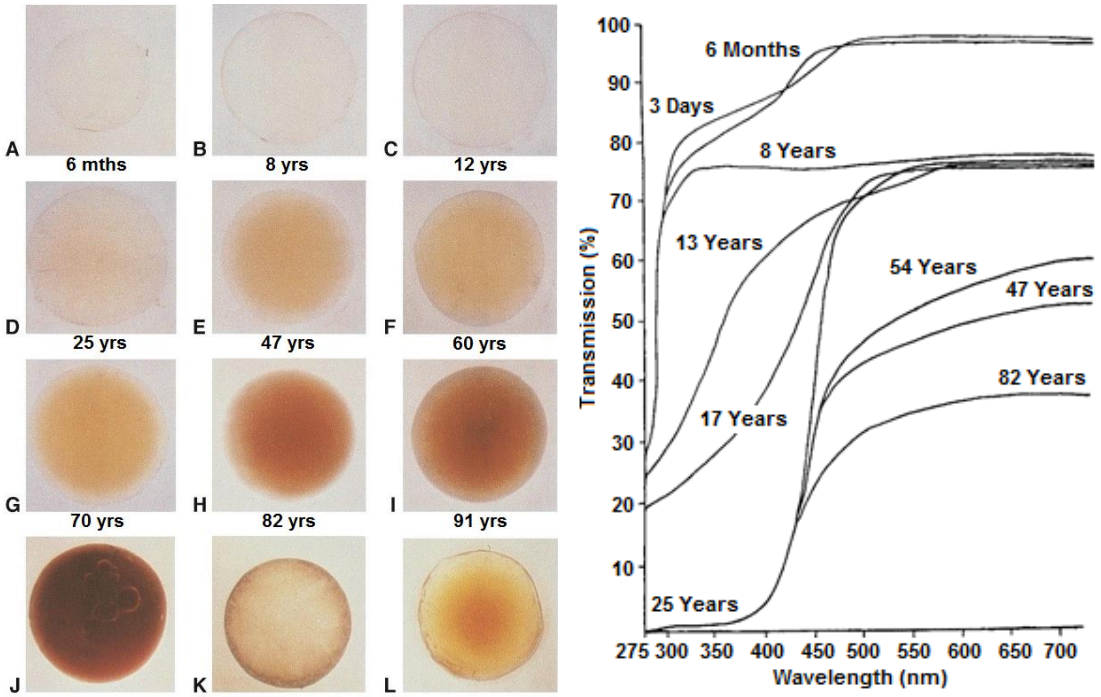

Figure 5.1b. Left - progression of photo-yellowing of the lens with age, J shows a brown nuclear cataract, K a cortical cataract and L a mixed nuclear and cortical cataract and Right - transmission spectral characteristics of the lens with age[17].

There are two main types of cataract: nuclear and cortical[23,24]. Cortical cataracts are characterised by opacity of the collagen fibres of the lens, presenting as a radial opacity of the outer layers of the lens (Figure 5.1b left, image K) and are associated with a high lifetime exposure to UV radiation[13]. Nuclear cataracts (Figure 5.1b left, image J) are characterised by hardening, yellowing and opacity of the centre of the lens and, as well as the processes mentioned above, are linked with a decrease in glutathione concentration in the lens nucleus with age. Glutathione intercepts reactive precursors to UV filters such as NFK, and as its concentration falls, nuclear proteins become more susceptible to oxidation[3]. Characterisation of the species giving rise to age-related pigmentation and fluorescence of the lens at different stages of progression and in different types of cataract, is the first step in establishing whether or not fluorescence can be used to quantitatively measure the progression of cataract and whether or not diagnosis of different cataracts is possible.

5.1.2 Current Methods of Cataract Diagnosis and Treatment

As mentioned previously, current methods for cataract diagnosis and treatment are not ideal. Diagnosis is subjective, due to the use of a visual grading system coupled with slit-lamp images of the lens in question. A more accurate method of diagnosis comes in the form of the Pentacam; a 360° rotating non-contact Scheimpflug imaging

system with a lens densitometry function[5]. Repeatability is high for the Pentacam and good correlation has been shown with the LOCS grading system[25]. Although the instrument has been used clinically, its use is rare compared to slit-lamp diagnosis. Although cataract surgery carries a low risk, the procedure is invasive and complications can lead to partial or total blindness. Treatment of cataract in the form of cataract surgery involves incision of the cornea and either manual removal of the intact lens or sonication followed by aspiration of the lens contents, followed by implantation of an artificial lens[2]. Consequently, there is significant trauma and discomfort, with healing times in the region of weeks. This has led to recent research into the action of molecular chaperones on crystallin aggregates, which has shown that administering the molecular chaperone lanosterol, as well as related compounds, in the form of eye drops can significantly improve lens clarity in cataractous lenses. This was shown via comparison of photographs of lenses before and after administration of lanosterol both *in vitro* and *in vivo*. Treated lenses showed a significant improvement in clarity and decrease in scattering. The dispersal of protein aggregates was further supported by monitoring the decrease in fluorescence from α-crystallin protein aggregates following administration[26]. In another study[27], a class of related sterols, including lanosterol, were screened for binding activity with α-crystallin. It was found that, although lanosterol showed some cataract dispersal, administration of a molecule known as 'Compound 29' improved the solubility of α-crystallins by 63%. Additionally, its presence before the initiation of aggregates in solution suppressed aggregate formation. Although these results are promising, research is in the early stages and far from clinical trials. More recently, a new surgical method has been trialled in human infants and utilises the patient's own lens epithelial stem cells (LECs). The surgery improves on current methods by significantly reducing the size of the incision made in the lens capsule to gain access to the contents. Additionally, the incision was moved to the periphery and lens contents removed to leave a layer of LECs inside a predominantly intact capsule. This allowed functional regeneration of the lens and visual axis transparency in more than 95% of cataractous eyes in infants[28]. Whether or not this treatment is viable in adult lenses is yet to be confirmed.

5.1.3 Previous Studies of Lens and Cataract Fluorescence and Photobleaching

Countless studies have set out to understand the processes behind the formation of cataract; however, as is evident from the literature, there is a tangled web of genetics, environment, disease and oxidative stress mediating the process. A recent study[9], conducted by our industrial collaborator, investigated cataract-related changes in the emission spectrum of the endogenous fluorophore tryptophan (trp), with the aim of developing a method for early diagnosis of the condition. As shown in Figure 5.1c (left), excitation of lenses at the red-edge of the trp absorption band, resulted in emission that was dominated by trp fluorescence, at 350 nm, from the lens proteins. With increasing age, and pigmentation, of the lens, the emission was found to become distorted; the trp emission at 350 nm decreased and long-wavelength emission at 450 nm increased.

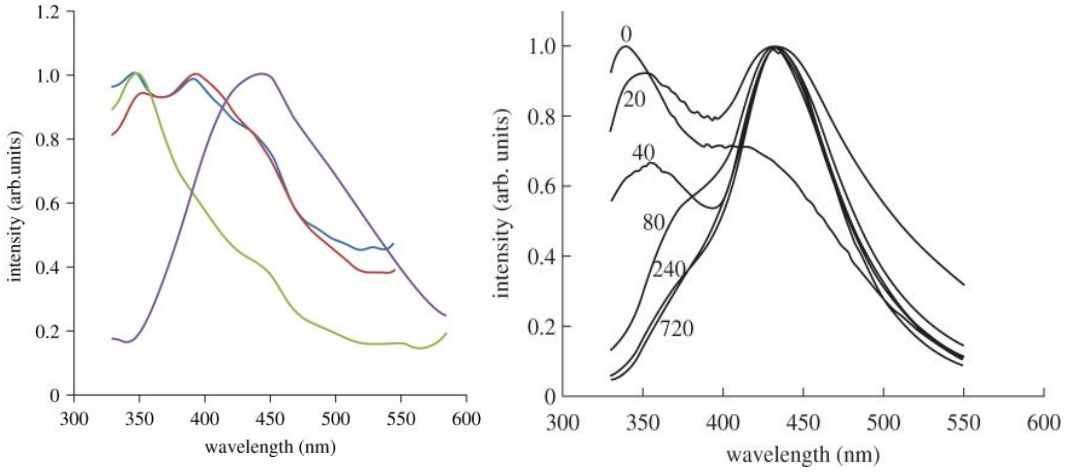

Figure 5.1c. Left - Fluorescence emission from human lenses; green: 66 years, blue: 79 years, red: 60 years, purple: 80 years, λ_{ex} = 317 nm and Right - Monitoring of the irradiation of a porcine lens at 310 nm for 720 minutes[9]. Emission spectra measured at an excitation wavelength of 317 nm

To determine if the same change in fluorescence signature of the lens could be created by UV irradiation in the laboratory, porcine lenses were irradiated at 310 nm, which is on the red-edge of tryptophan absorption. The fluorescence, excited at 317 nm, to allow excitation of both Trp and the photo-products, was then monitored, over the course of 720 minutes. The spectral changes were in keeping with those observed in ageing lenses (Figure 5.1c left); the Trp emission decreasing in intensity, while long-wavelength emission (435 nm) increased. The long-wavelength emission was attributed to the Trp photo-products NFK and 3-OHK. The "F-parameter" was

suggested as a diagnostic ratio of Trp and non-Trp emission intensity, and was shown to be sensitive to UV-induced photo-damage. Although this study shows that the photo-oxidation of Trp can be induced *in vitro*, it is only one of an extensive list of processes implicated in the progression of cataract. Moreover, given the complexity of the lens, any number of photochemical reactions could be induced under such conditions.

In the context of developing non-invasive methods of treating cataracts, Kessel *et al*[29,30] carried out experiments to determine if photo-bleaching could be used to improve transmission in human lenses showing yellow/brown pigmentation. In one study[29], it was observed that irradiation of yellowed donor lenses, at bleaching wavelengths of 375, 405, 445, 457 and 473 nm, resulted in an increase in measured transmission in the region 450 nm – 490 nm, where age-related transmission loss is most pronounced. This effect was most prominent when irradiating with a bleaching wavelength of 420 nm and least prominent at 375 nm, although no visible change in transparency or yellowing was observed. Although transmission was shown to improve following irradiation, a suitable reference for all studies was not reported, nor was variation in transmission between 'healthy' clear/colourless lenses. In another study by the same group, irradiation at 445 nm resulted in improved transmission of visible light in the region 420 – 600 nm; however, scattering measurements showed no significant change[30]. This suggests that, although chromophores absorbing at 445 nm were bleached, scattering bodies such as protein aggregates remained intact. Analysis of lens homogenates before and after bleaching showed a decrease in fluorescence at 385 nm (λ_{ex} = 335 nm) after bleaching, attributed to argpyrimidine and pentosidine-like advanced glycation end products (AGEs), and at 440 nm (λ_{ex} = 370 nm), attributed to other, unidentified AGEs. However, analysis of samples via HPLC and ELISA, before and after bleaching, showed no decrease in the concentration of the AGEs argpyrimidine, pentosidine, carboxymethyllysine and hydroimidazolone. It seems likely that 440-nm emitting species observed by Kessel *et al* are KRTDs. However, as KRTDs, as well as AGEs, do not absorb above 400 nm, irradiation at 445 nm and 420 nm would not result in photo-bleaching. It may be that effects of thermal decomposition are being observed and/or that a group of unknown lens chromophores are absorbing at these wavelengths. As is evident, further research is necessary to determine the chromophores involved in yellowing and decreased transmission of the lens.

5.2 Materials and Methods

5.2.1 Biological samples

Intact porcine eyes were acquired weekly (six at a time) from Hall's abattoir in Broxburn, within 3 hours of slaughter. Porcine lenses were used to ensure studies were in keeping with those carried out previously by our industrial partners at Edinburgh Bioscience Ltd. and because porcine eyes were readily available nearby, ensuring a fresh sample. The age of the pigs from which the eyes were removed ranged from 6-8 months. Upon delivery, the eyes were either stripped of any surrounding muscle tissue and stored whole or dissected to remove components of interest. Samples were stored in pH7 PBS buffer solution containing 100mg/ml Penstrep to prevent bacterial growth. PBS tablets and Penstrep solution were acquired from Fisher Scientific.

5.2.2 Transmission measurements

Transmission measurements were carried out using the excitation arm of a fluorescence spectrometer (Edinburgh Instruments model FS920) as the light source and an optical-fibre-coupled spectrometer (Ocean Optics model STS-UV), with associated software, for detection. Transmittance, through the centre of the lens under investigation, was measured, relative to a blank consisting of and a cuvette of storage solution, over the range 290 nm to 660 nm, in 10 nm increments.

5.2.3 Steady state fluorescence analysis

Experiments at Edinburgh Biosciences

Steady-state fluorescence spectra were recorded using a modified Edinburgh Instruments FS920 spectrofluorometer in conjunction with F920 software. (The sample chamber had been removed to allow the presentation of non-standard samples.) The excitation source was a Xe900 continuous ozone-free Xenon lamp coupled with a TMS300-X monochromator. Fluorescence from the sample was collected at a right angles to the excitation light[31]. The excitation and detection areas were define by matching the focal point of the source with the focal point of the collection optics of the emission arm. The size of the excitation area was 1x4 mm,

positioned centrally on the sample. Spectra were acquired with excitation and emission bandwidths of 2 nm.

Note: Due to damage to the monochromator, a dip was observed at 460 nm as an artefact in emission spectra.

Experiments at the University of Edinburgh

Steady-state fluorescence spectra were acquired using a Fluoromax-P spectrofluorometer in conjunction with FluorEssence™ software v.3.5. The excitation source was a 150W continuous ozone-free Xenon lamp, directed to the sample chamber via a monochromator. Fluorescence from the sample was collected at right angles to the excitation light. Front surface measurements were made using optical fibre bundles coupled to the excitation and emission arms of the spectrofluorometer and positioned as shown in Chapter 3, section 3.2.6. Spectra were acquired with 2 nm excitation and emission bandpass, or 5 nm bandpass when using the optical fibres.

The tissue sample was submerged in PBS/Penstrep solution in disposable PMMA macro or semi-micro cuvettes.

5.2.4 Irradiation and bleaching of samples

Samples were irradiated to produce Trp photoproducts at 310nm, in keeping with experiments carried out previously. Bleaching of chromophores was carried out at the following wavelengths: 360 nm, 405 nm, 420 nm and 470 nm, in accordance with bleaching measurements carried out by collaborators. Irradiation and bleaching was carried out using the excitation arm of the FS920 as the light source. The slit width was set to 5 nm giving an irradiation/bleaching area of 4x3 mm. All samples presented here were irradiated for 5 hours and bleached for 2 hours, with the sample in a fixed position throughout.

Please see Appendix 5.1 for details on how variation in lens size was taken into account during this study.

5.3 Results and Discussion

5.3.1 Transmission of Ocular Media

Initial measurements were concerned with the absorption and transmission characteristics of the ocular media, namely the vitreous humour, lens, cornea and an intact eye, to determine how each component responds *post mortem*. Figure 5.3a shows that the vitreous humour and lens have transmission characteristics which are comparable to those reported in the literature, both in spectral shape and intensity, suggesting that the lens and vitreous humour are resistant to *post mortem* changes. This, however, was not the case for the cornea which can begin to become cloudy within hours following death[32]. These changes resulted in significantly reduced corneal transmission with an altered spectral shape compared with the literature. Consequently, the transmission of the intact eye was similarly affected. Although the progression of corneal cloudiness *post mortem* is rapid, thus preventing analysis of whole eyes, *in vivo* experiments would not face this obstacle. Therefore, fluorescence experiments were carried out on extracted lenses. Figure 5.3b shows the penetration of light into the lens as a function of wavelength. A single lens was

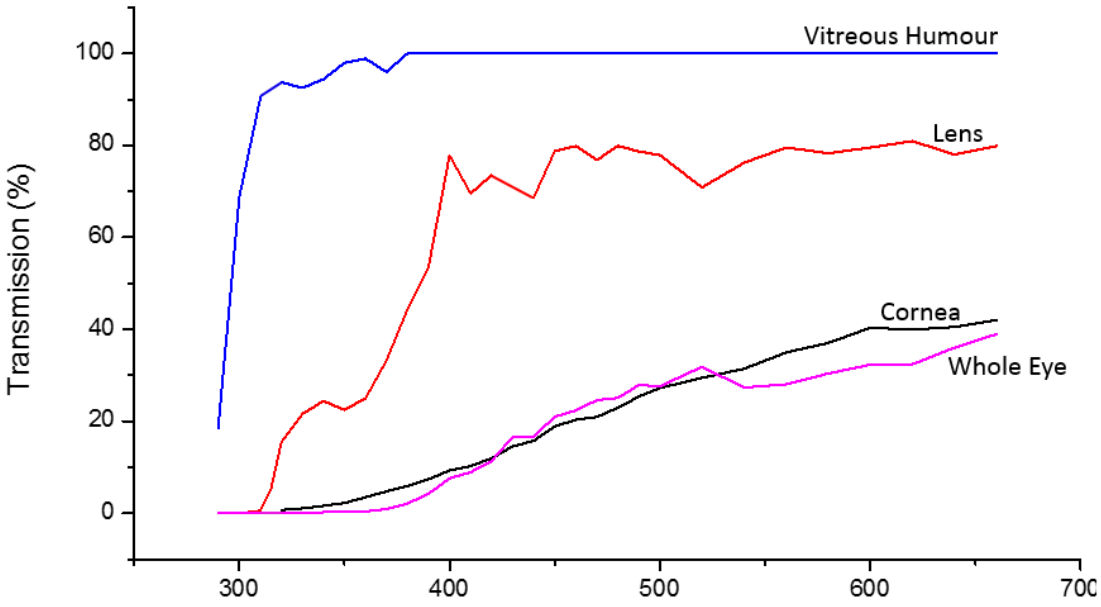

Figure 5.3a. Transmission of porcine ocular media (all samples 24 hours old).

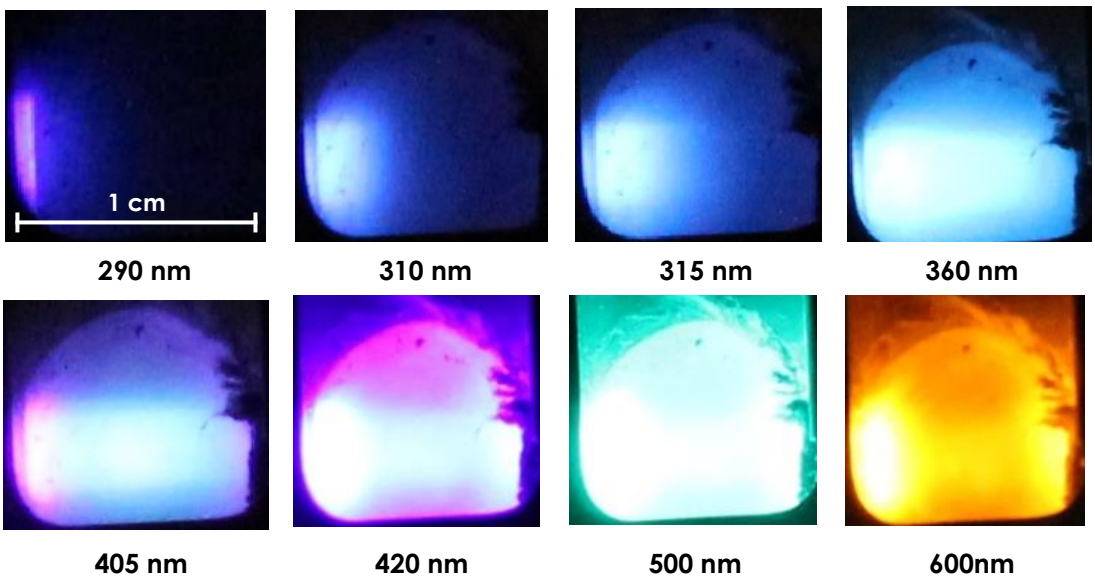

Figure 5.3b Penetration of light into an extracted lens as a function of incident wavelength

placed into a cuvette and submerged in PenStrep solution and placed into the cuvette holder in the set-up described in section 5.2.3. A digital camera was mounted perpendicular to the excitation light and a photograph taken at each wavelength described in Figure 5.3b. Evidently, light below 320 nm is strongly absorbed by the first few millimetres of the lens. This correlates with the absorption characteristics of the species present in the lens (e.g tryptophan and KRTDs) which have strong absorption bands in the UV. As wavelength increases, light penetrates further into the lens, paralleling the transmission curve for the lens shown in Figure 5.3a.

5.3.2 Fluorescence Characteristics of Extracted Porcine Lenses and Other Ocular Components

Initially, the fluorescence characteristics of a healthy eye were determined by producing an excitation-emission matrix (EEM) of each of the cornea, lens and vitreous humour, to determine the peak excitation and emission wavelengths in each case. For clarity, emission spectra are shown for each case for excitation at only two wavelengths, 290 nm and 360 nm (Figure 5.3c). 290 nm excitation selectively excites tryptophan, whereas 360 nm was used to selectively excite PChs. (For more detail on the fluorescence characteristics of the cornea and vitreous humour see Appendix 5.2).

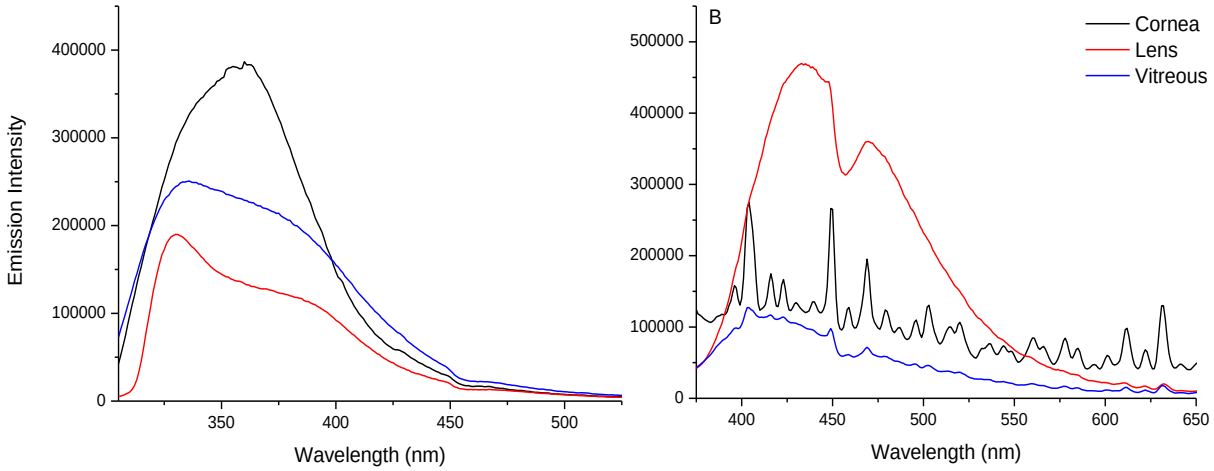

Figure 5.3c. Emission spectra of the cornea (black), lens (red) and vitreous humour (blue) at excitation wavelengths of 290 nm (left) and 360 nm (right)

When excited at 290 nm each component showed intense emission in the region 300 – 450 nm corresponding to the range of emission wavelengths observed from tryptophan in proteins. Due to the high protein content of each component it was expected to see strong tryptophan emission; however, a shoulder is also seen, beginning at roughly 350 nm, for the lens and vitreous humour. As is indicated in the literature, this shoulder can be attributed to the presence of fluorescent PChs in these structures. Upon excitation at 360 nm, emission was seen at 435 nm and 420 nm, for the lens and the vitreous humour, respectively. Observation of this long wavelength emission is consistent with the presence of PChs in the lens and, as the lens capsule is permeable to these chromophores, the vitrous humour. As the lens capsule is selectively permeable[33] depending on the molecule in question, it is suggested that the difference in emission maxima between the lens and vitrous humour is due to a different composition of chromophores between the two. The noisy spectrum produced as a result of exciting the cornea at 360 nm can be explained by the intense scattering produced at this excitation wavelength, as the cornea is essentially opaque to wavelengths above 320 nm.

The EEM in Figure 5.3d shows the emission intensity distribution for a healthy lens, with emission intensity from the fluorescent PChs of the lens higher than that for tryptophan. Although tryptophan emission intensity was consistently lower than that of the PChs, there was a large variation in the emission intensities observed for each lens and, for spectra excited at 290 nm, a large variation in spectral shape. Figure 5.3e shows the variation observed in both emission intensity and spectral shape between four different lenses. The difference in spectral shape was clearly seen when the samples were excited at 290 nm, as many molecules, including many PChs, absorb strongly at this wavelength. Upon excitation at 360 nm spectral shape remained constant (Figure 5.3e D); however, emission intensity varied from lens to lens. This suggests that, from lens to lens, the proportion of both Trp and PChs varies drastically.

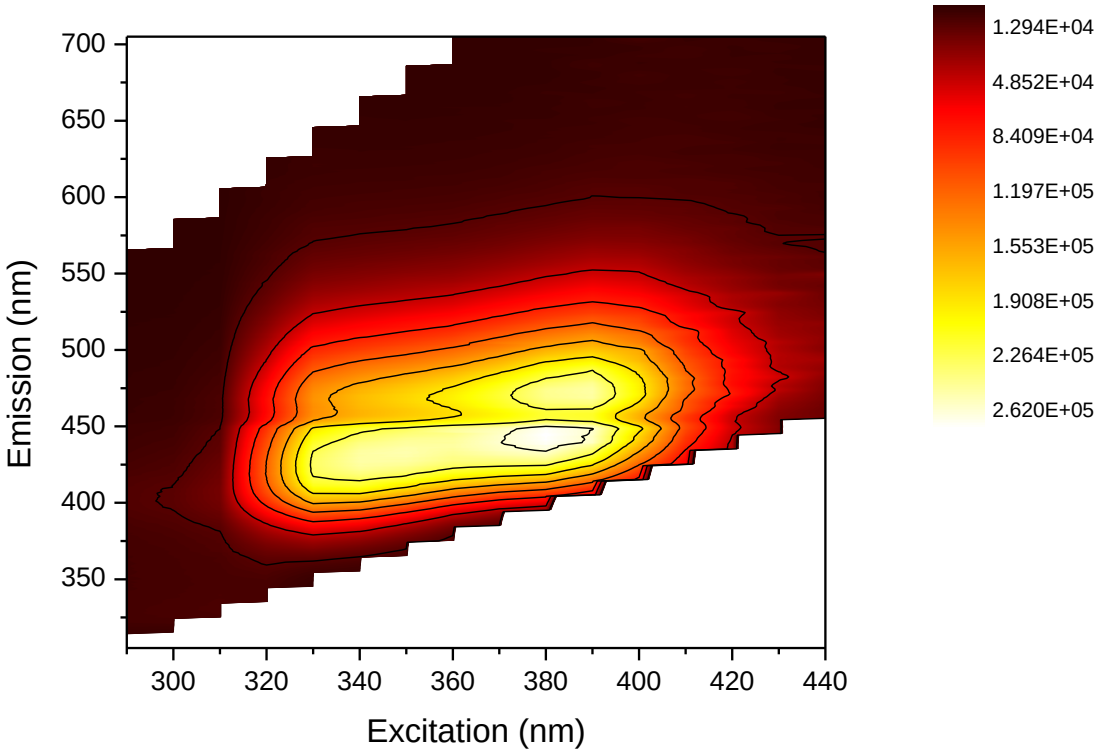

Figure 5.3d. EEM of a healthy porcine lens.

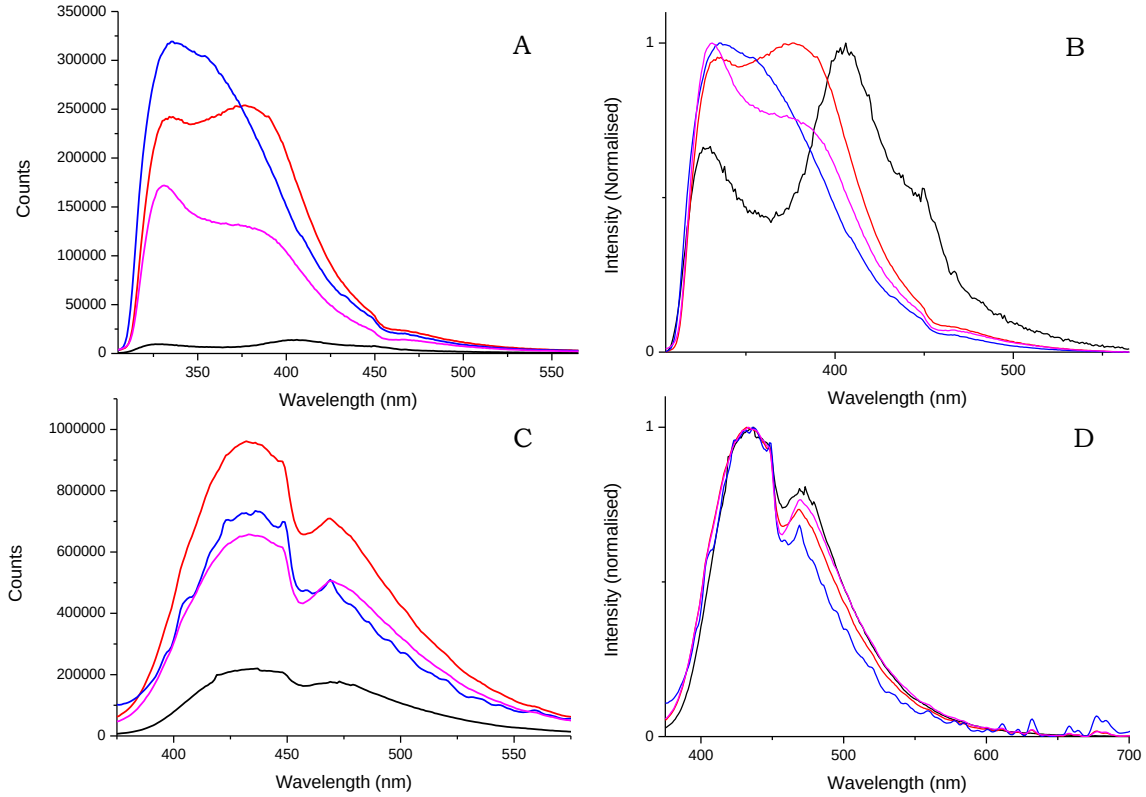

Figure 5.3e. Variation of emission intensity and spectral shape, respectively, among four lenses excited at 290 nm (A and B) and 360 nm (C and D). (Red: Lens 1, Blue: Lens 2, Pink: Lens 3, Black: Lens. 4)

The level of variation observed in young, healthy lenses is discouraging in the context of the previously reported studies by Gakamsky *et al* and Kessel *et al*, as well as the study presented here, as a reliable reference is required to determine the progression of cataract[9] and treatment[24,25]. Moreover, the proposed treatment of cataract via irradiation and bleaching of chromophores could result in the destruction of the protective, endogenous filters, therefore, removing the remaining protection present in a cataractous lens. In addition to variations in emission intensity and spectral shape at specific excitation wavelengths, emission was seen to be highly dependent on excitation wavelength (Figure 5.3f); as excitation wavelength was increased from 290 nm to 410 nm the emission wavelength shifted from 330 nm to 480 nm, indicating the presence of a multitude of fluorescent chromophores. The lens is a highly complex biological system, therefore, convoluted fluorescence characteristics are unsurprising.

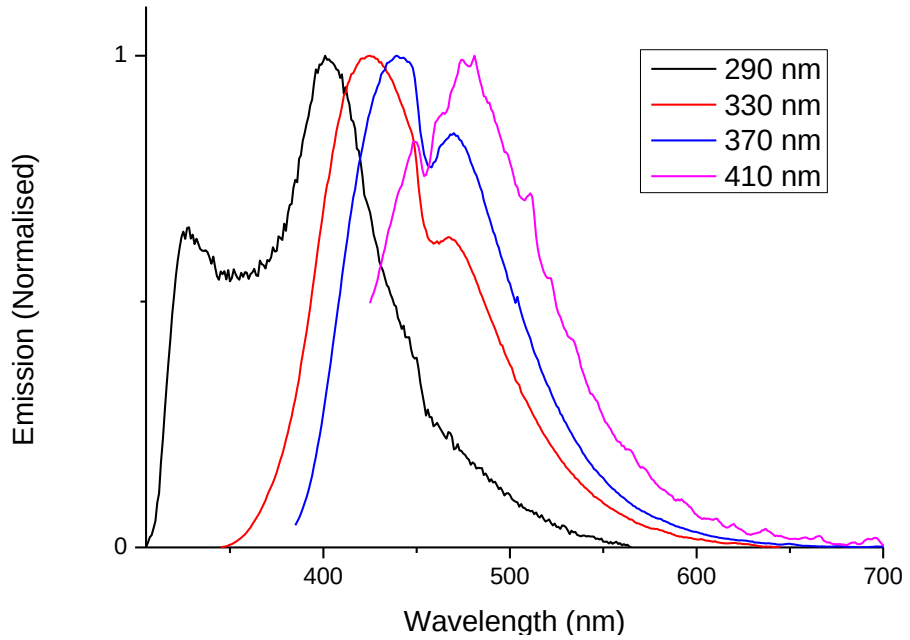

Figure 5.3f Excitation wavelength-dependent emission spectra of the lens.Spectra are normalised to the maximum intensity.

Despite these potential complicating factors, experiments continued to determine if cataract could be induced via artificial irradiation of lenses with UV light and if artificial cataract could be photo-bleached.

5.3.3 Induction and Bleaching of Cataract

To keep experiments in line with those of research partners, irradiation of the lenses was carried out at 310 nm, to attempt selective irradiation of trp. As shown in Figures 5.3g to 5.3i, irradiation resulted in a decrease in tryptophan emission intensity at 340 nm and an increase in emission intensity at 430 nm. This suggests that tryptophan was photo-oxidised into KTRDs, most likely NFK and/or kynurenine, as was obseved upon irradiation of protein crystals (See Chapter 4). In no sample, was there any evidence of emission peaks at longer wavelengths, when exciting at wavelengths above 360 nm. Additionally, no yellowing or cloudiness, which is indicative of cataract formation, was observed. Despite the observation that the species that were formed emitted mainly around 430 nm, and must, therefore, absorb predominantly below 430 nm, it was stipulated in the project plan that bleaching wavelengths should be in keeping with previous work carried out by Kessel *et al*[29], which aimed to bleach those chromophores which are related to the age-related decrease in tranmission in the visible region (450-490 nm). Hence, bleaching wavelengths of 405, 420 and 470 nm were used.

As is presented in Figure 5.3g initial irradiation of the lens at 310 nm to induce 'cataract' resulted in a 280% increase in emission intensity at 430 nm (when excited at 360 nm), corresponding to PCh emission, and a 50% decrease in emission intensity at 340 nm (when excited at 290 nm), corresponding to Trp emission. Bleaching of the 310-nm irradiated sample at 420 nm resulted in a 20 % decrease in emission intensity at 430 nm which, compared to the large increase induced by irradiation, is minimal. As 420 nm is on the very red-edge of kynurenine absorption and in no way relates to NFK absorption (See Chapter 4), and as kynurenine and NFK are the most likely photo-products produced during irradiation, the lack of effective photo-bleaching at this wavelength is unsurprising. Thermal decomposition, as a result of absorption by other chromophores at this wavelength, may also contribute to the decrease in emission intensity at 430 nm.

For a second lens (Figure 5.3h), irradiation at 310 nm produced a 195 % increase in emission intensity at 430 nm (λ_{ex} = 360 nm) and a 57% decrease in emission intensity at 340 nm (λ_{ex} = 290 nm). Following bleaching at 405 nm, a 30% decrease in emission intensity at 430 nm was observed. This suggests that bleaching at 405 nm is also inefficient. However, 405 nm is on the red edge of kynurenine absorption (Chapter 4) which may explain the slight increase in bleaching efficiency compared with bleaching at 420 nm.

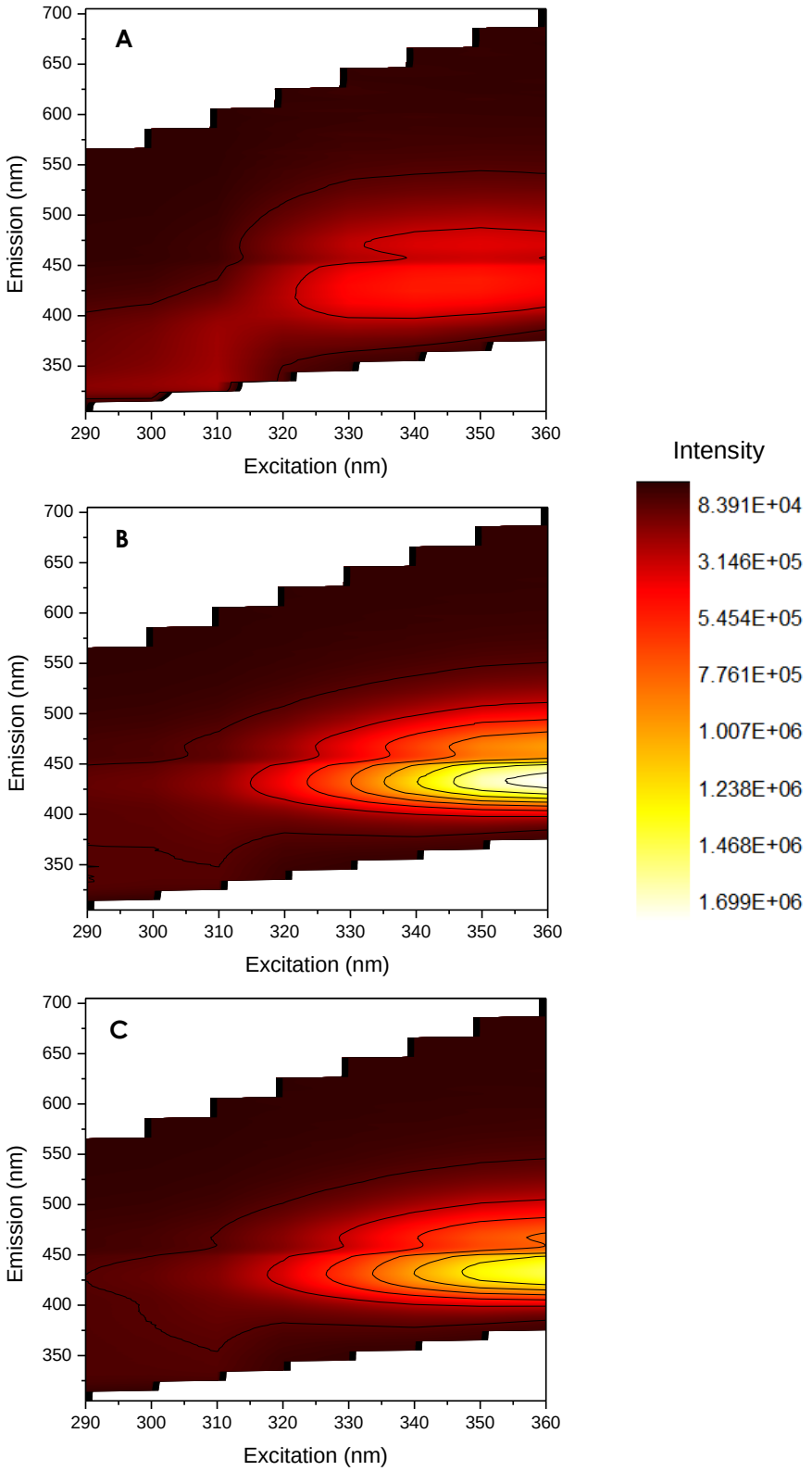

Figure 5.3g. EEM of the emission characteristics of a single lens a) before irradiation b) after irradiation at 310 nm and c) after photobleaching at 420 nm, following 310-nm irradiation.

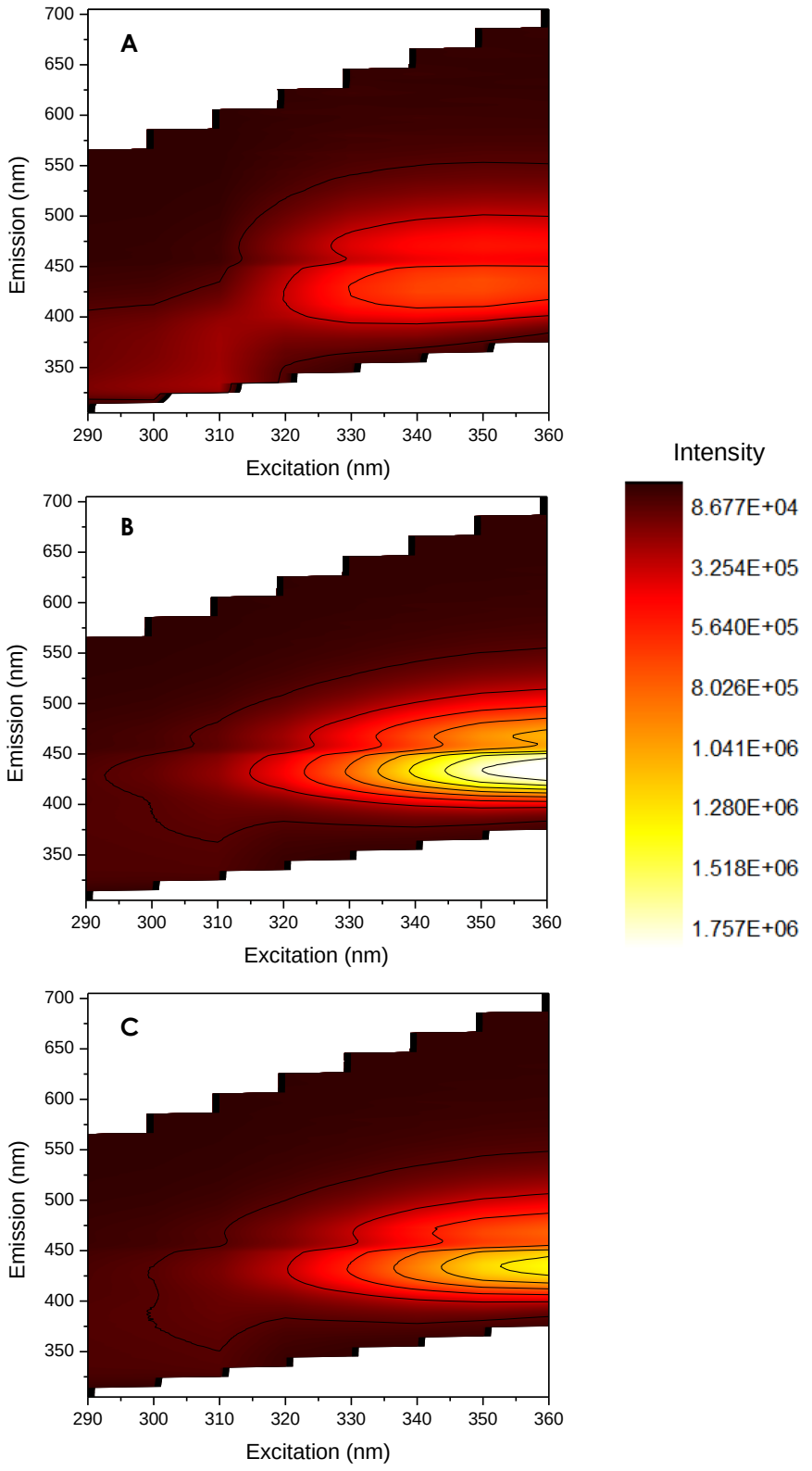

Figure 5.3h. EEM of a single lens a) before irradiation, b) after irradiation at 310 nm, and c) after photobleaching at 405 nm, following 310-nm irradtion.

Bleaching at 470 nm (data not shown) gave a negligible change in emission intensity. This can be attributed to the fact that KRTDs do not absorb light of this wavelength and that thermal contributions to fluorophore decomposition are small. These results show that cataracts equivalent to the natural, yellowed lenses analysed by Kessel *et al*[29] cannot be created artificially by UV irradiation, under the conditions of the present experiments. The 430 nm emitting photo-products of 310 nm irradiation observed here are most likely NFK and kynurenine. The bleaching of chromophores at wavelengths above 400nm, described by Kessel *et al*, can be attributed to the destruction of non-fluorescent chromophores which absorb at longer wavelengths than NFK and kynurenine. It is possible that such chromophores are present in the UV-irradiated lenses in the present experiments, but at concentrations too low to be observed visually As KRTDs absorb strongly in the region 320-380 nm it was decided to investigate photo-bleaching of UV-irradiated lenses at a wavelength in this range (Figure 5.3i). The batch of lenses used in this study presented differently, with a larger size and slight clouding of the lens capsule which may have hindered the penetration of UV light into the lens. These lenses showed a relatively small increase in 430-nm emission intensity following irradiation at 310 nm, compared those used previously. After 310-nm irradiation, the lens under study showed a 23 % increase in emission intensity at 430 nm and a 37% decrease in emission intensity at 340 nm. Following bleaching at 360 nm, the excitation maximum for KRTDs, a 44% decrease in emission intensity at 430 nm was observed. The much enhanced photo-bleaching at this wavelength is consistent with the absorption characteristics of KRTDs. It is notable that the decrease in 430-nm emission on photo-bleaching significantly exceeds the initial increase on 310-nm irradiation, indicating that bleaching at 360 nm is effective at destroying endogenous KRTDs as well as those produced artificially, further suggesting that light based methods of treatment cataract may not be suitable.

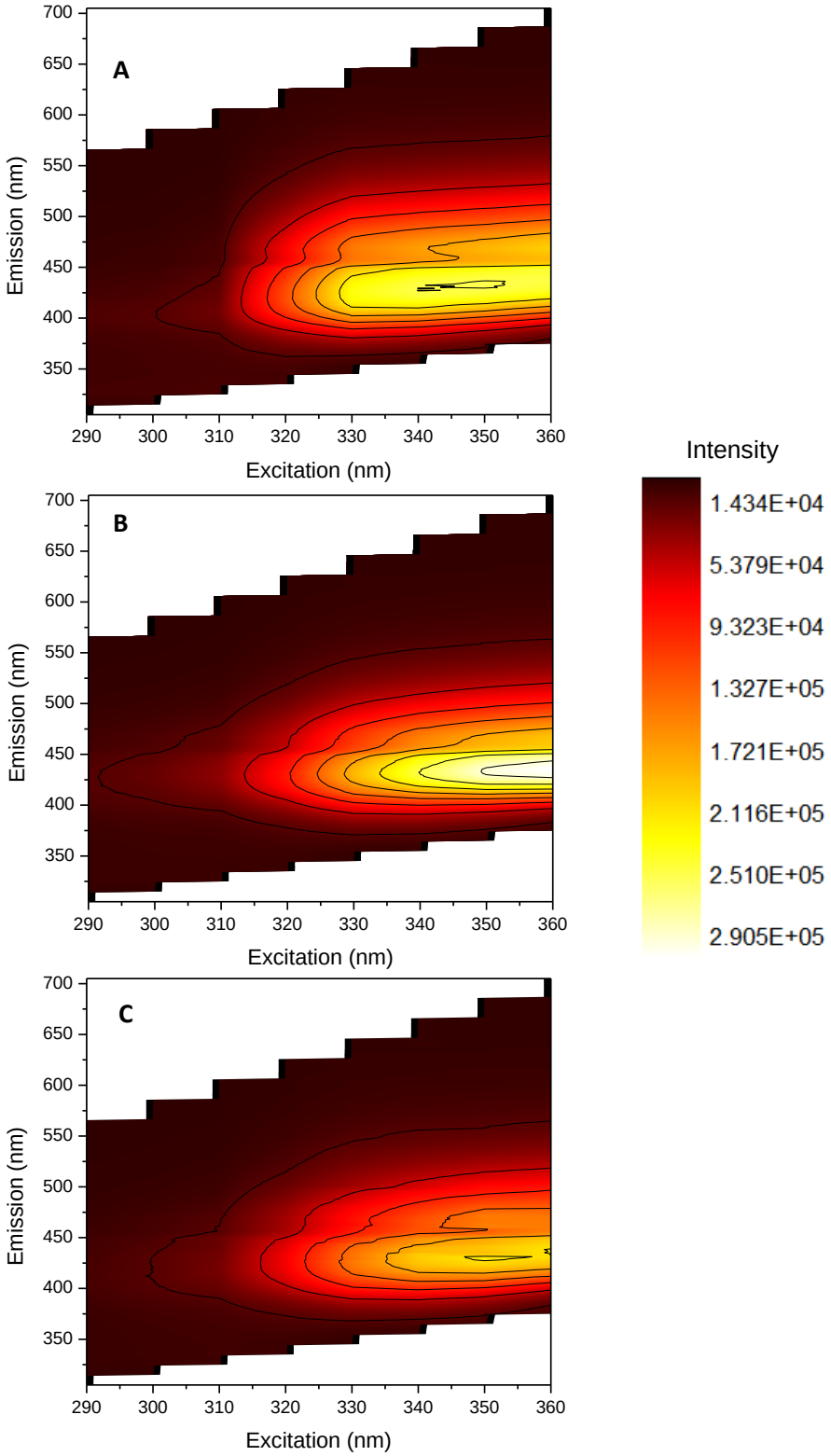

Figure 5.3i. EEM of a single lens a) before irradiation b) after irradiation at 310 nm and c) after photobleaching at 360 nm, following 310-nm irradiation.

5.4 Conclusions

The results of this study corroborate previous results that induction of long-wavelength fluorescence akin to that observed in cataractous lenses can be achieved via irradiation at 310 nm and show that, upon bleaching, the destruction of artificially created KRTDs can be observed. This is a promising result in terms of using light based methods in the early detection and monitoring of cataract, however, results suggest that light based methods of treatment may be out of reach. Upon photo-bleaching at 360 nm, the absorption maximum of KRTDs, a marked decrease in the long-wavelength fluorescence induced by 310 nm irradiation was observed. This decrease exceeded the increase observed following irradiation suggesting that endogenous KRTDs i.e. PChs were destroyed in the bleaching process. This is discouraging as, although bleaching may remove problematic KRTDs, it appears that remaining PChs may also be at risk of destruction using this method. Additionally, with such a complex system, the next steps, even just in terms of diagnosis and monitoring, will not be without complications. EEMs of healthy porcine lenses showed a complex distribution of emission from the multitude of fluorophores present. Moreover, there was significant variation in florescence intensity and spectral shape from lens to lens making it extremely difficult to find a suitable reference standard for measurements. In spite of these difficulties, the characterisation of lens fluorescence carried out in this study is a firm basis on which to build, and further research, as outlined below, could lead to successful use of fluorescence in the early detection of cataract.

5.5 Future Work

Much has been learned from this preliminary study; however, there is much more to be investigated. Firstly, as the lens used for the bleaching experiment at 360 nm differed in appearance and EEM to those analysed previously it would be pertinent to repeat this measurement to confirm the efficiency of bleaching at 360 nm. Following from this, the effect of temperature on lens fluorescence would be of interest to ensure storage in the fridge and prolonged analysis at room temperature does not affect results. Should the effect of temperature be shown to be significant, a temperature controlled set-up (at body temperature) should be adopted.

The extent of variation between fresh, healthy lenses should be further investigated by increasing the sample size and marrying fluorescence experiments with chromatographic analysis of lens contents and transmission measurements. Experiments should be carried out on intact eyes to determine if the presence of the rest of the eye will affect the results acquired from the lens. Subsequent analysis should focus on the characterisation of lenses (human as well as porcine) of varying ages, and cataractous lenses of varying severity to create a complete picture of the fluorescence characteristics of lenses at a wide range of ages and health. This may lead to the development of a non-invasive method for the diagnosis of cataract.

Regarding further investigations of artificial generation of cataract and effectiveness of photo-bleaching, it would be pertinent to attempt the creation of cataract and lens yellowing using white light rather than UV. It is possible that white light irradiation may cause other photo-chemical reactions which lead to the formation of cataract. To ensure the success and clinical relevance of subsequent measurements bleaching doses should be in accordance with the maximum permissible exposure value (the highest power density of a light source that is considered safe enough to cause no damage to the eye or skin). If successful, could lead to the development of appropriate bleaching methodology and perhaps, a light based treatment method.

5.6 References

1. E. Prokofyeva, A. Wegener and E. Zrenner, *Acta Ophthalmol.*, 2013, **91**, 395–405.

2. J. Jaggernath, P. Gogate, V. Moodley and K. S. Naidoo, *Eur. J. Ophthalmol.*, 2013, **24**, 520–526.

3. A. Korlimbinis, J. A. Aquilina and R. J. W. Truscott, *Exp. Eye Res.*, 2007, **85**, 219–225.

4. H. Lin, H. Ouyang, J. Zhu, S. Huang, Z. Liu, S. Chen, G. Cao, G. Li, R. A. J. Signer, Y. Xu, C. Chung, Y. Zhang, D. Lin, S. Patel, F. Wu, H. Cai, J. Hou, C. Wen, M. Jafari, X. Liu, L. Luo, J. Zhu, A. Qiu, R. Hou, B. Chen, J. Chen, D. Granet, C. Heichel, F. Shang, X. Li, M. Krawczyk, D. Skowronska-Krawczyk, Y. Wang, W. Shi, D. Chen, Z. Zhong, S. Zhong, L. Zhang, S. Chen, S. J. Morrison, R. L. Maas, K. Zhang and Y. Liu, *Nature*, 2016, **531**, 323–328.

5. S. Pathai, P. G. Shiels, S. D. Lawn, C. Cook and C. Gilbert, *Ageing Res. Rev.*, 2013, **12**, 490–508.

6. J. Francois, *Heredity in Ophthalmology*, Mosby, 1961.

7. F. Avila, B. Friguet and E. Silva, *Photochem. Photobiol.*, 2015, **91**, 767–779.

8. E. S. Vladimirova, V. V. Salmin, A. B. Salmina, S. A. Oskirko, V. I. Lazarenko, and A. S. Provorova, *J. Appl. Spectrosc.*, 2012, **79**, 136–140

9. D. M. Gakamsky, B. Dhillon, J. Babraj, M. Shelton and S. D. Smith, *J. R. Soc. Interface*, 2011, **8**, 1616–1621.

10. Y. Qazi, G. Wong, B. Monson, J. Stringham and B. Ambati K, *Natl. Inst. Heal.*, 2011, **81**, 198–210.

11. K. M. Meek and C. Knupp, *Prog. Retin. Eye Res.*, 2015, **49**, 1–16.

12. S. Bassnett, Y. Shi and G. F. J. M. Vrensen, *Philos. Trans. R. Soc. Lond. B. Biol. Sci.*, 2011, **366**, 1250–1264.
13. L. A. Remington, *Clinical Anatomy and Physiology of the Visual System*, Elsevier - Health Sciences Division, 2012.

14. Y. P. Tsentalovich, P. S. Sherin, L. V Kopylova, I. V Cherepanov, J. Grilj and E. Vauthey, *Invest. Ophthalmol. Vis. Sci.*, 2011, **52**, 7687–7696.

15. J. P. G. Bergmanson, *Clinical Ocular Anatomy and Physiology*, 2009

16. A. M. Wood and R. J. W. Truscott, *Vision Res.*, 1994, **34**, 1369–1374.

17. S. Lerman, *Am. J. Optom. Physiol. Opt.*, 1987, **64**,11–22.

18. M. J. Davies and R. J. W. Truscott, *J. Photochem. Photobiol. B*, 2001, **63**, 114–125.

19. L. M. Bova, M. H. J. Sweeney, J. E. Jamie and R. J. W. Truscott, *Investig. Ophthalmol. Vis. Sci.*, 2001, **42**, 200–205.

20. B. D. Hood, B. Garner and R. J. W. Truscott, *J. Biol. Chem.*, 1999, **274**, 32547–32550.

21. J. M. Dyer, S. D. Bringans and W. G. Bryson, *Photochem. Photobiol. Sci.*, 2006, **5**, 698–706.

22. H. Bloemendal, W. De Jong, R. Jaenicke, N. H. Lubsen, C. Slingsby and A. Tardieu, *Prog. Biophys. Mol. Biol.*, 2004, **86**, 407–485.

23. R. Michael and A. J. Bron, *Philos. Trans. R. Soc. Lond. B. Biol. Sci.*, 2011, **366**, 1278–1292.

24. R. J. W. Truscott, *Protein misfolding, Aggreg. Conform. Dis.*, 2007, 435–447.

25. B. J. Kirkwood, P. L. Hendicott, S. A. Read and K. Pesudovs, *J. Cataract Refract. Surg.*, 2009, **35**, 1210–1215.

26. L. Zhao, X.-J. Chen, J. Zhu, Y.-B. Xi, X. Yang, L.-D. Hu, H. Ouyang, S. H. Patel, X. Jin, D. Lin, F. Wu, K. Flagg, H. Cai, G. Li, G. Cao, Y. Lin, D. Chen, C. Wen, C. Chung, Y. Wang, A. Qiu, E. Yeh, W. Wang, X. Hu, S. Grob, R. Abagyan, Z. Su, H. C. Tjondro, X.-J. Zhao, H. Luo, R. Hou, J. Jefferson, P. Perry, W. Gao, I. Kozak, D. Granet, Y. Li, X. Sun, J. Wang, L. Zhang, Y. Liu, Y.-B. Yan and K. Zhang, *Nature*, 2015, **523**, 607–611.

27. L. N. Makley, K. A. McMenimen, B. T. DeVree, J. W. Goldman, B. N. McGlasson, P. Rajagopal, B. M. Dunyak, T. J. McQuade, A. D. Thompson, R. Sunahara, R. E. Klevit, U. P. Andley and J. E. Gestwicki, *Science*, 2015, **350**, 674–677.

28. 1 H. Lin, H. Ouyang, J. Zhu, S. Huang, Z. Liu, S. Chen, G. Cao, G. Li, R. A. J. Signer, Y. Xu, C. Chung, Y. Zhang, D. Lin, S. Patel, F. Wu, H. Cai, J. Hou, C. Wen, M. Jafari, X. Liu, L. Luo, J. Zhu, A. Qiu, R. Hou, B. Chen, J. Chen, D. Granet, C. Heichel, F. Shang, X. Li, M. Krawczyk, D. Skowronska-Krawczyk, Y. Wang, W. Shi, D. Chen, Z. Zhong, S. Zhong, L. Zhang, S. Chen, S. J. Morrison, R. L. Maas, K. Zhang and Y. Liu, *Nature*, 2016, **531**, 323–328.

29. L. Kessel and M. Larsen, *PLoS One*, 2015, **10**, DOI:10.1371/journal.pone.0123732

30. T. Holm, C. T. Raghavan, R. Nahomi, R. H. Nagaraj and L. Kessel, *BMC Res. Notes*, 2015, **8**, DOI 10.1186/s13104-015-0977-3

31. Horiba, Jobin and Yvon Inc., FluoroMax Spectrofluorometer – Operation and Maintainance, SPEX Industries Inc., New Jersey

32. W. A. Cox, *Early Postmortem Changes and Time of Death*, 2009

33. B. P. Danysh and M. K. Duncan, *Exp. Eye Res.*, 2009, **88**, 151–164.

Appendix 5.1: Corroboration of Experimental Set-Up

Due to the variation in lens size, samples were either held in macro or semi-micro cuvettes. Consequently, the position of each lens may have differed and positional dependence of the lens could cause variation of results due to the distribution of chromophores within the lens.

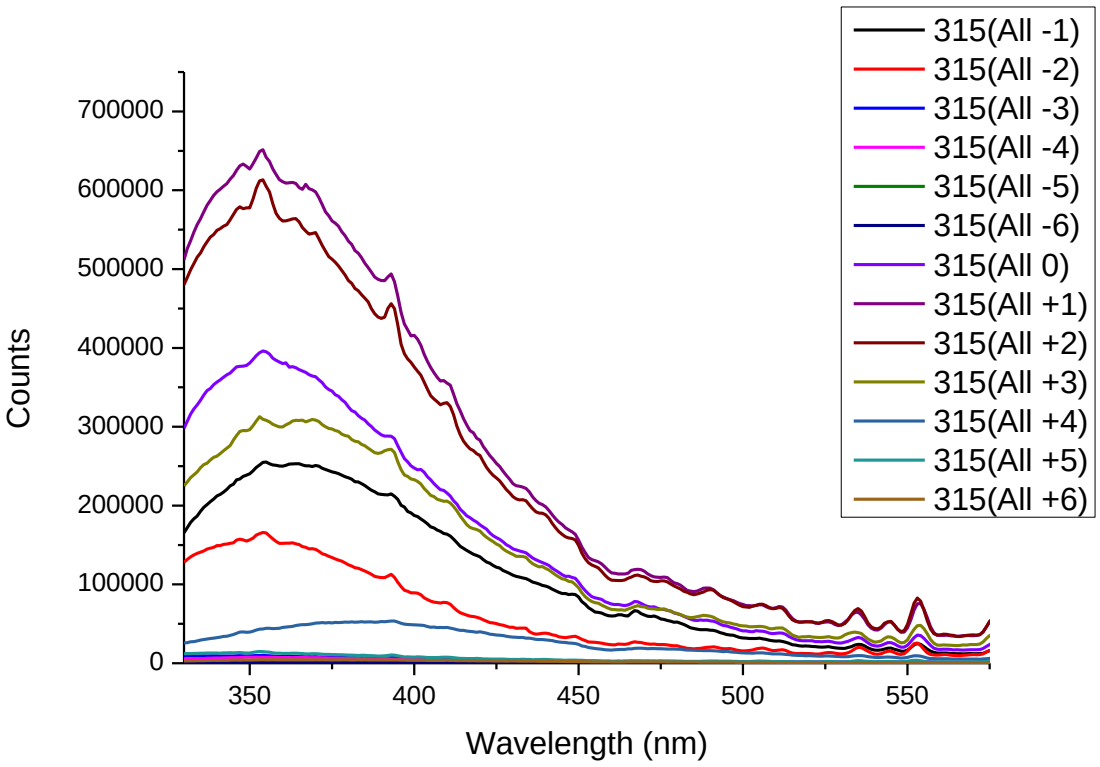

Figure A5.1a. Positional dependence of lens contained in semi-micro cuvette (channel depth 3.5 mm) and excited at 315 nm – Cuvette moved in 1mm increments from focal point in the positive (away from source) and negative (towards source) directions

Figure A5.1a shows that the position of the lens has the most significant effect on the emission intensity. Peak position remained consistent until the focal point reached the surface of the cuvette (All +4) and when the focal point sat at the back of the lens (All -2) at which point a slight shift was observed.

From these results, slight positional differences between holding the lenses in macro or semi-micro cuvettes does not appear to affect the outcome of experiments.

Appendix 5.2: Fluorescence characteristics of the cornea and vitreous humour

EEM of fluorescence emission from healthy components

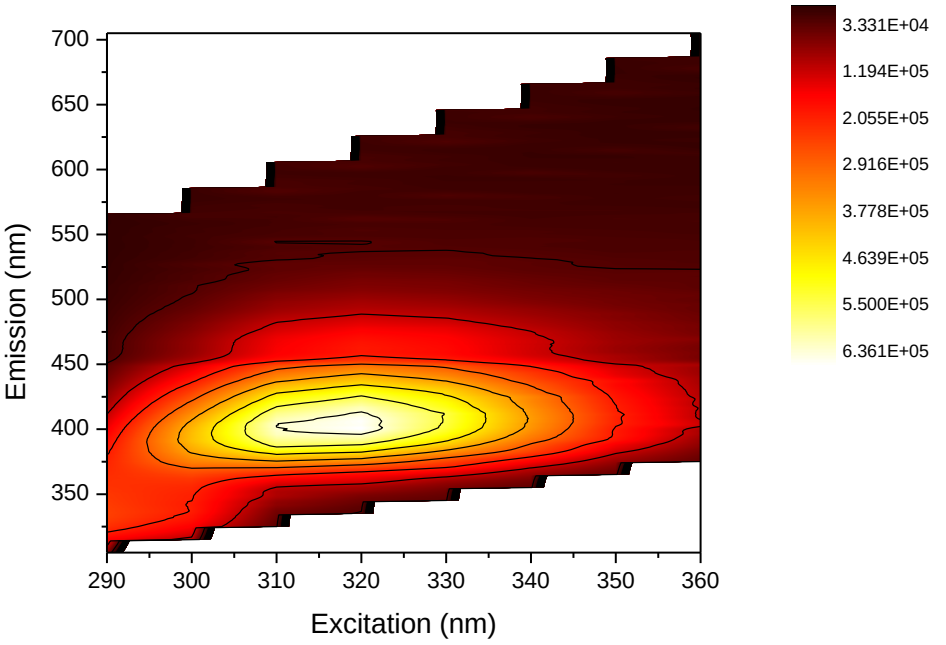

Figure A5.2a. EEM spectrum of vitreous humour

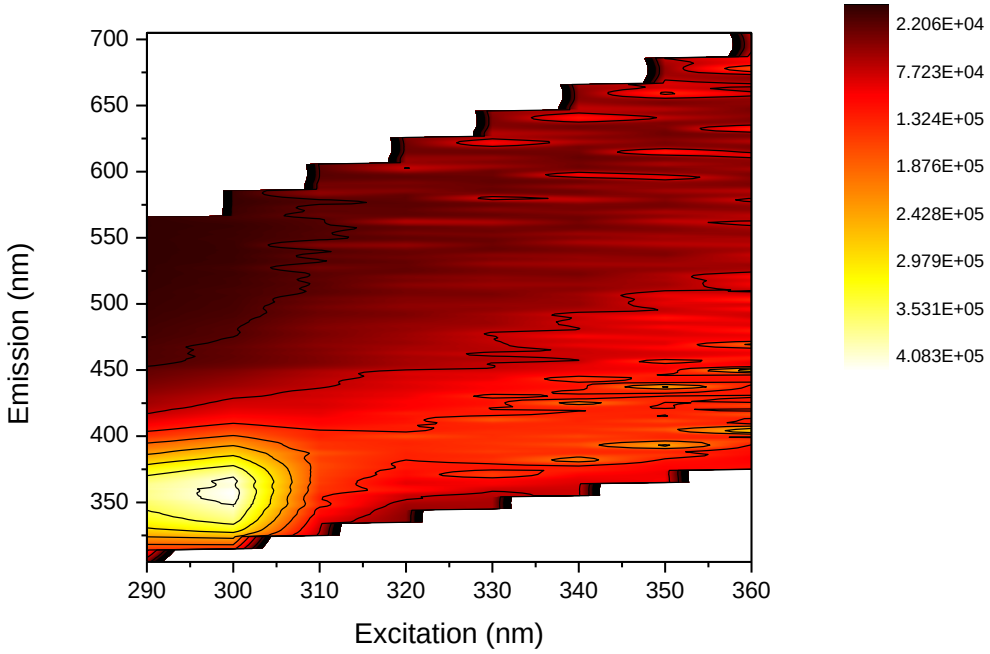

Figure A5.2b. EEM spectrum of cornea

Comparison of the action spectra shows that emission from the cornea (Figure A5.2b) is dominated by tryptophan emission at 340 nm from the epithelium whereas the vitreous humour (Figure A5.2a) displays the strongest emission at 400 nm with a small contribution from tryptophan emission at 350 nm. Considering the role of each component these results are unsurprising. The cornea is the first defence in UV protection but is transparent to the visible range, therefore the only dominant absorbing species would be those that absorb in the UV i.e. tryptophan/proteins; the vitreous humour is also transparent to the visible range, however, the vitreous humour is the last defence against UV damage to the retina, therefore, PChs are present.

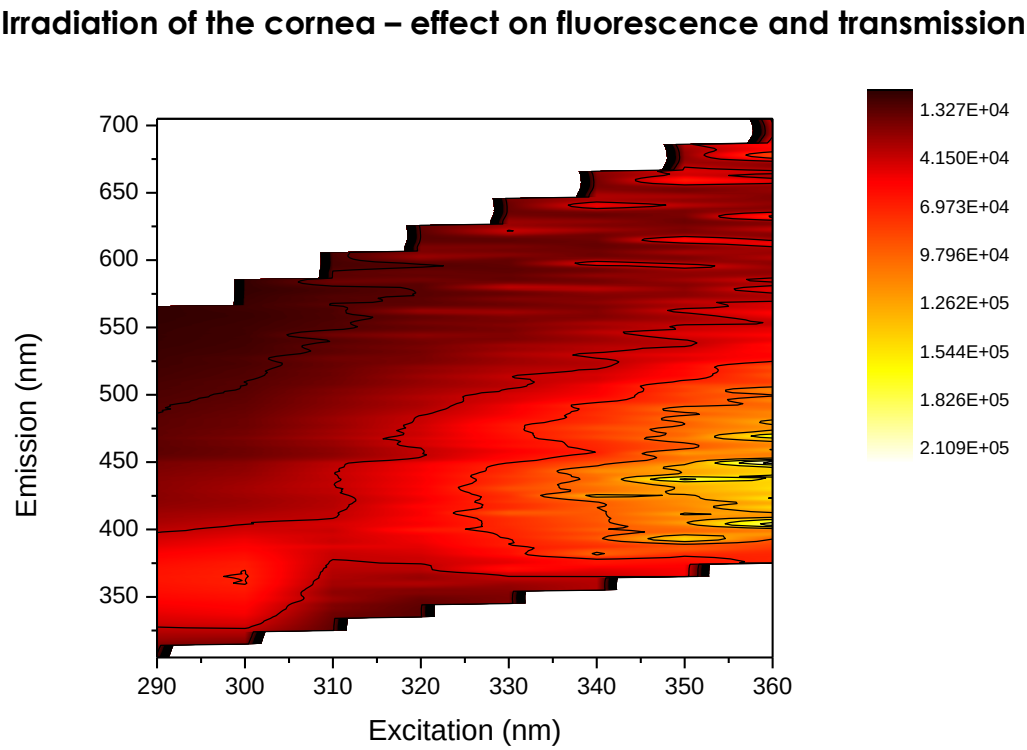

Figure A5.2c. EEM of cornea irradiated at 310 nm for 3 hours (the same sample was used to produce Figure A2b)

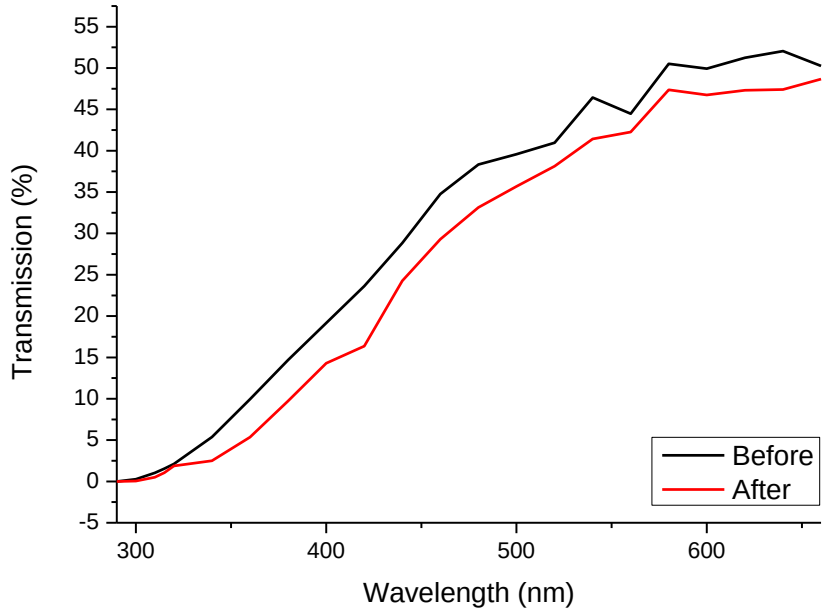

Figure A5.2d. Comparison of transmission through the cornea before and after irradiation

Irradiation of the cornea resulted in an 80% reduction in tryptophan emission intensity (Figure A5.2c) due to photo-oxidation, however, this translated to a reduction in transmission of only 10% (Figure A5.2d). This suggests that, following irradiation of the cornea, resultant, non-fluorescent photo-products do not absorb significantly in the visible range.

Chapter 6: Overall Conclusions

The work presented in this thesis demonstrates the value of utilising fluorescence in the interrogation of biological systems in the solid state.

Analysis of single-use instruments pre-labelled with FITC using the prototype EFScan system has revealed that residual protein, on the order of micrograms can be found on instruments before their first use, raising questions as to the quality and conditions of their manufacture. Comparison of results from the three centre study show that consistent levels of contamination were detected using three different fluorescence based techniques, verifying fluorescence detection as an appropriate method in the detection and quantification of residual proteinaceous contamination on surgical instruments. It was also determined that the EFScan system exceeds the sensitivity of the ninhydrin swab test, which is commonly used in hospital SSDs, by more than a thousand-fold. Subsequently, disposable instruments obtained from three manufacturers; Qasco, DMI Ltd. and Instrapac were analysed using the EFScan system and the results compared. It was found that contamination ranging from 2.4 - 19.6 µg of protein could be found per side of an instrument before their first use. Moreover, hotspot values were found to be 10 times higher than the average amount of protein per pixel. As hotspots represent areas of high protein contamination and therefore thicker plaques, the likelihood of infectious material detaching from the instrument surface is increased. Following revision of the HTM 01-01 to include a threshold value of 5µg of protein per side of an instrument, it was observed that only 13% of instruments (10 out of 75) from the three manufacturers would have passed inspection. Additionally, in light of the high hotspot values observed it would be pertinent to include an additional threshold to contribute to the improvement of quality control in SSDs.

Investigation into the possibility of intrinsic detection of protein via detection of Trp fluorescence revealed that the commonly used protein standard BSA is not a suitable standard for the intrinsic detection and quantification of protein. Due to the susceptibility of the Trp residues of BSA to photo-oxidation, Trp emission is quickly bleached to produce long wavelength emission associated with the KRTDs NFK and kynurenine. Analysis of other possible candidates; BFG, γ-globulins and lysozyme revealed that although the Trp residues in these proteins are not susceptible to photo-oxidation they are susceptible to photo-bleaching. Wavelengths below 300 nm can result in photo-ionisation of Trp leading to the production of a Trp radical which

can go on to react, bleaching the observed Trp emission. Bleaching of Trp emission was also observed in α- and γ-crystallins of the lens which have evolved to resist photo-oxidation, further suggesting that photo-ionisation is the dominant photochemical process following the irradiation of crystalline proteins below 300 nm. BFG, lysozyme and γ-globulins especially were identified as possible candidates as standards for the intrinsic detection of protein on surgical instruments. Analysis of BFG on stainless steel revealed that protein amounts as low as 200 fmole mm^{-2} could be detected. Additionally, analysis of lifetime measurements of BFG on stainless steel has revealed that the amount of protein on the stainless steel surface, at the low concentrations found on reprocessed surgical instruments, should not affect the lifetimes obtained. These results show that a combined steady-state/time-resolved method for the detection of residual protein on medical instruments could be a possibility.

The final project in this thesis, carried out in conjunction with industrial partners from Edinburgh Biosciences Ltd. in Livingston, found that the early detection of cataract may be possible via monitoring of Trp fluorescence from the lens. Efforts to create cataract in extracted porcine lenses via UV irradiation, induced fluorescence signals akin to those observed in cataractous lenses and the progression of induced fluorescence changes (Trp > NFK/kynurenine) could be easily monitored in extracted lenses. However, these fluorescence changes were not accompanied by the characteristic yellowing and cloudiness associated with natural cataract, therefore, creation of conventional cataract under the conditions described is not possible. Irradiation at 360 nm bleached the long wavelength fluorescence induced during attempted cataract formation suggesting that a light based method could be utilised to offer a non-invasive treatment for cataract. Conversely, bleaching of the long wavelength emission exceeded that of the emission that was first created via irradiation, suggesting that natural, long wavelength, chromophores were also destroyed. Despite the complexities of the system, which includes variation in spectral intensity and shape from lens to lens, the fluorescence characterisation carried out to this point is an encouraging step towards the early detection of cataract, however, the possibility of light based treatments is unlikely and will require significant further research.

This work provides a strong foundation for extensive further research in the subject of fluorescence detection and quantification of protein in two very different systems. Further investigation into the achievable limit of detection for the intrinsic detection

of protein on surgical instruments could lead to the development of novel instrumentation based on both steady-state and time-resolved fluorescence detection, providing a sensitive tool for the assessment of decontamination standards in SSDs. Additionally, detailed fluorescence characterisation of lenses of different ages and health could lead to a non-invasive, light based method for the early diagnosis, monitoring and, perhaps, the treatment of cataract.